2020-08-12

Physical Characterization of Crackle-Related Events in Military Jet Aircraft Noise

Aaron Burton Vaughn
Brigham Young University

Physical Characterization of Crackle-Related Events in Military Jet Aircraft Noise

Aaron Burton Vaughn

A thesis submitted to the faculty of
Brigham Young University
in partial fulfillment of the requirements for the degree of

Master of Science

Kent L. Gee, Chair
Brian E. Anderson
Brian D. Jeffs

Department of Physics and Astronomy

Brigham Young University

ABSTRACT

Physical Characterization of Crackle-Related
Events in Military Jet Aircraft Noise

Aaron Burton Vaughn
Department of Physics and Astronomy, BYU
Master of Science

Crackle is a perceptual feature of supersonic jet noise that is related to the presence of acoustic shocks. The skewness of the time-derivative of the pressure waveform, or derivative skewness, is used as a metric indicative of crackle perception. The three main objectives of this work are: 1) Determine the potential spatial origin of crackle-related events in the near field of a high-performance military aircraft via an event-based beamforming method. 2) Investigate the potential for nonlinear, irregular shock reflections occurring along the near-field ground array and their implications on derivative skewness. 3) Relate the near-field, crackle-related events to far-field crackle perception by comparing nonlinearly propagated waveforms with measured far-field data. The event-based beamforming method used to determine source and far-field relationship of shock-like events utilizes the cross correlation between adjacent microphone waveform segments to determine the angle of propagation for an ensemble of crackle-related events within the waveform. The angle of propagation is traced towards the source for each event to find its apparent origin along the jet lipline. Beamforming results indicate that crackle-related events appear to originate anywhere from 2 to 14.5 m downstream along the jet lipline, with distributions that shift downstream and broaden with increasing engine power. The shock reflection classification method builds on the event-based beamforming method to calculate angle of incidence relative to the ground for an ensemble of shock events. The combination of angles of incidence and the measured shock strengths of the events reveal that irregular reflections are likely to occur over the majority of the array, which likely elevates the derivative skewness values due to steeper shocks with greater peak-to-peak pressures relative to off-ground measurements. Near-field, crackle-related events are extrapolated to the far field using a nonlinear propagation model to determine their prevalence in the far field. Cross-correlation coefficients of waveform segments centered about the propagated events indicates that for farther aft angles, near-field events are more related to far-field measurements. Waveform observations show that shock-like events in the near field that are more spiked in nature tend not propagate into the far field. However, near-field, large-derivative events with broader, high-pressure peaks nonlinearly steepen and form shocks in the far field that are likely contribute to crackle perception.

Keywords: supersonic jet noise, crackle, aeroacoustics, shock

Acknowledgments

The mentors, advisors, teachers, colleagues, friends, and family who have helped me reach this point and their influence in my life are innumerable and immeasurable. I am grateful to Hales Swift for his work in developing the event-based beamforming code, Kevin Leete for all the office talks and co-authorship on several papers I have authored, and Jacob Ward for playing basketball with me on intramural teams and helping me get set up with the nonlinear propagation code used in Chapter 4. My advisor has been a great source of mentorship and an example of excellence in his field. He has taught both in word and deed what it is to be a scholar and a mentor. To my parents and other family members who always encouraged me in my scientific endeavors, you have helped me pursue a course of study which has propelled me towards a dream career. And to my wife, who has been by my side throughout this journey, I am forever grateful for your love and support to pursue this endeavor.

The author gratefully acknowledge funding for the measurements provided through the F-35 Program Office and Air Force Research Laboratory. (Distribution A: Approved for public release; distribution unlimited. F-35 PAO Cleared 05/17/2021; JSF20-1007) This research was funded under an Air Force Research Laboratory SBIR program.

Table of Contents

List of Figures

List of Tables

Chapter 1
Introduction

1.1 Motivation

"[T]urbofan engines that propel today's high-performance tactical aircraft also produce "the sound of freedom" – noise levels sufficient to cause concern regarding personnel hearing loss on airfields and aircraft carries and increased annoyance for communities near bases." [1] Throughout the United States, and elsewhere in the world, communities are being built ever closer to existing air bases. These communities are potentially exposed to noise produced by these aircraft during routine flyovers. Therefore, understanding source mechanisms of military jet noise and how they propagate into the far field is important for determining potential community annoyance and further minimize its impact through improved noise mitigation efforts.

1.2 Jet Crackle

Jet crackle is an annoying[2] and dominant[3] perceptual component of supersonic jet noise related to the reception of acoustic shocks. Ffowcs Williams *et al.*[2] initially observed this phenomenon in a supersonic commercial aircraft, the Concorde, and described these aircraft as "particularly prone to producing sudden spasmodic bursts of a rasping fricative sound." Further describing this phenomenon, Ffowcs Williams *et al.* stated, "It is a startling staccato of cracks and bangs and its onomatope, 'crackle' conveys a subjectively accurate impression." Crackle is also perceptible in noise produced by rockets[4,5] and volcanoes,[6] which are essentially jets with larger nozzles. However, crackle does not seem to be readily identifiable in laboratory-scale jet noise.[7]

The most common occurrence of crackle is in noise from military-style, high-performance engines, which noise can regularly impact local communities.

Since its original definition, differing interpretations of jet crackle have emerged over the years. Initially crackle was defined by Ffowcs Williams *et al.* as 1) the presence of acoustic shocks, 2) transient events undetectable purely by a spectral means, 3) predictable by the skewness of the amplitude probability density function, or pressure skewness, and 4) primarily a source phenomenon.[2] Consistent with a recent subjective listening study carried out at Brigham Young University,[8,9] crackle is defined for this research as a perceptual feature of supersonic jet noise that is related to the reception of acoustic shocks. This definition inherently coincides with the first two points of Ffowcs Williams *et al.*'s definition; however, the definition used in this study disagrees with the latter two points, as supported by other recent studies.[10–13]

1.2.1 Crackle-related Metrics

A point of interest in several studies is predicting crackle perception. Particularly of interest are metrics of nonlinearity that are responsive to the presence of shocks. Acoustic shocks are characterized by large positive pressure derivatives and may be present at the noise source, in the near field, or develop in the far field through nonlinear propagation. Acoustic shocks may be weak or nonexistent in the near-field, but via nonlinear propagation, high-amplitude sound pressures can grow to be a characteristic component of the far-field waveform, thus causing the perception of crackle in the far field.[10-15] Pressure skewness was a metric initially proposed by Ffowcs Williams *et al.*[2] that quantifies the asymmetry of the pressure waveform. Some have since examined other temporal statistics to quantify "bursts"[14] or rise-time and peak-to-peak pressures.[15] Others have tried using kurtosis to examine fourth-order peakedness.[16,17] Gee *et al.*[8] proposed the skewness of the time derivative of the pressure waveform, or derivative skewness (Sk{∂p/∂t}), as an indicator

of crackle content. The derivative skewness has a stronger relation to crackle than the pressure skewness as determined in a recent subjective listener study.

1.2.2 Initial Listener Study

In order to determine the relationship of crackle perception and derivative skewness, jet waveforms of varying derivative skewness values are auralized and rated in a subjective listener study. In the first formal, jury-based listening study[8,9] of its kind, 31 participants listened to 3 second audio clips from a F-35A played back at a consistent level via a loudspeaker. These waveforms were selected from a far-field microphone arc about 305 m from the aircraft to test a variety of pressure skewness and derivative skewness values. Combinations of high derivative skewness and low pressure skewness and vice versa were chosen to better quantify their relative influence on crackle perception. In one portion of the study, participants rated the crackliness of a signal using a five-point scale ranging from smooth, no crackle to intense crackle. Comparing the results of the crackle ratings with the derivative skewness and pressure skewness values yielded a significantly greater R^2 value for derivative skewness than pressure skewness. The study concluded that the transition from intermittent to continuous crackle perception occurs at $\mathrm{Sk}\{\partial p/\partial t\} = 3$ and proposed an equation relating derivative skewness to crackle rating.[8]

While potential crackle content can be determined using derivative skewness, source mechanisms that give rise to far-field crackle perception are not well understood. Nonlinear propagation likely plays a strong role in the development of crackle in the far field; however, other factors, such as shocks present in the near field and how they relate to the perception of crackle in the far field are important to consider. In addition, with the use of the derivative skewness as a metric to predict crackle content, the cause for difference in derivative skewness values at ground-based measurements compared to off-ground locations has need of additional study. This

difference in derivative skewness has been previously observed for a high-performance military aircraft measurement,[18] and the present F-35 data provides an opportunity to further investigate this occurrence.

1.3 F-35B Measurement

Acoustic measurements of the F-35A and F-35B variants were made in September 2013 at Edwards Air Force Base. While the listener study relied on the data from the F-35A,[8] the A and B variants are acoustically the same and the study contained in this thesis uses data collected from the B variant.[19] The aircraft was tethered to the ground as shown in Figure 1.1 with the center of the nozzle exit set 2 m above the coordinate system origin point. The Cartesian coordinate system is defined where x is the sideline distance, y is the height above the ground, and z is the downstream distance from the nozzle. The nominal diameter of the jet nozzle is approximately 1 m, though it varied slightly with engine condition. The aircraft operated at engine conditions ranging from idle to afterburner, with interest given to the four engine conditions—75%, 100%, 130%, and 150% engine thrust request (ETR)—with significant crackle content perceived. Engine conditions greater than 100% are possible due to the addition of afterburner. Time waveforms were synchronously acquired for 5–6 run ups at each engine condition. Each recording is at least 27 s, except for the 130% ETR case used in this study, which was only 10 s in length.

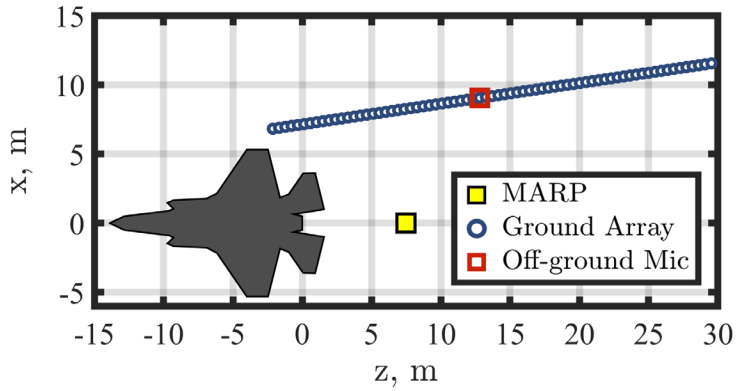

Figure 1.1 Schematic of the F-35B aircraft and the ground-based linear microphone array.

The studies in Chapter 2 and Chapter 3 focus on data collected from a 71-element, linear ground array, as illustrated in Figure 1.1. It consisted of GRAS 6.35 mm (1/4") pressure microphones, and the acoustic data were acquired using National Instruments PXI-449X cards sampling at 204.8 kHz. The array was located approximately 8–10 m from the estimated jet shear layer with a 0.45 m (18") inter-microphone spacing. The microphone array reference point (MARP) is located 7.5 m downstream of the nozzle as shown in Figure 1.1. Comparisons made in Section 3.3 between ground and off-ground placement of microphones is possible due to an off-ground microphone located in the vicinity of the ground array, which is represented by a red square in Figure 1.1. The off-ground microphone was a GRAS 6.35 mm (1/4") free-field microphone sampled at 204.8 kHz.

The study in Chapter 4 relies on near to far-field microphone arc arrays with placement defined by radials and jet inlet angles relative to the MARP, as shown in Figure 1.2. Arc radial distances range from 19 m (63′) to 305 m (1000′) with each arc doubling in distance, except for the 29 m (94′) arc. Microphones are located anywhere from 0° to 160° in 10° increments and at 5° increments in the maximum radiation region from 120° to 160°. An assortment of GRAS 6.35 mm (1/4") pressure and free-field microphones were used at the 19, 29, 38.2, and 76 m (63′, 94′, 125′, and 250′) arcs and data were recorded using National Instruments PXI 4496 cards sampling at

204.8 kHz. While there were microphones co-located along the outer arcs, the subset used in the present study consist of an assortment of GRAS and B&K 6.35 mm (1/4") free-field microphones at 130°–140° along the 152 m (500′) arc and 110°–150° along the 305 m (1000′) arc and B&K and PCB 12.7 mm (1/2") free-field microphones at the remaining locations. The outer two arcs used National Instruments PXI 4472B cards sampling at 96 kHz. A comparison between derivative skewness values measured by co-located microphones at 152 and 305 m arcs are given in the Appendix and plotted in Figure A.2.

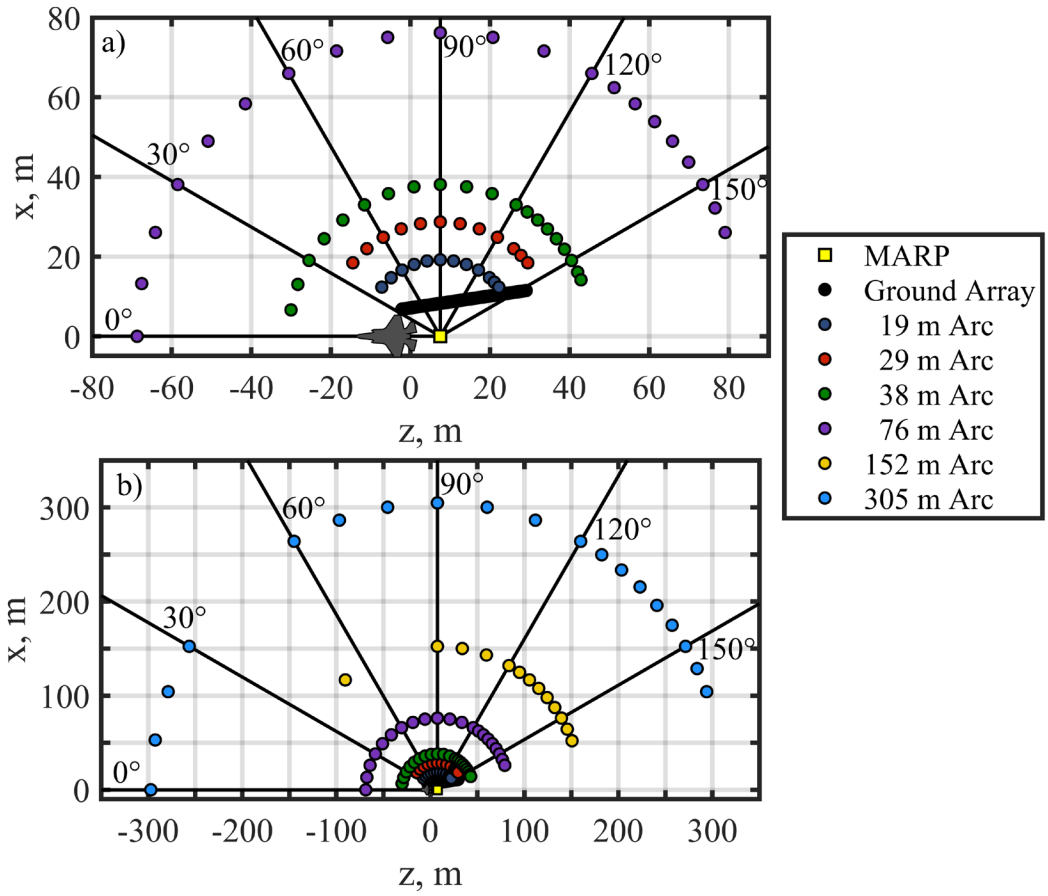

Figure 1.2 Schematic of the F-35B aircraft and the locations of the a) near and b) far-field measurement arrays.

Pertinent meteorological data are the average atmospheric pressure across measurements of 93.45 kPa and for the 150% ETR run investigated in Chapter 4, the temperature and relative

humidity were approximately 293.45 K and 41.2%. Other analyses of the ground array are reported on in Refs. 20– 24. More details for this measurement are found in Ref. 19.

1.4 Objectives and Scope of Work

This thesis investigates physical jet noise phenomena associated with the perception of crackle. The three main goals of this thesis are: 1) Determine the potential spatial origin of crackle-related events in the near field via an event-based beamforming method. 2) Investigate the potential for irregular shock reflections occurring along the near-field ground array and their implications on derivative skewness. 3) Relate the near-field origins of crackle to far-field perception by comparing nonlinearly propagated waveforms with measured far-field data.

The majority of the work contained in this thesis comes from papers submitted or in process by the author to journals or conference proceedings papers. A list of source materials for Chapters 2–4 is found in Table 1.1 for reference.

Table 1.1 Source material for technical chapters.

Chapter	Source Article(s)
Chapter 2	Vaughn *et al.,* "Source localization of crackle-related events in military aircraft jet noise," *AIAA Journal* (2021). https://doi.org/10.2514/1.J059823 Vaughn *et al.*, "Crackle-related beamforming of military jet aircraft noise," AIAA Paper 2019-2664 (2019). https://doi.org/10.2514/6.2019-2664 Vaughn *et al.*, "Beamforming of supersonic jet noise for crackle-related events," *Proc. Mtgs. Acoust.* (2018). https://doi.org/10.1121/2.0000998
Chapter 3	Vaughn *et al.*, "Evidence for nonlinear reflections in shock-containing noise near high-performance military aircraft," *J. Acoust. Soc. Am.* (2021). https://doi.org/10.1121/10.0003932
Chapter 4	Vaughn *et al.*, "Near to far field correlation of crackle-related events in military aircraft jet noise," *Proc. Mtgs. Acoust.* (clearance pending).

Chapter 2
Near-field Beamforming of Crackle-related Events

2.1 Introduction

Crackle is an annoying[2] and dominant[3] component of high-power jet noise. In the initial study of crackle in supersonic commercial aircraft noise, Ffowcs Williams *et al.*[2] described these aircraft as "particularly prone to producing sudden spasmodic bursts of a rasping fricative sound." They further stated, "It is a startling staccato of cracks and bangs and its onomatope, 'crackle' conveys a subjectively accurate impression." Since the publication of this initial investigation, differing crackle definitions have emerged as various metrics[13,14,16,25,26] and methodologies[14,27–29] have been developed. In this study, we define crackle as a perceptual feature of supersonic jet noise that is related to the reception of acoustic shocks. This is in accord with the assertion made by Ffowcs Williams *et al.* that the "physical feature of a sound wave that gives rise to the readily identifiable subjective impression of 'crackle' is shown to be the sharp shock-like compressive waves that sometimes occur in the waveforms."[2]

Acoustic shocks are rapid pressure increases that are characterized by large positive pressure derivatives. For shocks in supersonic jet noise, the formation, strengthening, and persistence of the shocks in the far field are largely due to nonlinear effects.[11,12,15] Although the far-field shock evolution is of importance to quantifying community response to flyovers at high powers, source-related investigations are also of importance because of the potential to understand noise production in a way that could provide guidance for future noise reduction methods and technologies, such as those described in Refs. 30–33.

Recent crackle-related studies have used numerical and laboratory-scale data sets to examine steepened-wave or shock-like features in and near the jet. A growing number of numerical investigations have used diverse jet conditions (e.g. nozzle pressure ratios,[34] Mach numbers,[35,36] temperature ratios[17,37–40]) and an assortment of simulation methods to study the jet flow and subsequent noise field. Several of these numerical studies report acoustic shocks with large pressure skewness (the foundation for the original Ffowcs Williams *et al.*[2] criterion) values forming at or near the turbulent shear layer of the jet.[35–38] These findings are complemented by laboratory-scale jet studies that suggest the generation of impulsive signatures exists over a distributed range rather than a localized source region.[41–44]

The analysis approach introduced in this paper is founded on a crackle criterion that has been tied to human subject testing.[8,9,45,46] With crackle defined as a perceptual feature, listening tests are necessary to link the human perception to measurable noise characteristics. Prior studies[45,46] utilized signal processing and informal listening tests to identify the skewness of the time-derivative of the pressure waveform, $\mathrm{Sk}\{\partial p/\partial t\}$ (or derivative skewness), as a measure for the crackle percept. Recently, a relationship between derivative skewness and crackle has been quantified in the first formal, jury-based listening study of crackle.[8,9] The study employed F-35A waveforms with various degrees of crackliness and a range of values for both pressure skewness and derivative skewness. A total of 31 participants auralized the waveforms as part of a category subdivision scaling test[8] and also rank-ordered them in a complementary exercise.[9] The subdivision scaling test resulted in a model for five crackliness categories (smooth noise, rough noise, intermittent crackle, continuous crackle, intense crackle) based on derivative skewness, whereas the relationship between pressure skewness and the crackle percept was found to be statistically insignificant.[8] The listening test revealed that a jet noise waveform with a

$Sk\{\partial p/\partial t\} > 3$ is perceived to 'continuously crackle.' This criterion is used as part of the analysis reported herein.

To find the regions in the jet responsible for crackle-containing waveforms in the field, this study examines the origins of waveform segments chosen by the presence of large positive derivatives that contribute significantly to the overall derivative skewness value. The origins of these waveform segments are calculated by a two-point cross-correlation beamforming method. A brief summary of the acoustical measurement of the F-35B high-performance military aircraft is provided, which is acoustically similar to the F-35A used in the subjective listener study.[19] A description of the methodology used in the beamforming process is subsequently provided. Results for four engine conditions are then discussed, which are followed by an analysis involving microphone pair groupings to describe jet noise characteristics associated with jet crackle.

2.2 Event-based Beamforming Methods

This study employs an event-based beamforming method involving a cross correlation of adjacent microphones' waveforms windowed around particular events, from which the radiation angle and apparent origin of the events are calculated. The analysis method, which builds off of that described by Vaughn *et al.* in Ref. 24, also resembles the method used in Refs. 43, 44, 47 to detect the apparent acoustic origins along the jet axis of large-amplitude events for both laboratory and full-scale jets. A previous study by Vaughn *et al.*[24] examined three types of event triggers: maximum pressure values, maximum derivative values and, as a control, regularly-spaced, non-overlapping waveform segments. However, only the maximum derivative events are considered in the present analysis, for two reasons. First, the three types of event definitions revealed similar source characteristics, as high-amplitude events were correlated with high-derivative events and

even relatively short event windows typically contained a high-derivative or high-amplitude event within the regularly spaced segments. Second, as demonstrated in Section 2.2.1, the large derivative values are directly linked to elevated derivative skewness, which in turn is directly correlated with the crackle percept as quantified by Gee *et al.*[8,9] The relationship between the large-derivative event trigger and derivative skewness is elaborated in the following section.

2.2.1 Event Selection Method

Two short F-35B waveform segments with and without acoustic shocks are shown in Figure 2.1. Each 10-ms waveform was taken from a measurement of the F-35B operating at maximum afterburner (150% ETR), with Figure 2.2a measured at the farthest upstream microphone ($z = -2.1$ m) and Figure 2.2c in the region of maximum radiation ($z = 11$ m). Distinct acoustic shocks are present in Figure 2.2c, which are characterized by sudden pressure increases followed by longer rarefactions. Corresponding derivatives of these waveforms are presented in Figure 2.1b and 2.1d, with the peaks in these plots corresponding to sudden increases in pressure. Based on the Gee *et al.*[8] crackle criteria, the waveform represented by the segment in Figure 2.1a (Sk{∂p/∂t} = 0.6) is considered to not contain crackle and the waveform represented in Figure 2.1c (Sk{∂p/∂t} = 9.4) would contain "intense crackle." Auralization of the waveforms with studio quality headphones confirms the predicted crackle perception of these waveforms.

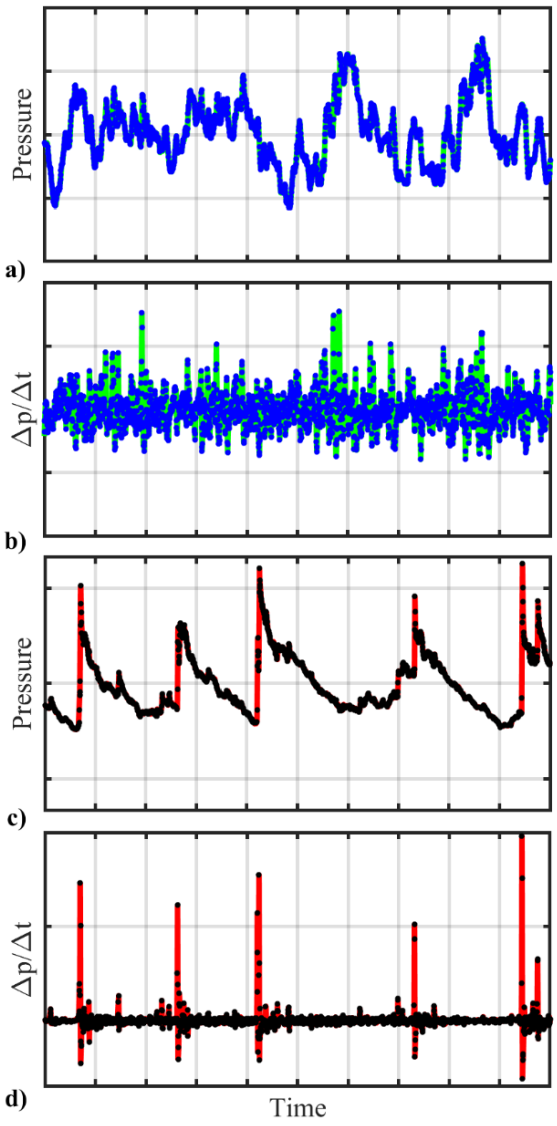

Figure 2.1 Waveforms a) without and c) with acoustic shocks present and their corresponding derivatives in b) and d).

The event-based beamforming approach in this study triggers off of large derivatives, which are related to crackle via the Sk{∂p/∂t}. The relationship between the discretely measured pressure derivative, Δp/Δt, and Sk{∂p/∂t} is shown in Figure 2.2 with the time-derivative of a 10-s pressure waveform in blue, the running Sk{∂p/∂t} value calculated for non-overlapping 20-ms segments in red, and the Sk{∂p/∂t} value for the entire waveform of 3.6 in green. Large peaks in the Δp/Δt waveform represent high-derivative events, and the largest Sk{∂p/∂t} values

occurring simultaneously with the Δp/Δt peaks indicate that these events contribute most significantly to the overall Sk{∂p/∂t} value of the waveform. Using this direct link of Sk{∂p/∂t} with the large-derivative events in conjunction with the result of the prior subjective studies,[8,9] the maximum derivative events are used in the subsequently described event-based beamforming method.

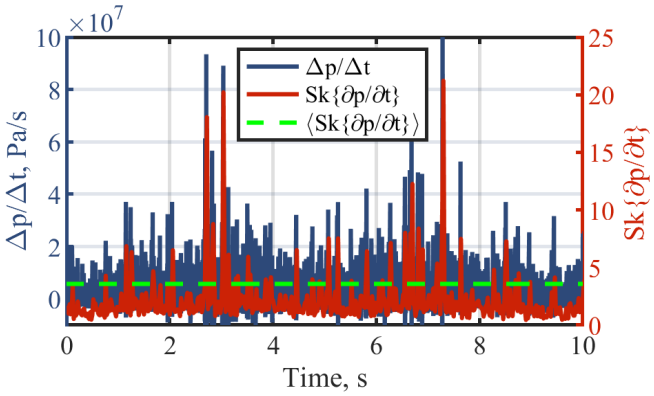

Figure 2.2 Pressure waveform time derivative, Sk{∂p/∂t} values calculated for every 20-ms segment, and time-averaged Sk{∂p/∂t} from a 10-s waveform.

For every pair of adjacent microphones along the array, the events are selected in the upstream microphone. In the 27-s waveforms, the derivative values were sorted in descending order, and the top one thousand were selected with the condition that they were not within 2.4 ms of each other to allow for distinction between shock events in the applied signal processing method. An example of a defined event is indicated by the red x in Figure 2.3a. Events defined in the reference channel may or may not become events in the adjacent channel when the adjacent channel is used as a reference channel for the next microphone pair, as this depends upon a given large derivative event persisting across multiple microphones. For example, the acoustic shock that occurs at about 8.5 ms in the reference channel in Figure 2.3a is seen as having a significantly reduced amplitude at about 9 ms in the adjacent channel in Figure 2.3b. Fievet *et al.*[26] observed that not all waves propagate in the same direction with the possibility of crossing waves; however,

further investigation is needed to understand why particular acoustic shocks change drastically between adjacent microphones. A justification for the use of only a two-point cross-correlation beamforming method is provided in the Appendix.

2.2.2 Beamforming Method

After events are defined, a window is applied around each event in both the reference and adjacent channels, as shown in Figure 2.3. The window is centered about the defined event in the reference channel, but when applied to the other channel in the pair a time lag is added so that the peak of the window is at an approximation of the event in the adjacent channel. This time lag is determined by assuming the MARP as the source location for the event, determining the relative path length differences, and assuming the events travel at the ambient speed of sound. A 20-ms Hann window was chosen to be sufficiently long that if the event in the adjacent channel does not line up in the center of the window, there is still enough information in the corresponding event to compute a meaningful cross correlation. Due to the length of the window, two events may overlap. However, most (>90%) events occur at least 5 ms from the next closest event, where the window drops by 50%, so most of the information captured by the different waveform segments can be considered independent of the others.

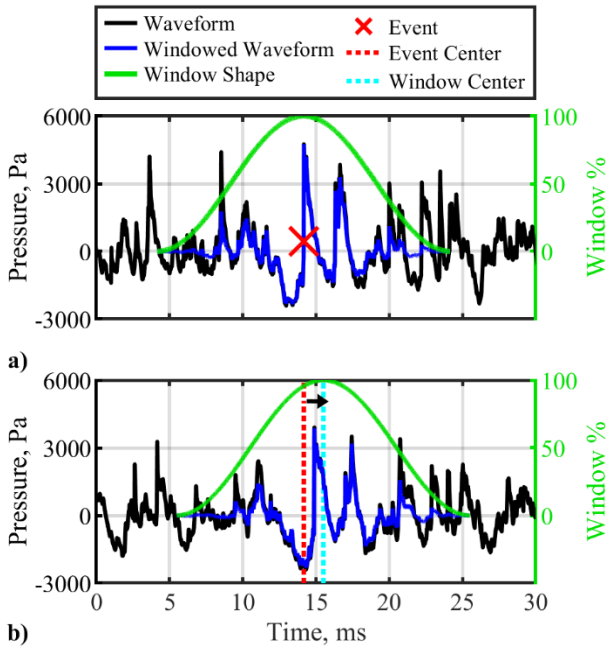

Figure 2.3 Two 30-ms waveforms illustrating the application of a Hann window around a high-derivative event in a) the reference channel and the offset from the event b) the adjacent channel.

To obtain the apparent origin for each pair of windowed waveforms, a simple cross-correlation is used as a time-domain beamformer. From the peak of the cross correlation, a time delay, $\Delta\tau$, due to the difference in arrival time between the two adjacent microphones is found. Then, using the assumption that waves in the vicinity of the microphones are locally planar and travelling at the ambient speed of sound, c, a distance, $c \cdot \Delta\tau$, is found to form a right angle between the arrival path to the downstream microphone and the wavefront in contact with the upstream microphone. This creates a right triangle which can be used to solve for the angle of incidence, ψ, in terms of $c \cdot \Delta\tau$ and the interelement spacing along the array, d. The array offset angle, ϕ (shown in Figure 2.4), is then directly computed from the difference in the microphone locations, and then ϕ and ψ are used to compute the directivity of the event in terms of the jet inlet angle,

$$\theta = 180° - [\psi + \phi]$$

$$= 180° - \left[\cos^{-1}\left(\frac{c \cdot \Delta\tau}{d}\right) + \tan^{-1}\left(\frac{\Delta x}{\Delta z}\right)\right]. \quad \textbf{Equation (2.1)}$$

Tracing the incident angle back to the nozzle lipline gives an apparent source location of the flow corresponding to the event. While the nozzle center is approximately 2 m off the ground, vertical information cannot be achieved from the locally planar assumption and two-point cross-correlation method, therefore apparent origin results are limited to the downstream distance along the nozzle lipline. Each apparent source location and directivity angle found for each of the 1000 events are then compiled into normalized histograms. The process is repeated for each microphone pair in the array.

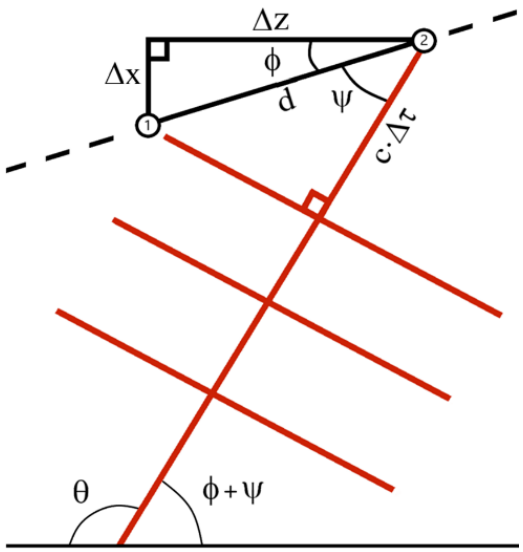

Figure 2.4 Schematic depicting the adjacent two-microphone cross-correlation beamforming method.

2.3 Event-based Beamforming Results

The event-based beamforming process described above has been applied to the F-35B, for engine conditions between 75% and 150% ETR, which have far-field Sk{∂p/∂t} values sufficient

for the perception of continuous crackle at many angles.[8,19] Section 2.2.1 presents normalized histograms of the propagation angle and apparent origin of the highest 1000 derivative events beamformed from microphone pairs along the ground array for 75% and 150% ETRs. Additional comparisons across all four engine conditions are made in Section 2.3.2.

.

2.3.1 Normalized Histograms

The occurrences of beamformed directivity angles are shown for 75% and 150% ETR in Figure 2.5. The abscissa is the z-coordinate of the microphones in the array pictured in Figure 1.1 and the ordinate is the array of histogram bins (representing inlet angle in one-degree increments). Each vertical slice of the colormap corresponds to a normalized histogram of computed angles for a microphone pair, where the histogram counts are divided by the total number of events and represented as probabilities that sum to 1 for each distribution. The horizontal width is the z distance between microphones in a pair. Each histogram is bounded by its 5th and 95th percentiles and probabilities below 0.01 are set to white to emphasize the dominant trends. The transition from upstream ($\theta<90°$) to downstream ($\theta>90°$) radiation is shown by the dashed horizontal line at 90°.

For both 75% and 150% ETR, there is a distinct separation in the peak between 3–5 m along the array, where the directivity angle of the maximum derivative events changes from upstream to downstream radiation. This transition occurs somewhat farther downstream and is more distinct for 150% ETR. Microphone pairs located beyond 4 m for 75% ETR and 4.5 m for 150% ETR all record propagation angles greater than 90°, indicating aft radiation from the origin of the sound in the jet. For 75% ETR, propagation angles increase quickly at first, then nearly level off at the end of the microphone array, whereas for 150% ETR the propagation angles remain constant until about 13 m before increasing to the end of the array. At the end of the microphone

array, the propagation angles converge to 155° for 75% ETR and 150° for 150% ETR. These propagation angles along the microphone array when traced to the jet lipline yield an apparent origin of these top derivative events.

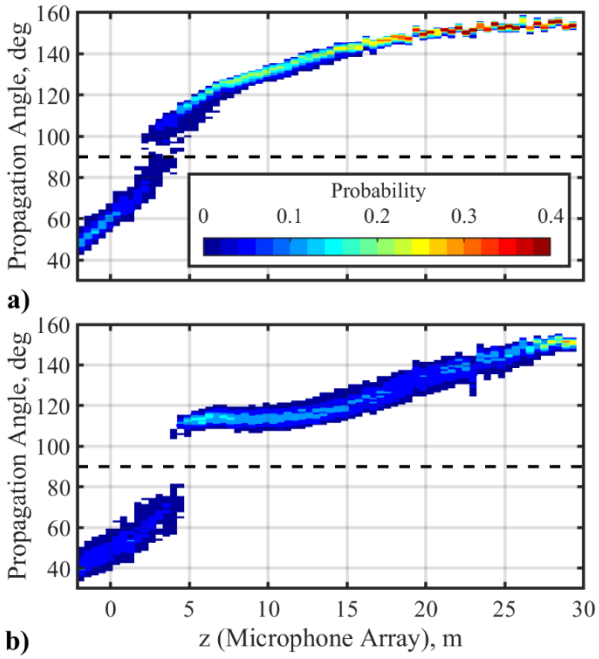

Figure 2.5 Normalized histograms of propagation angle occurrence across each microphone pair for a) 75% and b) 150% ETR.

The propagation angles, such as those in Figure 2.5, are now used to ray-trace the apparent origins of these high-derivative events at all four engine conditions of interest. The resulting apparent origins are compiled into normalized histograms along x = 0.5 m (approximately the jet nozzle lipline) and shown in Figure 2.6 for 75% and 150% ETR. The abscissa is the z-coordinate of the microphones, the same as above in Figure 2.5, while the ordinate now represents the histograms of the apparent origin along the lipline in 0.5 m bins.

The apparent origins corresponding to the upstream radiating top-derivative events are shown by the farthest upstream microphone pairs in Figure 2.6. These events appear to originate from 2–5 m downstream of the nozzle for 75% ETR in Figure 2.6a and slightly farther downstream

from 3–8 m for 150% ETR in Figure 2.6b. Continuing down the microphone array, the source region broadens as the radiation transitions from forward to aft. Then, the microphones between 4–12 m and 4.5–14 downstream localize the sources of the events to compact histograms which shift downstream. Downstream of this region, the histograms continue to shift downstream slightly and broaden. For 75% ETR, the histograms become spatially less continuous as neighboring microphone pairs do not record many counts in adjacent apparent origin bins. In contrast, at 150% ETR, the mode for each microphone pair shifts slightly downstream until about 20 m where the now broad distribution begins to move back upstream along the lipline. This last result indicates that the events creating the largest derivatives present at the far aft portion of the microphone array at maximum afterburner do not originate from a corresponding far-aft position.

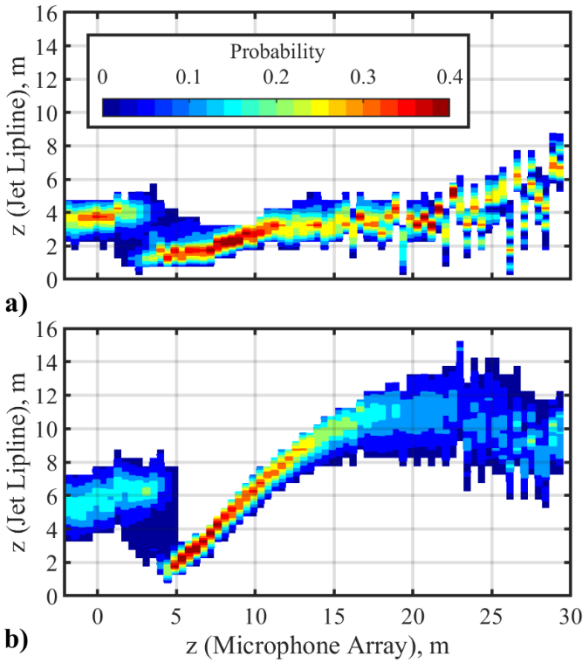

Figure 2.6 Normalized histograms of apparent origin occurrence along the jet lipline across each microphone pair for a) 75% and b) 150% ETR.

2.3.2 Normalized Histogram Mode Comparison Across Engine Condition

Simplifying the results in Figure 2.5 and Figure 2.6 allows for ease of examining trends across engine power for propagation angles and apparent origins. Each histogram is reduced to its distribution mode (with a 1° or 0.5 m resolution) and are shown in Figure 2.7. While both the mode and mean show similar trends, the mode better represents the dominant trend in the transition region from upstream to downstream propagation, where there is not a smoothly varying transition but a bimodal distribution. The inclusion of 100% and 130% ETR demonstrate intermediate cases for the previously analyzed 75% and 150% ETR.

While exhibiting similar features across engine conditions, notable differences exist. At the farthest upstream microphone locations, the propagation angle decreases with increased engine condition making the apparent origin shift downstream. The transition region from upstream to downstream propagation occurs farther downstream along the microphone array for higher engine conditions. Beyond the transition region along the array, higher engine conditions continue to have decreased angle or increased apparent origin, though the amount varies along the array. Immediately downstream of the transition region, minimal change in propagation angle is experienced at ETR greater than 75% with the region persisting over a greater span for higher engine conditions. This corresponds to the steady increase in lipline origin in Figure 2.7b from 4–15 m. Above 75% ETR, while maintaining downstream propagation, an transition point where the apparent origin along the lipline shifts from an upward to downward slope is shown in Figure 2.7b at about 15 m for 100%, 17 m for 130%, and 25 m for 150% ETR. Beyond this region for 100% ETR, propagation angles increase to be nearly identical to 75% ETR from 19 m to the end of the array, yielding similar apparent origins. At 130% ETR, 27 m to the end of the array is nearly identical to lower engine conditions, and while 150% ETR does decrease, it does not match those

of lower engine conditions. This trend at the end of the array is interesting to note as the Sk{∂p/∂t} values seen in Figure 2.8 vary greatly in this region where propagation angles and apparent origins are similar.

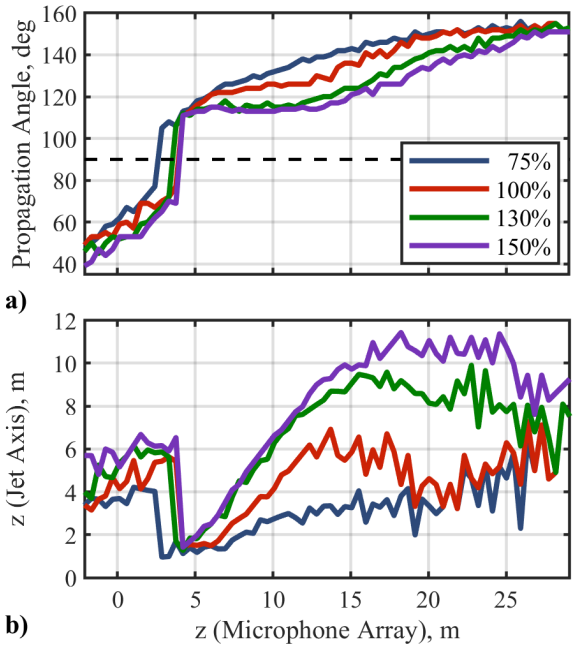

Figure 2.7 Comparison across ETR of the normalized histogram mode along the microphone array for a) propagation angle and b) apparent origin.

2.4 Event-based Beamforming Analysis

To better identify source regions important to crackle perception in the field, microphone pairs are sorted into groups using criteria suggested in Section 2.4.1. Criteria used include the propagation angles found through the event-based beamforming, the measured Sk{∂p/∂t}, and measured OASPL. The groupings are then assigned a color for distinction and examined graphically. Normalized histograms of the apparent origins calculated from the compilation of all microphone pairs for each group are presented and compared with other similar studies in Section 2.4.3, followed by a discussion in Section 2.4.4 of potential jet noise phenomena associated with crackle.

2.4.1 Microphone Pair Groupings

For each engine condition, microphone pairs are placed into one of six groups. The grouping criteria build on previously developed criteria for the four groups used to analyze 75% ETR in Ref. 24. The critera for those four groups plus the two additionally established groups in this study are displayed in Table 2.1. Criteria are defined using trends in the beamformed angle of the derivative events as well as the Sk{∂p/∂t} and OASPL measured at the reference microphone within the pair. The first criteria for categorizing the microphone pairs is whether the radiation direction is upstream (<90°) or downstream (>90°) from the source to the array and whether or not the directionality is changing along the array or unidirectional (which is defined as less than 2° changes compared to adjacent microphones pairs for the purposes of this work, denoted by <Δ2°), as determined by the mode of the beamformed propagation angles. The second criteria is whether or not the Sk{∂p/∂t} is greater or less than 3, indicating that continuous crackle would be perceived by an observer at the array.[8] It should be noted that the relationship of Sk{∂p/∂t} to crackle perception in Refs. 8 and 9 was made using far-field data from the 305 m arc. The Sk{∂p/∂t} is expected to continue to grow beyond the array due to nonlinear propagation by as much as 1000% at 75% ETR from near the shear layer to 38 m.[48] The final criteria for group distinction is whether or not the microphone pair is upstream, downstream, or in the vicinity of a peak in the OASPL measured along the array. The first, primary peak is at about 10 m and the second, lower peak is just beyond 22 m along the array. Application of these criteria to the microphone pairs for each of the four engine conditions generates six distinct groups.

Table 2.1 Number, color, and the three criteria associated with each of the six microphone pair groups.

Group #	Color	Angle	Sk{∂p/∂t}	OASPL
1	Blue	<90°	<3	Upstream
2	Red	>90°	<3	Upstream
3	Purple	<Δ2°	>3	1st Peak
4	Green	>90°	>3	1st Peak
5	Yellow	>90°	>3	2nd Peak
6	Orange	>90°	<3	Downstream

Groups are numbered by their occurrence from upstream to downstream along the microphone array. Each adjacent group generally shares one or two common criteria, as each trend for the most part is smoothly varying along the array. One abrupt trend is in propagation angle and is exemplified by upstream propagation from source to array of group 1 (blue), which is easily distinguished from all the others groups that display downstream propagation. With their primary difference in propagation angle, groups 1 and 2 (blue and red) both are not considered to 'continuously crackle' and have low OASPLs that are spatially located upstream of the 1st OASPL peak. Groups 3–5 (purple, green, and yellow) all exceed the threshold at the array for 'continuous crackle' perception. While both groups 3 and 4 (purple and green) propagate downstream and are part of the 1st peak in the OASPL, distinction between them is the unidirectional radiation of group 3 (purple), defined by less than 2° change in propagation angle between adjacent microphone pairs. Group 5 (yellow) differs from group 4 (green) by appearing in the 2nd OASPL peak with its accompanying abrupt change in Sk{∂p/∂t} at the lower engine powers. The spatial relation to the OASPL peaks is also used to differentiate group 2 (red), which occurs upstream of the 1st OASPL peak, from group 6 (orange) that is found downstream of the 2nd OASPL peak at the end of the array.

The three criteria are plotted along the microphone array for 75%, 100%, 130%, and 150% ETRs in Figure 2.8. Engine conditions are noted by marker while colors signify the group classification as noted in Table 2.1. This allows for comparison of criteria across group and ETR. The Sk{∂p/∂t} shown in Figure 2.8a increases slightly with increased ETR and yields a similar trend across all engine conditions up to 22 m along the array, at which point the Sk{∂p/∂t} diverges with greater values at lower engine conditions. It is curious that Sk{∂p/∂t} increases with lower OASPL at lower engine conditions at the end of the array. Previously-made spatial Sk{∂p/∂t} maps by James *et al.*[19] from data collected at off-ground microphone arcs for the same F-35 measurement and by Gee *et al.*[48] for an earlier F-35 dataset show that Sk{∂p/∂t} generally decreases with downstream distance after peaking, as is seen with 150% ETR in Figure 2.8a. In comparison, it is noted that the Sk{∂p/∂t} values measured at the ground array in this study are higher than at nearby off-ground microphone locations reported in Ref. 19. A possible cause for increased Sk{∂p/∂t} values at the ground is nonlinear reflections of shocks causing a greater than doubling of pressure for the shock events.[49,50] Further investigation into these phenomena should lend insight into understanding crackle and measurement considerations for Sk{∂p/∂t}.

Unlike the Sk{∂p/∂t} with a diverging trend at the end of the array, the OASPL is more smoothly varying across the array for each engine condition. The OASPL is shown in Figure 2.8b as a function of downstream distance along the array and has a consistent trend across engine conditions. The main peak in the OASPL occurs at 10 m and a second, smaller peak occurs at 22 m. Levels increase with engine condition, except about the main peak where the levels decrease slightly from 130% to 150% ETR. The first peak shifts slightly upstream and broadens with engine power, while the second peak occurs at the same location but with a steeper roll off towards the end of the array at higher engine conditions. Though the levels plotted in Figure 2.8 are directly

computed from the data, the second peak in the OASPL is more pronounced when the levels are spatially normalized to a common reference distance, as seen in Ref. 24, and is associated with the region with higher Sk{∂p/∂t} at lower engine conditions.

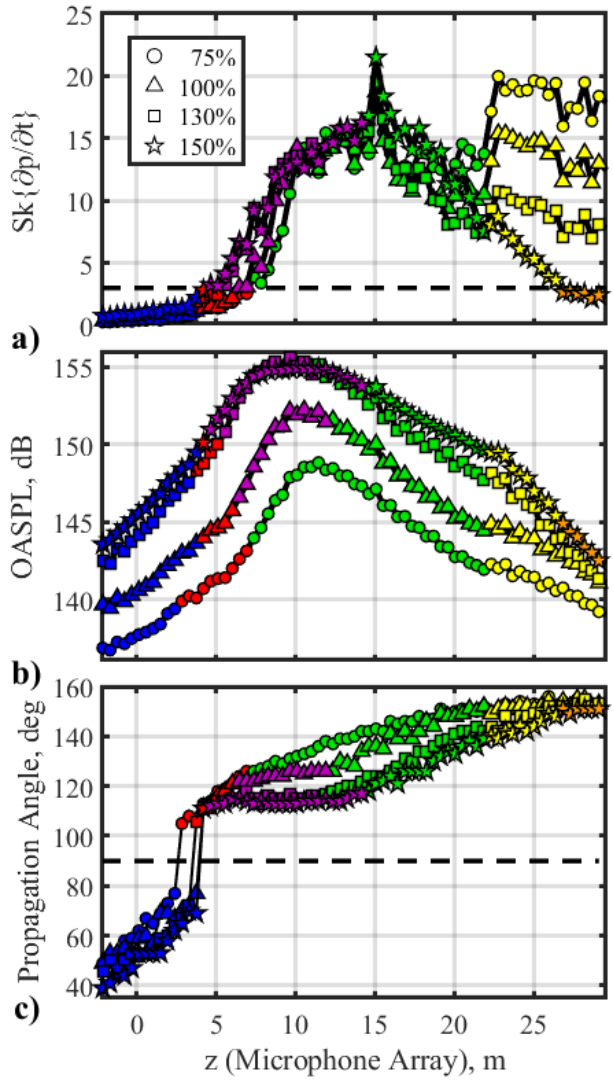

Figure 2.8 Color groupings across engine conditions for a) derivative skewness (Sk{∂p/∂t}), b) overall sound pressure level (OASPL), and c) propagation angle along the microphone array.

2.4.2 Group Source Regions

Groups defined in Section 2.4.1 are associated with apparent origins via the propagation angles of the beamformed events. The mode of the angle distribution for each microphone pair are

used to draw a line from the array back to the nozzle lipline to create a visual representation of the event-based beamforming results in Figure 2.9. These traced lines are color coded to represent their grouping and are shown for each engine condition with a schematic of the F-35, the nozzle lipline, the approximate location of the shear layer, and the array location. Also depicted in Figure 2.9 below the jet axis are lines summarizing the region where all the events associated from that group originate. The extent represents the 5^{th} and 95^{th} percentile bounds, and the diamond marker notes the location of the mean. Table A.1 and Table A.2 summarize this information as well.

The upstream radiation of group 1 (blue) intersects at the nozzle lipline in the same region as groups 3 and 4 (purple and green), though there is less intersection with group 4 (green) at higher engine conditions. Group 2 (red) originates farthest upstream and has a broad overall source region. Group 3 (purple) starting at 100% ETR (see Figure 2.9b) has parallel rays that persist over a broad range for both microphone pairs and apparent source region, which increases with engine condition. When compared to group 3 (purple), the rays for group 4 (green) converge to more localized source region, which is primarily downstream of the apparent origin of group 3 (purple) for engine conditions greater than 75% ETR. Group 5 (yellow) has a similar source region as group 4 (green) with the rays farthest downstream along the array crossing over other rays to upstream locations. This crossover behavior is also exemplified by group 6 (orange) at 150% ETR.

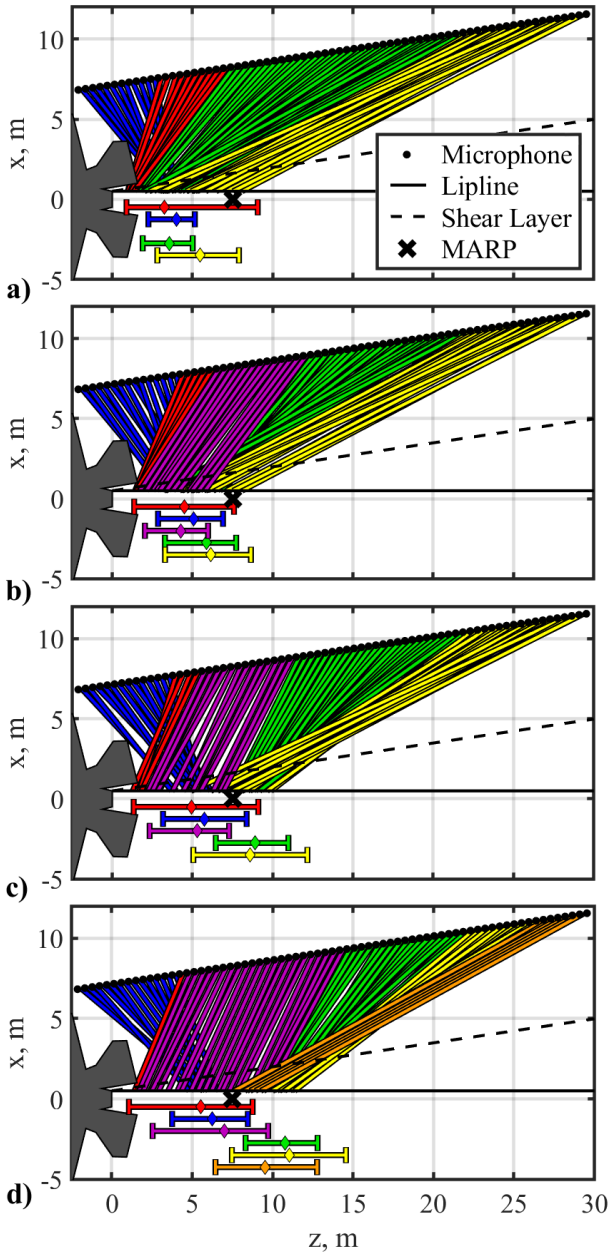

Figure 2.9 Ray tracings of the angle mode for each microphone pairing for a) 75%, b) 100%, c) 130%, and d) 150% ETR. Color bounds below the lipline denote the 5% and 95% with the mean shown as a diamond for the compiled distribution for each group.

2.4.3 Normalized Group Histograms

Distributions of the apparent origins for all the individual events associated with each group are compiled into normalized histograms in Figure 2.10. Despite each group sharing similar

angular, Sk{∂p/∂t}, and OASPL trends across engine conditions, their apparent origins primarily shift downstream as engine condition is increased. The distribution for group 1 (blue) broadens slightly and shifts downstream with the mode increasing from about 4 m to 6 m with increased ETR. Group 2 (red) maintains a peak at less than 2 m downstream of the nozzle with increased engine condition but has a more pronounced bimodal distribution. The portion of the distribution downstream of 3 m for group 2 (red) overlaps with the distribution of group 1 (blue) that radiates upstream. Group 3's (purple) distribution shifts downstream and broadens significantly due to the unidirectional radiation persisting over a greater range with increased engine condition. Group 4 (green) is consistently downstream of group 3 (purple), maintains a more consistent distribution width, and shifts downstream with engine condition. Group 5 (yellow) has a broader source region than group 4 (green) and shifts slightly downstream and broadens with increasing engine condition. However, due to the crossing over of the rays shown above in Figure 2.9, there are source regions for group 5 (yellow) at the jet lipline that are upstream of group 4 (green), as is again demonstrated by group 6 (orange). The total (black) distribution peak is most closely followed by groups 3 and 4 (green and yellow) because a larger number of microphone pairs are associated with these groups and their source regions along the lipline overlap. This trend of source distributions broadening and shifting downstream with increased engine power is consistent with observations of general jet noise trends at all scales and matches the understanding of the stretching of the potential core of the jet with increasing Mach number.[23,41,51]

The motivation for this study is to investigate the origin of crackle-related events in the near field. Examination of the histograms of the origins of the crackle-related groups (groups 3–5, where Sk{∂p/∂t}>3) in Figure 2.10 together show that the corresponding large derivative events originate 1.9–7.9 m downstream of the nozzle along the jet lipline for 75% ETR, 2.0–8.6 m for

100% ETR, 2.3–12.2 m for 130% ETR, and 2.5–14.6 m for 150% ETR, which mirrors the overall distribution in black, meaning that the majority of high-derivative events propagate to locations where an observer would classify the noise as continuously crackling. The majority of events also originate several diameters downstream of the nozzle, which is consistent with the idea that most acoustic energy comes from between the potential and supersonic cores. However, since parameters such as Mach number and temperature of the jet are unknown to the authors, exact description based on potential core lengths is unavailable. Previous studies of high-performance military aircraft[23,51] and laboratory-scale jets[52] have shown that peak acoustic source region to be between 7 and10 diameters. The MARP was chosen as an estimate of the maximum acoustic source region.[11] It is noted that the main source of these large-derivative events denoted by the black line are found several diameters downstream (3–11 m downstream), which differs from several event-based studies which show that intermittent high amplitude events originate from near the nozzle exit,[15,17] which likely suggest that they are not the same phenomenon.

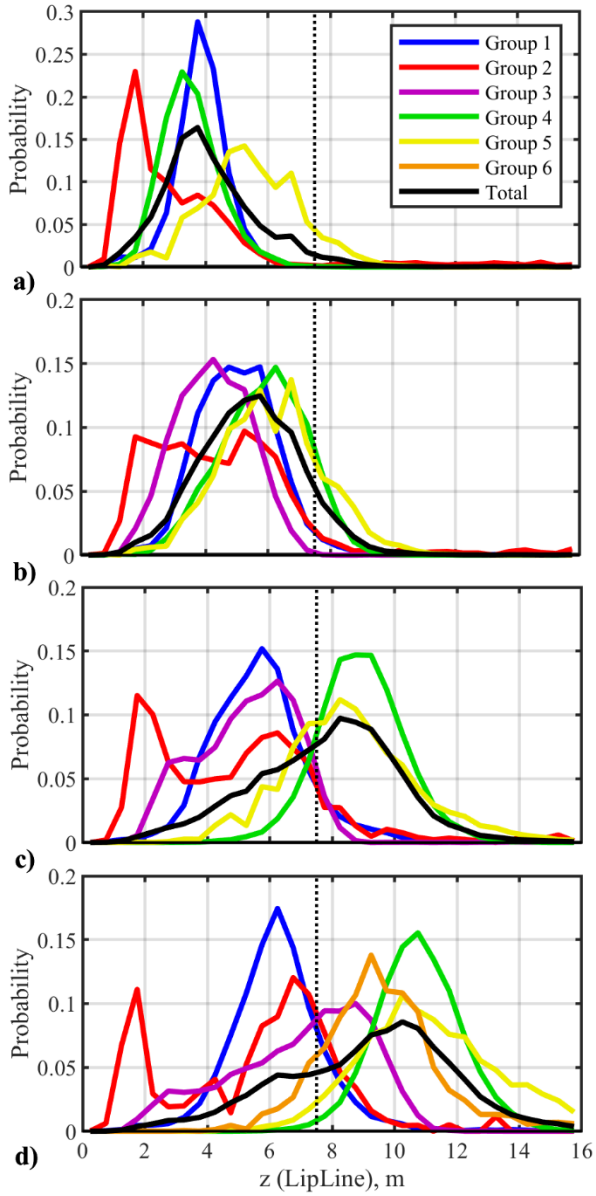

Figure 2.10 Normalized histograms of the apparent origin along the nozzle lipline for all events associated with each group (colored) as well as all the events (black) for a) 75%, b) 100%, c) 130%, and d) 150% ETR. Vertical dotted line indicates the MARP location.

2.4.4 Jet Noise Characterization

In addition to determining the source region of crackle-related events, the characteristics of microphone pair groupings created in Section 2.4.1 help relate groups with particular jet noise phenomena. The non-crackle-related groups are discussed first. The upstream propagation of group 1 (blue) is likely associated with broadband shock-associated noise (BBSAN), which

propagates upstream and is a dominant noise component at these locations in recent spectral characterizations.[22] Group 2 (red) also appears partly associated with BBSAN as its source region partly overlaps with group 1 (blue) in Figure 2.10 and perhaps with its broad source distribution is also related to fine-scale turbulence structure noise that conceivably has numerous sources along the jet plume.[53,54]

Examination of the individual crackle-related groups provides insight into different jet noise source phenomena. While both groups 3 and 4 (purple and green) are related to the main OASPL peak measured along the array, group 3 (purple) is characterized by a nearly-constant radiation angle, consistent with the description of Mach wave radiation[29] stemming from a nearly constant supersonic convective velocity that is characteristic of the potential core. This suggests that one difference between groups 3 and 4 (purple and green) is that the events are originating from either upstream or downstream of the collapse of the potential core. One can infer from this observation that the potential core persists between 5–6 m downstream of the nozzle for 100% ETR, 6.5–7.5 m downstream for 130% ETR, and between 9–10.5 m for 150% ETR.

Recent coherence analysis of a large eddy simulation of a laboratory-scale jet operating at a temperature ratio of 7 (to be on the order of a military aircraft operating at afterburner)[55] shows that source mechanisms upstream of the potential core radiate in the unidirectional pattern exemplified by group 3 (purple) here. Additionally, the source of coherent energy between the nozzle lip line and the aft field of the simulated jet qualitatively changes in the region downstream of the potential core, characteristic of less efficient, more omnidirectional radiation of the large-scale turbulent structures as they become convectively subsonic. This source mechanism was observed to be spatially large and centered around the end of the supersonic core. Groups 4 and 5 (green and yellow) overlap and exemplify well this behavior. This overall trend is also observed

by Schmidt *et al.*,[56] who did spectral proper orthogonal decompositions of subsonic, transonic, and supersonic jets. They found that upstream of the potential core, the low-rank decompositions were of compact wavepacket shape in the shear region of the jet, while downstream of the potential core the modes were not low rank with many overlapping, spread out modes with lower phase velocities. These two wavepacket types were named Kelvin Helmholtz and Orr-type wavepackets respectively, due to their probable source mechanisms. It is possible that these phenomena are responsible for driving the generation of steep acoustic shocks and therefore crackle perception in the near field.

The differences between group 3 (purple) and groups 4 and 5 (green and yellow) are also observed when comparing two studies which use event-based inverse methods similar to the current work. Schlinker *et al.*[47] and Hileman *et al.*[43] used a similar cross-correlation beamforming method but with large amplitude events as the triggers. For a full-scale engine at full power, Schlinker found the source locations along the jet axis to be concentrated at 5 diameters downstream, whereas Hileman found for a cold model-scale jet at three Mach numbers the peak in the distributions to be about 9–10 diameters downstream. Schlinker explains some of the differences are in part due to their placement of sensors at 135° relative to the nozzle compared to 160° for Hileman's study. These results are corroborated in the current work, which suggests that the sensor placement for Schlinker would measure events related to group 3 (purple) and Hileman to groups 4 and 5 (green and yellow). Furthermore, Schlinker also proposes that Hileman's distribution correspond to the more dominant large-scale turbulent structure mechanisms at the end of the potential core rather than Mach wave signature captured in their study.

2.5 Conclusions

This study has identified acoustic source regions along the nozzle lipline of a military aircraft that correspond to higher crackle percept[8,9] in the near field by an event-based beamforming method. Short windowed segments of the waveform around 1000 of the highest derivative values are chosen as events in the beamforming process. Six distinct microphone pair groupings have been defined, with particular interest given to those that exceed the criterion for continuous crackle (groups 3–5 (purple, green, and yellow), $Sk\{\partial p/\partial t\} > 3$). These three crackle-related groups propagate downstream but have differing source locations and directivities. Events beamformed from group 3 (purple) display unidirectional radiation and likely originates from the potential core region, consistent with the description of Mach wave radiation.[15,29] Groups 4 and 5 (green and yellow) likely originate downstream of the potential core and appear similar to large-scale turbulent structure noise. Additional work is undertaken to determine the relationship of these near-field shock events to far-field crackle perception in Chapter 4. Community response to jet crackle, the relationship between far-field crackle perception, and the results of this study are of importance for future research.

Chapter 3
Nonlinear Shock Reflections near Military Aircraft

3.1 Introduction

This study investigates the possibility and implications of nonlinear shock reflections for acoustic shocks contained in jet noise produced by a high-performance military aircraft. Acoustic shocks are characterized by abrupt changes of properties in the medium, such as pressure, temperature, and density. In jet noise, shocks are intermittent events embedded within other jet noise components, occurring particularly in the loud, aft radiation region. Shocks have been shown to be present in the near field[16,26] as well as in the far field, [57] though far-field shocks are augmented due to nonlinear propagation.[11] The reception of acoustic shocks are responsible for the perception of jet crackle,[46] which is as an annoying[2] and dominant[3] component of supersonic jet noise. The skewness of the time derivative of the pressure waveform (Sk{∂p/∂t}, hereafter referred to as the "derivative skewness") is a metric indicative of the crackle percept in jet noise,[8] as it is sensitive to the presence of acoustic shocks in the jet noise waveform.[57] Of interest in this study is how ground reflections impact shocks in jet noise and the subsequently measured Sk{∂p/∂t} values.

There is a debate over the placement of microphones at ground or off-ground locations for measuring and characterizing jet noise. The American National Standards Institute/Acoustical Society of America standard for measuring high-performance military jet aircraft dictates off-ground placement of microphones for measuring tied-down aircraft emissions. Off-ground placement simulates the position of an observer's ear and for some flyover measurements have been shown to provide cleaner data for measuring acoustic nonlinearities,[58] though ground

interference nulls result in the spectra due to such placement.[59] While there are methods to address ground interference effects,[60,61] there are a number of studies that rely acoustical data collected at ground-based arrays for full-scale military aircraft.[20,62,63] Placement of microphones on the ground eliminate interference nulls, though due to the immediate reflection at the microphone-surface interface, there is an increase in the measured pressure compared to a free-field measurement. In addition to increased pressure, there has been an increase in derivative skewness values at the ground relative to the air,[18] for reasons that have not been understood. The potential for nonlinear reflections of acoustic shocks at ground locations, however, has not been directly investigated in the context of jet noise.

There are a variety of classifications for nonlinear reflections. Ernst Mach in 1878 first classified shock wave reflections as either regular or irregular.[64] Regular reflections (RR) consist of two shocks; an incident and a reflected shock (as seen in Figure 3.1a). The amplitudes and angles of incidence relative to the surface of the incident and reflected shocks can differ slightly for RR and do not follow the linear reflection described by Snell-Descartes laws. In addition to the incident and reflected shocks, irregular reflections (IR) have a third shock called the Mach stem that travels parallel to the surface, as can be seen in Figure 3.1b. Mach stem formation is due to changes in the medium induced by the incident shock causing the reflected shock to travel faster and coalesce with the incident shock. The intersection of the three shocks in an IR is called the triple point. While there are several subsets of IR based on the shock strength or flow deflection processes,[65,66] for weak shocks (acoustic Mach numbers below 0.47)[67] there are two types of IR: von Neumann Reflection (vNR) and Weak von Neumann Reflection (WvNR). These shock reflection types are named for the von Neumann Paradox,[68,69] which is the inability of von Neumann's three-shock theory[70] to predict irregular reflections for weak shocks. Unlike IR for

strong shocks, or Mach reflections,[66] that have a slope discontinuity at the triple point, vNR have no slope discontinuity between the Mach stem and the incident shock, as visualized in Figure 3.1b. Only a single, incident shock results for WvNR due to a shock being at grazing incidence with the surface, as pictured in Figure 3.1c.[71]

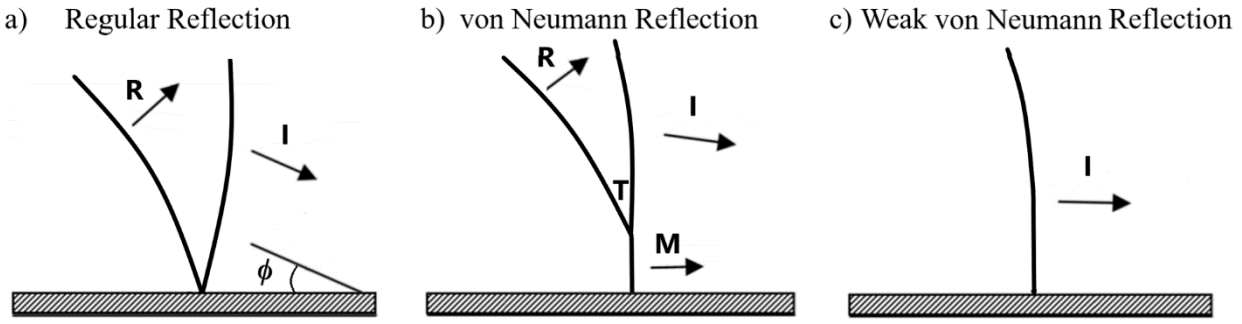

Figure 3.1 Weak shock reflection schematics similar to Figure 3 in Ref. [71], Figure 1 in Ref. [72], and Figure 1 in Ref. [73].

The pressure amplitude at the ground due to the Mach stem of an irregular (or nonlinear) reflection is greater than a linear reflection. Two-dimensional simulations of shocks reflecting on a rigid boundary performed by Desjouy *et al.*[73] showed the peak-to-peak pressure approaching a factor of 2.5 for the 3-shocks regime, as opposed to doubling in the linear 2-shocks regime described by Snell-Descartes laws. The 1-shock regime for WvNR are expected to have less than a doubling of pressure. Marchiano *et al.*[50] experimentally validated the peak-to-peak pressure increasing by a factor of 2.5 for the Mach stem of vNR of weak shock waves in water. If the shocks in a jet noise waveform undergo a nonlinear, irregular reflection at the ground and their peak-to-peak amplitude increase by a factor greater than two, while the remainder of the waveform increases by a factor of two, it is hypothesized that there are characteristic differences between the waveforms measured at the ground in the air: the ground waveform has a higher ratio of energy in the shock to the overall energy and thus may affect the perception of crackle.

Generally, experimental identification of shock reflection type is performed by imaging the shock reflection pattern using techniques such as schlieren imaging[49,50,69,74] and shadowgraphy.[66,75] However, because shocks were not visualized directly for reflection identification during the jet noise measurements, a method is used to identify the potential shock reflection type that involves a parameter based on measured shock characteristics. Based on theory and validated by experimental results, a critical parameter, a, has been proposed to bound the regime for a given shock reflection classification.[76] The critical parameter originates from the application of boundary conditions on the Khokhlov-Zabolotskaya equation[77] and is defined as:

$$a = \frac{\sin(\phi)}{\sqrt{2\beta M_a}}, \qquad \textbf{Equation (3.1)}$$

where ϕ is the angle of incidence relative to the ground (see Figure 3.1a), β is the coefficient of nonlinearity of the propagation medium, given as $\beta = (\gamma + 1)/2$ with γ as the ratio of specific heat of the medium, and M_a is the acoustic Mach number. Physically, the acoustic Mach number is the ratio of the maximum particle velocity at the shock to the ambient sound speed in the medium, but can be calculated using pressure measurements as follows:

$$M_a = \frac{\Delta P}{\gamma P_{\text{atm}}} \qquad \textbf{Equation (3.2)}$$

where ΔP is the peak-to-peak shock pressure, P_{atm} is the atmospheric pressure, and γ is the ratio of specific heat of the medium.[76] For a given medium, the critical parameter value depends only upon the angle of incidence and acoustic Mach number. For weak acoustic shocks or N-waves, Baskar *et al.*[76] theoretically predicts $a = 0.4$ as the transition from WvNR to vNR and $a = 0.8$ as the transition from vNR to RR. Experimental validation by Karzova *et al.*[71] indicated transitions boundaries at $a = 0.38$ and $a = 1.05$ for individual shock pulses where $M_a = 0.044$ and

transitions at $a = 0.58$ and $a = 1.1$ for shocks where $M_a = 0.006$. Similarly, Marchiano *et al.*[50] indicated for ultrasonic pulses in water the transitions at $a = 0.36$ and $a = 0.91$. Leete *et al.*[78] studied gaseous explosions reflecting over a hard ground and found that the transition point from regular to irregular reflection occurred at $a > 0.8$, though they observed a discontinuity between the Mach stem and incident shock, suggesting that the transition occurred while the shock strength was sufficient to strong shock. Represented in M_a-ϕ space, Figure 3.2 shows the transitional critical parameter values used in this study: $a = 0.4$ as the transition between WvNR and vNR and both $a = 0.8$ and $a = 1.1$ as the transition between vNR and RR from the theoretical and experimental results. The transition at $a = 0.4$ for WvNR and vNR is theoretically predicted and validated by experiments with similar M_a values to the shocks in the present study. It is anticipated that the transition from RR to vNR occurs at $a > 0.8$, but due to lack of visual confirmation, the two a values are used to bound the maximum a value for potential occurrences of vNR based on the theoretical prediction and experimental findings.

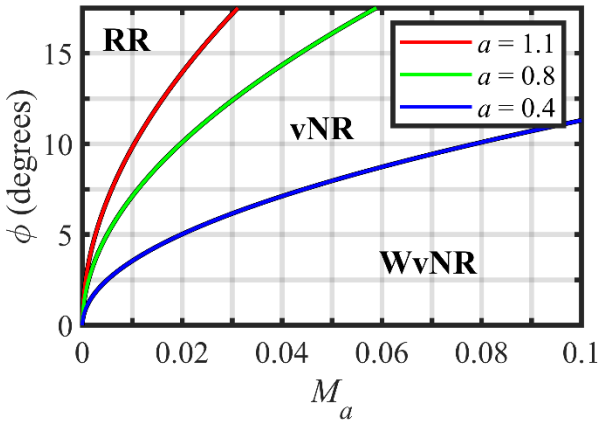

Figure 3.2 Shock reflection classification in M_a-ϕ space based on transitional critical parameter values.

The goal of this paper is to identify differences between ground and off-ground jet noise measurements and provide evidence for the occurrence of irregular shocks as a partial explanation for these differences. The possibility for the occurrence of irregular reflections at the ground-based

microphone array pictured in Figure 1.1 is evaluated by calculating the acoustic Mach number and implementing an event-based beamforming method to identify the angle of incidence relative to the ground for an ensemble of acoustic shocks, then computing the critical parameter, a, value for each event. An explanation of the shock strength and event-based beamforming method and shock strength calculation are first presented. Predictions of shock reflection type for shock-like events across the entire array are then provided, after which the percentage of shocks expected to undergo vNR are discussed in relationship to elevated derivative skewness values.

3.2 Shock Reflection Prediction Methods

Two event types of interest related to acoustic shocks are first defined. For each event of interest, the acoustic Mach number and angle of incidence are determined so that the critical parameter can be calculated and used to predict potential shock reflection type.

3.2.1 Shock Characterization

The first event type of interest are the largest 100 derivative events in the 10-s waveforms. Due to the two-point cross-correlation in determining the angle of incidence, events are defined in the upstream microphone for the 70 adjacent microphone pairs along the entire array. While well-defined shocks may not exist at all locations along the array, this event definition provides the steepest portions of the waveform that likely have the largest shock strengths and are therefore the most likely cases for irregular shock reflections to occur. These events are determined in the same manner as events examined in the event-based beamforming process developed in Section 2.2.

The second event type of interest in this study are acoustic shocks as defined by the following criterion: An event where the derivative of the pressure waveform exceeds 15 times the

standard deviation of the derivative waveform ($15\sigma_{\partial p/\partial t}$) is considered to be a shock.[57] This statistical criterion was chosen to differentiate the large derivative outliers common for shock waves from the other components of jet noise. Though the criterion is sensitive to sampling frequency, this dataset satisfies the sampling frequency requirement suggested by Reichman *et al.*[79] of at least 100 times the characteristic frequency, which is 100–200 Hz.[22]

Values for $15\sigma_{\partial p/\partial t}$ criterion and the resulting shock counts along the microphone array for the four engine conditions of interest are shown in Figure 3.3. Though the criterion changes with distance, it is normalized to the variation within a given waveform because of its use of the standard deviation. The following two spatial trends for the $15\sigma_{\partial p/\partial t}$ criterion are similar to OASPL trends in Figure 2.8b: first, the values at all engine conditions as a function of downstream distance increase, peak at $z \approx 10$ m, and then decrease along the array, and second, as a function of engine power, the values increase from 75% to 130% ETR and then have similar values at the two afterburner conditions (130% and 150% ETR), suggesting that the derivatives generally go up when amplitude goes up. Interestingly, for $z > 20$ m, the $15\sigma_{\partial p/\partial t}$ criterion converges to having nearly identical values at all engine conditions.

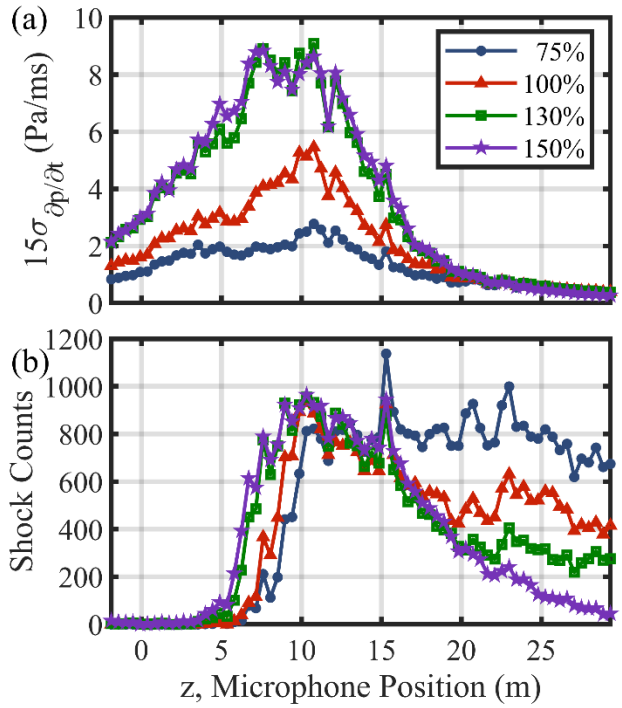

Figure 3.3 (a) Shock criteria of $15\sigma_{\partial p/\partial t}$ based on Ref. 57 and the (b) shock counts along the microphone array.

While the shock criterion identifies a number of shocks in the majority of channels along the ground array as shown in Figure 3.3b, there are locations $z < 5$ m that have no shock counts. On the other hand, caution is needed to make certain that shocks are not double counted, because if time waveform is sufficiently steep and sampled fast enough, multiple samples tracking the pressure rise of an acoustic shock may satisfy the $15\sigma_{\partial \mathrm{p}/\partial \mathrm{t}}$ criterion. The spatial trend across the entire array of shocks counts is strongly correlated to the derivative skewness shown in Figure 2.8a, which is particularly interesting for $z > 20$ m where the shock counts increase with lower engine powers. As there are no shocks identified by the $15\sigma_{\partial \mathrm{p}/\partial \mathrm{t}}$ shock criterion at several locations for $z > 5$ m, the use of the first event type of interest, the top 100 largest derivative events, is justified by providing a means to examine potential for nonlinear reflections across the entire array. Where there are no shock counts according to the shock criterion, irregular shock reflections are not expected and the classification of the events as exhibiting regular shock

reflection is anticipated, though they may actually be linear reflections, as only shocks may be characterized using shock reflection classifications.

3.2.2 Shock Strength

To represent shock strength, this study utilizes the acoustic Mach number, M_a, as defined in Equation (3.2). There are other viable metrics such as the pressure ratio, density ratio, or shock Mach number that may also be used for shock strength characterization. The use of M_a in Equation (3.1) is the primary motivation for the choice of M_a to quantify shock strength. An example waveform segment demonstrating measures used to calculate M_a is shown in Figure 3.4 with a derivative event and upper (P_2) and lower (P_1) peak pressures marked. Because shocks are defined within continuous noise, $\Delta P = P_2 - P_1$ rather than being equal to P_2, as would be the case for a single shock event in a quiescent environment.

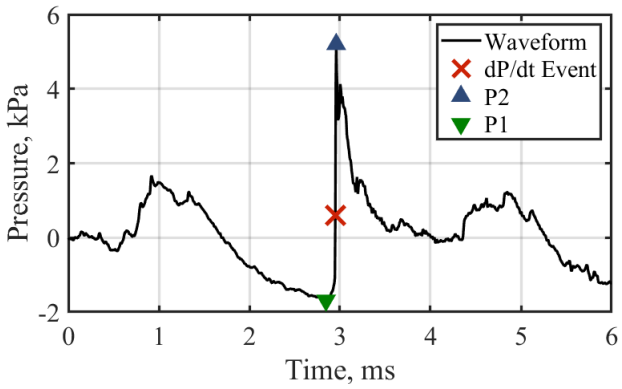

Figure 3.4 Example waveform segment of a large derivative event with the upper and lower peak pressures noted.

3.2.3 Angle of Incidence

The method implemented to determine the angle of incidence, ϕ, used to calculate the critical parameter in Equation (3.1) is similar to the event-based beamforming procedure described in Section 2.2.2 and visually depicted in Figure 3.5. First, a two-point cross-correlation is

performed to determine the propagation angle, ψ, for an event of interest. For each event defined in upstream channel of the 70 adjacent microphone pairs, a 20-ms Hann window is applied about the large derivative or shock event. Then the event is compared with a similarly windowed waveform segment recorded by the adjacent downstream microphone. The window was chosen to be long enough to obtain a meaningful cross-correlation but short enough to isolate the energy of just the shock and not the underlying jet noise. From the cross-correlation between the two windowed waveform segments, a time lag, τ, is calculated and used along with the speed of sound, c, and the inter-microphone spacing distance, Δd, to determine the event's propagation angle, ψ, as follows:

$$\psi = \cos^{-1}\left(\frac{c \cdot \tau}{\Delta d}\right). \qquad \textbf{Equation (3.3)}$$

This angle is visually depicted in Figure 3.5. Due to the placement of the microphone pair on the ground, the propagation angle contains only x-z plane propagation and no vertical information. Therefore, a source location along the jet nozzle lipline at $(x, y) = (0.5, 2)$ m is assumed to provide a height, h, at $\mathrm{y} = 2$ m from which an angle of incidence relative to the ground may be determined. Though the shock may originate at the shear layer or any point along the path, the jet lipline is used in congruence with the previously performed event-based beamforming study in Chapter 2. (If the jet nozzle centerline were used instead, ϕ would decrease in the maximum radiation region by only about 0.2° or at most by 1° at far upstream locations.) The propagation pathlength, d, (red line in Figure 3.5) is found by tracing the propagation angle from the microphone pair midpoint to the jet nozzle lipline (black dashed line in Figure 3.5). The angle of incidence, ϕ, is calculated as follows:

$$\phi = \sin^{-1}\left(\frac{h}{d}\right) \qquad \textbf{Equation (3.4)}$$

Grazing incidence is 0° and normal incidence is 90° for ϕ in this orientation. This process is repeated for each event of interest, resulting in a unique (M_a, ϕ) pair and a value for each event.

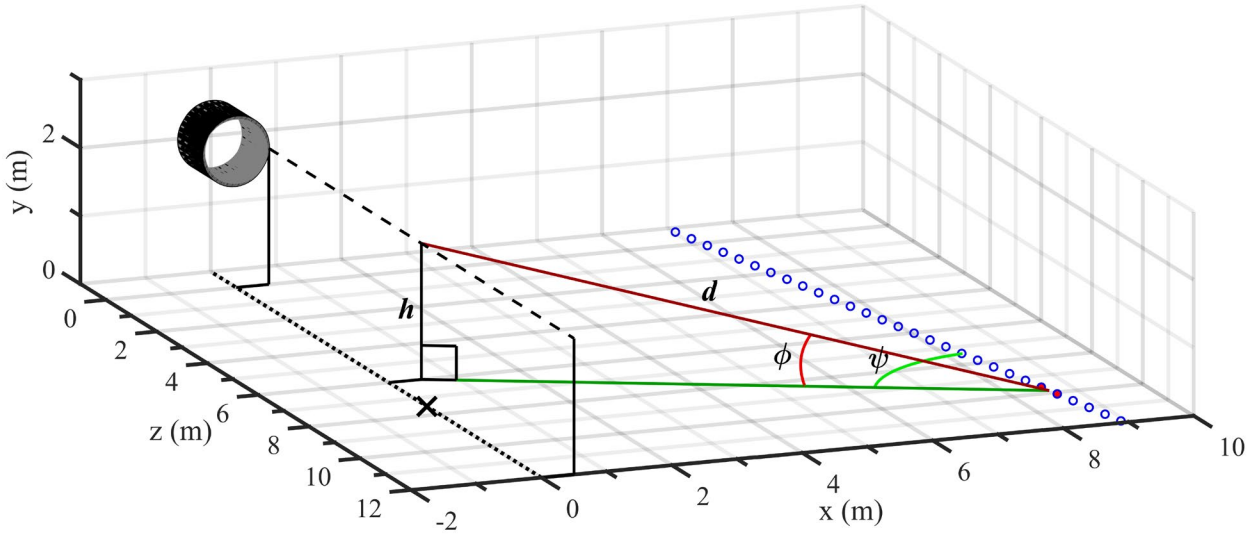

Figure 3.5 Angle of incidence beamforming schematic with the jet nozzle represented by a cylinder, microphones along the ground array noted by blue circles, and the MARP marked by a black x.

3.3 Ground and Off-ground Shock Comparisons

Before the examining the results for the shock reflection classifications of the events of interest, differences are presented for shocks measured at ground and off-ground locations. Discrepancies between ground and off-ground measurements in derivative skewness values may exist due to the presence of nonlinear ground reflections. The distance between the ground microphone (located at $z = 9.1$ m) and the off-ground microphone is 0.31 m in the x-z plane (see Figure 1.1) and 0.91 m in the y-direction, as shown in Figure 3.6. To aid in the comparison of the ground and off-ground measurements, a waveform with a simulated linear ground reflection is generated by adding the ground measurement waveform to itself with a time delay corresponding

to the pathlength difference between the direct and reflected path for the off-ground microphone. A 1-ms time delay is calculated for the pathlength differences between the direct and an assumed linear reflected path for the off-ground microphone by assuming a source at the jet nozzle lipline at the microphone array reference point (MARP) downstream location, $(x, y, z) = (0.5, 2.0, 7.5)$ m, as shown in Figure 3.6. The pressure of the simulated-ground-reflection waveform is also halved, to account for a doubling of pressure at the ground as would be expected for a linear reflection off an acoustically rigid surface.

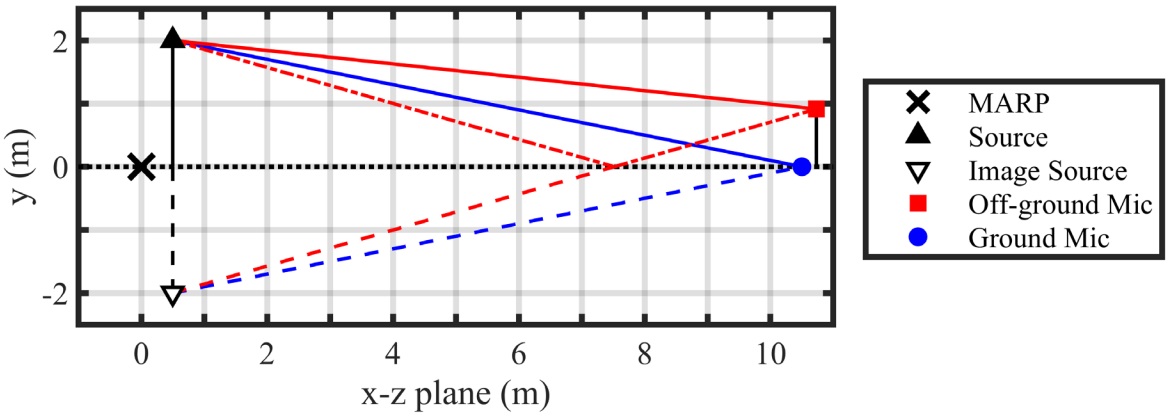

Figure 3.6 Direct and reflected propagation paths for the off-ground microphone with an assumed source at the jet nozzle lipline, $(x, y) = (0.5, 2)$ m, at the downstream distance of the MARP, $z = 7.5$ m.

Probability density functions (PDF) of the pressures and time-derivative pressures for the ground, off-ground, and simulated cases at 150% ETR are provided in Figure 3.7. Each distribution is normalized by its respective standard deviation, and the logarithmic scaling on the ordinate allows for inspection of the distribution tails, which are the drivers of the skewness value due to its cubic nature. The averaged pressure skewness (Sk$\{p\}$) and derivative skewness (Sk$\{\partial p/\partial t\}$) values across five runups at 150% ETR are noted in Table 3.1. The pressure distribution in Figure 3.7a for the simulated waveform approaches that of the off-ground measurement, though the Sk$\{p\}$ values are underpredicted. This suggests that a linear reflection may generally account for the

differences in pressure skewness values for ground and off-ground measurements. The derivative skewness on the other hand is greater for the simulated waveform than is measured off-ground, as given in Table 3.1 While this shows that the derivative skewness value decreases for a linearly simulated reflection compared to a ground measurement, the derivative skewness is still significantly greater, which may partly be attributed to the ground waveform containing nonlinear reflections that inherently cause the simulated waveform to contain stronger shocks than observed at the off-ground location.

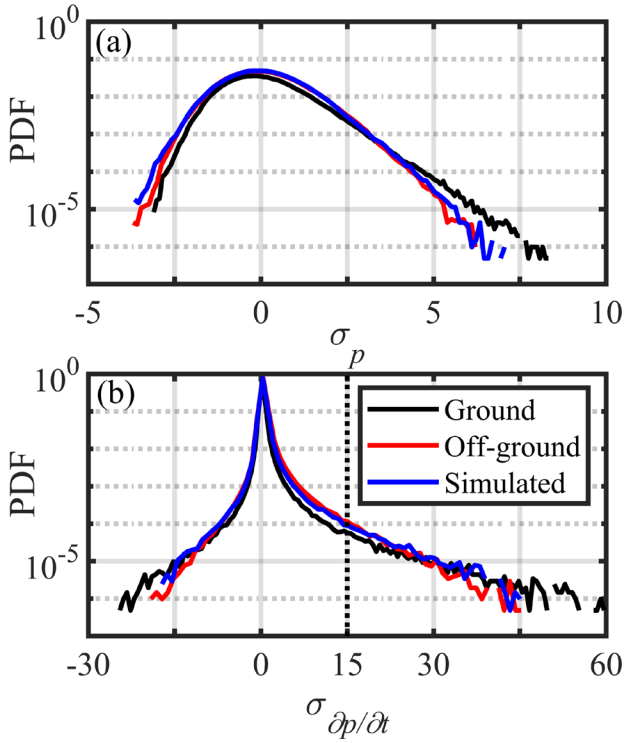

Figure 3.7 Probability density functions of the (a) pressures and (b) time-derivative pressures for ground, off-ground, and simulated waveforms at 150% ETR. The vertical dotted black line in (b) indicates the shock criterion of $15\sigma_{\partial p/\partial t}$.

The application of the $15\sigma_{\partial p/\partial t}$ shock criterion, shown by a vertical dotted black line in Figure 3.7b, yields more shock comparisons with the $15\sigma_{\partial p/\partial t}$ values, shock counts, and averaged maximum derivative value, $\langle\sigma_{\partial p/\partial t}\rangle_{\max}$, also noted in Table 3.1 for 150% ETR. A linear superposition of a delayed shock-containing waveform with itself might suggest that there would

be a doubling of shock counts, however, there are on average 12% more shock counts for the off-ground and simulated waveforms relative to the ground measurement. Fewer shocks at the ground measurement location proposes that there is fundamental difference in the type or strength of shocks at the ground versus off-ground location that causes an increase in derivative skewness values at the ground. The $\langle\sigma_{\partial p/\partial t}\rangle_{\max}$ is greater at the ground than off-ground, suggesting that on average, the shocks measured at the ground are steeper, which would be the case for nonlinear reflections. In addition to this, the ratio of peak-to-peak pressures at the ground relative to the off-ground measurement is 2.3. This increase in pressure is expected for irregular reflections and the value approaches the factor of 2.5 observed by Marchiano *et al*.[50] for irregular shock reflections in water.

Table 3.1 Averaged derivative skewness, pressure skewness, shock criteria, shock counts per second, and average maximum shock derivative values across 5 runs for 150% ETR.

Case	Sk{p}	Sk{∂p/∂t}	$15\sigma_{\partial p/\partial t}$, Pa/ms	Shock/sec	$\langle\sigma_{\partial p/\partial t}\rangle_{\max}$
Ground	0.70	15.9	6.7	86.6	25.9 $\sigma_{\partial p/\partial t}$
Off-Ground	0.41	9.5	4.4	97.8	20.4 $\sigma_{\partial p/\partial t}$
Simulated	0.36	11.2	4.8	97.4	22.9 $\sigma_{\partial p/\partial t}$

3.4 Results for Largest 100 Derivative Events

The ground versus off-ground shock analysis presented evidence for stronger shocks at the ground. Here, the assertion is reinforced that stronger shocks could be due to nonlinear reflections. The feasibility of irregular reflections occurring is examined for the first event type of interest, the top 100 largest derivative events, at each of the 70 microphone pairs along the array. Histograms of spatial variations in acoustic Mach number and angle of incidence are examined for two engine conditions; 75% and 150% ETR. Results in M_a-ϕ space are then presented for shock reflection

classification. To further analyze shock reflection classification, critical parameter value histograms are presented as a function of microphone position. Average values across the top 100 largest derivative events are then used for subsequent comparisons across engine condition.

3.4.1 Acoustic Mach Number and Incidence Angle Histograms

The occurrences of M_a values for the top 100 largest derivative events at each of the 70 microphone pairs are given for 75% and 150% ETR in Figure 3.8. The abscissa is the z-coordinate of the microphones in the array pictured in Figure 1.1 and the ordinate is the array of histogram bins of M_a values calculated for each event in 0.001 increments. The color represents the number of event counts in each histogram bin. Each vertical slice corresponds to a microphone pair for which the sum of the binned event counts is 100. Both engine conditions contain a peak at $z =$ 10–13, similar to the OASPL seen in Figure 2.8b. The peak is broader and contains M_a values nearly double that of 75% ETR at 150% ETR. At either end of the microphone array ($z < 3$ m and $z > 22$ m), where M_a values for both engine conditions are similar, M_a values are higher at 150% ETR for $z < 3$ m. Conversely, for $z > 22$ m, greater M_a values occur on average for 75% ETR.

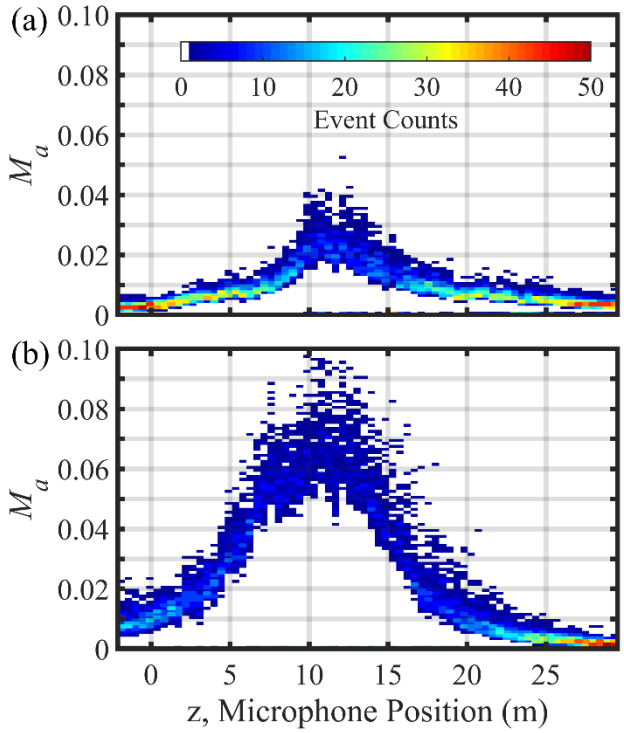

Figure 3.8 Histograms of acoustic Mach numbers, M_a, for the top 100 largest derivative events across each microphone pair for (a) 75% and (b) 150% ETR.

In the same format as Figure 3.8, Figure 3.9 depicts the angle of incidence of each event along the microphone calculated by the beamforming algorithm. The abscissa is the same as in Figure 3.8 with the ordinate now representing histogram bins for angles of incidence in 0.25° increments. For both 75% and 150% ETR, the maximum angle of incidence is approximately 15° and occurs at $z = 2–3$ m, which then incrementally decreases to 5° at the end of the array. However, the rate of decrease is different, with a larger decrease of angle of incidence for $z = 3–20$ m and minimal reduction at $z > 20$ m for 75% ETR. This contrasts with 150% ETR, which has a small drop in angle of incidence for $z < 15$ m and a greater rate of decline for $z < 15$ m. Also, while the distributions are rather narrow for both cases, the distribution are broader for 150% ETR at $z < 5$ m and $z > 15$ m.

The overall trend is most likely influenced by the positioning of the array. The downstream microphone locations are farther away from the jet nozzle lipline, which increases the propagation pathlength in Figure 3.5b and results in smaller angles of incidence. Other differences in angles of incidence between the two engine conditions at a given microhpone location are due to shocks having different source locations. From the event-based beamforming results in Section 2.3, the source region for 75% ETR is more compact and predominantly upstream of the MARP, while the source region at 150% ETR is broader and extends well downstream of the MARP.

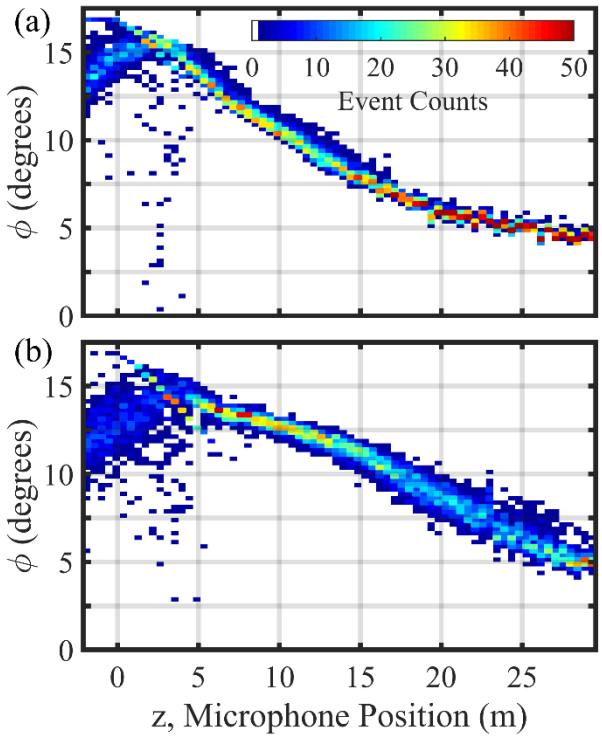

Figure 3.9 Histograms of angle of incidences, ϕ, for the top 100 largest derivative events across each microphone pair for (a) 75% and (b) 150% ETR.

3.4.2 M_a-ϕ Space and Critical Parameter Values

For 75% and 150% ETR, Figure 3.10 shows the locations of the top 100 derivative events in M_a-ϕ space at each of the 70 microphone pairs along the ground array. Black dots represent individual shock events, with reflection regimes noted and bounded by the curved lines denoting

the transitional critical parameter value. Across the entire array, for both engine conditions, 35% of the total 7000 events fall into the $0.4 < a < 0.8$ vNR regime and about 60% in the $0.4 < a < 1.1$ vNR regime, while almost no events fall into the WvNR regime. Regardless which vNR criterion is more appropriate for shocks in jet noise, the results show variability for the top 100 derivative events for a given microphone position is directly related to the spread in the histograms in Figure 3.8 and Figure 3.9, for which the overall trend is smoothly varying with space. The events located in the upper left corner of Figure 3.10 with low M_a and large ϕ are recorded at the upstream microphones. The distribution of events decreases in ϕ and increases in M_a with downstream microphone pair locations until the point along the array is reached with the peak OASPL (at z ≈ 10 m). Then, M_a decreases again as ϕ continues to decrease towards the end of the array.

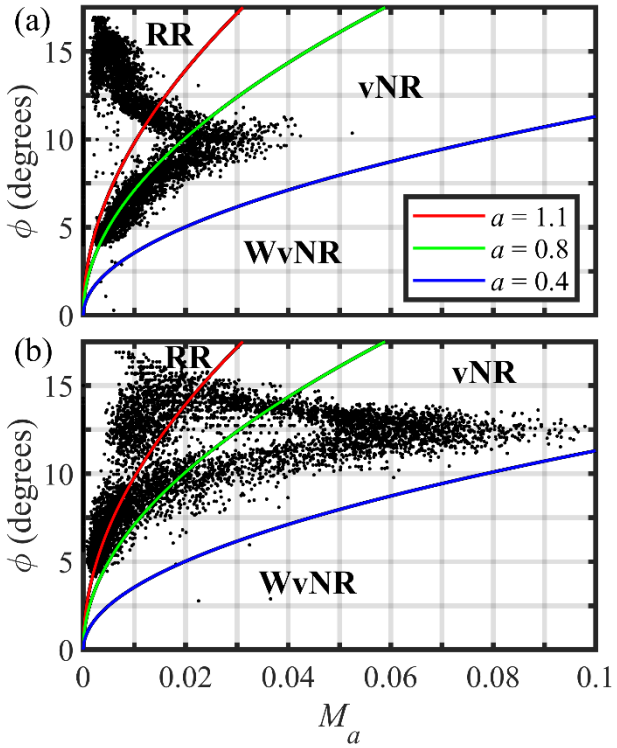

Figure 3.10 M_a- ϕ space results of the top 100 top derivative events for a) 75% and b) 150% ETR. Colored lines indicate transitional critical parameter values.

Spatial and quantifiable trends are more readily identifiable in Figure 3.11, which shows the histograms of calculated a values of the top 100 derivative events at each microphone pair for 75% and 150% ETR. The a values for the events at each microphone location were binned in 0.05 increments, and the horizontal lines represent the two transition criteria that separate the RR and vNR regimes and the one separating the vNR and WvNR regimes. Large derivative events that are not necessarily shocks may end up being classified as RR, though a linear reflection may be more appropriate as a shock reflection classification should not be applicable to a non-shock event. Without visual confirmation of the reflection, RR is the most nonlinear reflection classification that may be assumed for these events. The overall a trend for the two engine conditions in Figure 3.11 is different. For $z < 7$ m, the distribution spread varies significantly for both engine conditions, though the a values are greater for 75% ETR. In the trough region from $z = 7$–15 m, the distributions are the densest along the array. For $z < 15$ m, the distribution for 75% ETR remains moderately dense and centered about $a = 0.8$, whereas the a value increases and the distribution spreads out more for 150% ETR, extending into the RR regime.

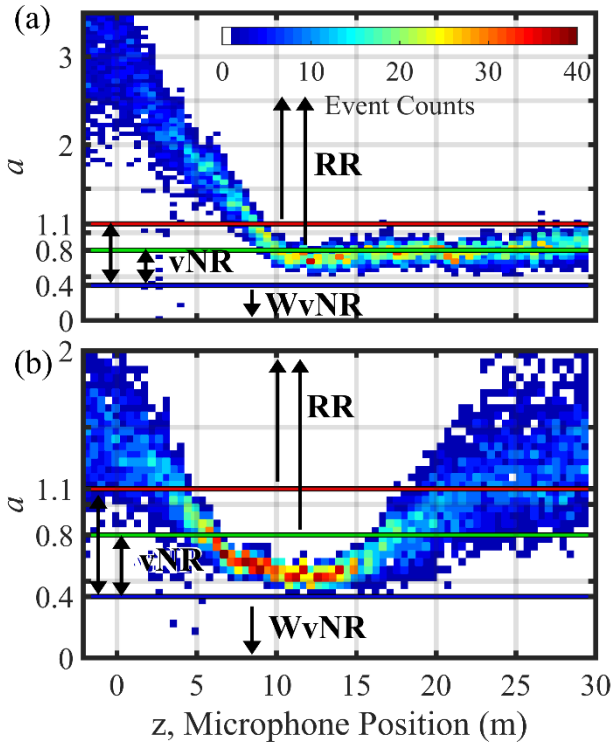

Figure 3.11 Histograms of critical parameter values for (a) 75% and (b) 150% ETR.

While both engine conditions transition into the vNR regime, because of the greater acoustic Mach numbers and lower angles of incidence at the end of the array, the top 100 largest derivative events are more likely classified as vNR for 75% ETR at the end of the array, as shown in Figure 3.11. The distribution of acoustic Mach numbers in Figure 3.8 and angles of incidence distributions in Figure 3.9 directly impacts the histograms of calculated a values and helps explain the different trends in Figure 3.11. For $z > 7$ m, the acoustic Mach numbers are lower for the 75% ETR distribution than 150% ETR in Figure 3.8 and the angle of incidences in Figure 3.9 are less for the 75% ETR distribution than 150% ETR. In the trough region from $z = 7$–15 m, both the angles and acoustic Mach numbers are lower for 75% ETR. For $z < 15$ m, the angle of incidence distribution remains slightly less, whereas the acoustic Mach numbers are slightly greater for 75% ETR. This combination means that there are more of the derivative events are predicted to be vNR

at 75% ETR than at 150% ETR at far downstream locations, which may be a plausible explanation for the elevated derivative skewness values for lower engine conditions at the end of the array.

3.4.3 Engine Condition Comparison

The occurrence of vNR for all four engine conditions of interest are compared in M_a-ϕ space are visualized in Figure 3.12a. The mean is taken for both M_a and ϕ values of the 100 events at each microphone. Using a greater number of events would shift the mean value to the left to a lower acoustic Mach number because events are defined as the largest derivatives, which are expected to have the largest acoustic Mach numbers, while the angle of incidence is anticipated to vary similarly to the current distribution. Even though there are events in Figure 3.8a with $M_a \approx 0.1$ for 150% ETR, the peak mean $M_a \approx 0.06$. Similarly, for 75% ETR, the mean is less than that of the events most likely to be classified in the vNR regime. However, the mean value of the top 100 derivative events transitions into the vNR regime for all engine conditions of interest. The acoustic Mach number drives the transition from RR to vNR (at $\phi > 10°$) as each trend line predominantly crosses the boundary a line from left to right. Including 100% ETR serves as an intermediate case between 75% and 150% ETR, whereas 130% ETR is nearly identical to 150% ETR.

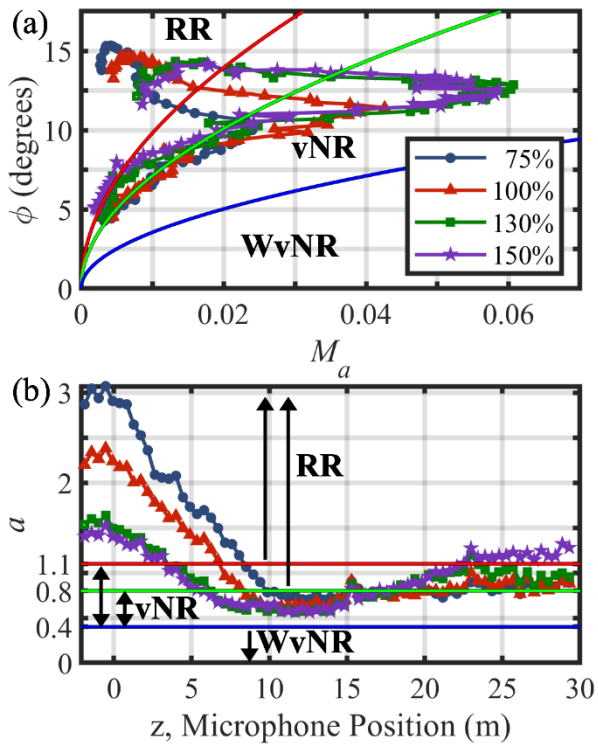

Figure 3.12 Averaged (a) M_a- ϕ space results and (b) critical parameter values for the top 100 derivative events for 75%, 100%, 130%, and 150% ETR.

The mean for the calculated a values versus microphone pair position are shown in Figure 3.12(b), which allows for spatial comparison of a values across engine condition. In the upstream portion of the array, particularly $z > 5$ m, a values are greater for lower engine powers, suggesting that the events undergo RR. The transition from RR to vNR occurs farther upstream for greater engine powers and the locations are reported in Table 3.2. In the trough region from $z = 7$–15 m, the a values remain lower for higher engine powers. However, for $z > 18$ m, lower a values are observed for lower engine conditions. While all engine conditions in the downstream region increase to at least $a = 0.8$, only 150% ETR transitions to $a > 1.1$. Differences at the end of the array are interesting, as the shock strength generally would be assumed to increase with engine condition, resulting in lower a values and irregular reflections. However, the jet noise directionality shifts towards the sideline at higher engine conditions[19] and because the angle is

greater due to an extended source, the resulting ϕ and M_a values are sufficient at the end of the array for events at higher engine conditions to have higher a values and therefore be less likely classified in the vNR regime, even though levels are still greater at the end of the array for 150% ETR.

Table 3.2 Predicted transition locations from RR to vNR along the array for the mean a values of the top 100 derivative events at each engine condition based on the experimental ($a = 1.1$) and theoretical ($a = 0.8$) transitional critical parameter values.

ETR	z (m)
75%	8.4–9.8
100%	6.8–8.3
130%	3.5–6.2
150%	3.5–5.8

3.4.4 Mach Stem Height

With the strong likelihood of vNR occurring in shock-containing jet noise, Mach stem height is now considered for their impact on off-ground measurements. Mach stem height is expected to increase with distance, which corresponds to lower angles of incidence that are the stronger driving factor for a. When a decreases, h_M increases. Desjouy *et al.*[73] developed a relationship between Mach stem height, h_M, and the critical parameter, a. This relationship resulted from a parametric numerical study of over 2000 configurations of varying spark source heights, propagation distances, and incident pressures. The equation is as follows:

$$h_M = h\left(\frac{\xi}{a}\right)^2 \qquad \textbf{Equation (3.5)}$$

where h is the source height and ξ is a constant equal to 0.41 for which a physical meaning was not initially established, though it appears to be associated with the transition from vNR to WvNR at $a = 0.4$. Equation (3.5) is valid for vNR shocks as it predicts $h_M > h$ when in the WvNR regime, at which point there is no longer a Mach stem but a single shock present. The application

of Equation (3.5) to the present study suggests $h_M = 0.28$ m for $a = 1.1$ and $h_M = 0.53$ m for $a = 0.8$. Using the same spark source as the Desjouy *et al.*[73] study, Karzova *et al.*[72] observed Mach stem heights in strong agreement with Equation (3.5); however, the source heights for the two studies ranged from 2–40 mm. This raises the question of whether the differences in source and scaling allow for the application of Equation (3.5) to the present study. Future investigation to determine the height of Mach stems for vNR in jet noise is necessary to understand potential impact of irregular reflections impacting off-ground measurements.

3.5 Results for All Shocks

Section 3.4 established that there are events over a significant portion of the array predicted to be in the vNR regime. The present section now considers all shock events as defined by the $15\sigma_{\partial \mathrm{p}/\partial \mathrm{t}}$ criterion to determine the percentage of shocks expected to undergo vNR and their relationship to increased derivative skewness values. A brief discussion is also provided for the appropriate a value to bound the transition from RR to vNR.

The percentage of shocks along the ground array predicted in the vNR regime according to the experimentally $(0.4 < a < 1.1)$ and theoretically $(0.4 < a < 0.8)$ proposed bounds are given in Figure 3.13. The total shock counts in Figure 3.3b indicated that there are no significant shock counts at $z < 5$ m, percentage of shocks in the vNR regime are only reported for $z > 5$ m in Figure 3.13. While there is a substantial percentage of shocks across the array for the experimentally proposed vNR regime $(0.4 < a < 1.1)$, there is a lower percentage for the theoretical case $(0.4 < a < 0.8)$, as it is more restrictive. For $z < 15$ m, higher engine powers have a larger percentage of shocks that are predicted to be in the vNR regime, with practically identical percentages at afterburner conditions (130% and 150% ETR). However, for $z > 17$ m,

the trend with engine condition flips with lower engine powers having a greater percentage of shocks in the vNR regime. This inverse relationship between engine condition and percent of shocks in the vNR regime is similar to the relationship for engine condition and derivative skewness at the far downstream portion of the array.

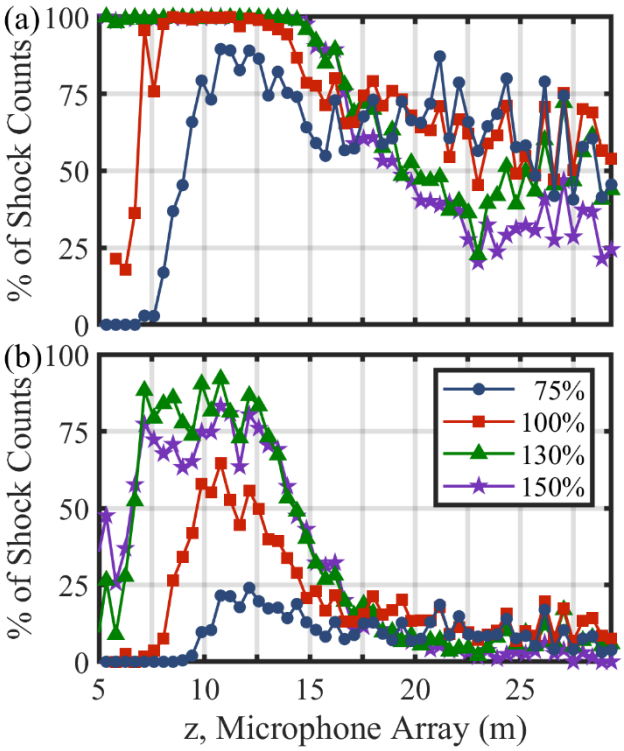

Figure 3.13 Percentage of shocks predicted to be vNR according to the (a) experimentally (0.4 < a < 1.1) and (b) theoretically (0.4 < a < 0.8) proposed bounds.

The occurrence of vNR for a substantial percentage of shocks may help explain the increased Sk{∂p/∂t} values along the ground array relative to off-ground measurements. There is a strong spatial correlation between the shock counts shown in Figure 3.3b and Sk{∂p/∂t} in Figure 2.8a, even at $z > 20$ m where there are greater values at lower engine conditions. Despite the spatial correlation between shock counts and Sk{∂p/∂t}, similar shock counts were observed for the ground and off-ground locations Section 3.3 with drastically different Sk{∂p/∂t}, suggesting that shock counts alone is not sufficient to determine increased Sk{∂p/∂t}. With there being a

notable percentage of shocks in the vNR regime across the entire array, the subsequently increased peak-to-peak pressure and shock steepness are likely to increase derivative skewness compared to off-ground measurements without nonlinear reflections present. Since a larger percentage of shocks are in the vNR regime at lower engine powers for $z > 20$ m, their percentage increase relative to 150% ETR are given in Table 3.3. Not only are there more shock counts at $z > 20$ m for lower engine powers, a larger percentage of those shocks are predicted to be in the vNR regime, especially for the experimental transitional critical parameter bounds.

Table 3.3 Average percentage increase of vNR shocks compared to 150% ETR at $z > 20$ m for the experimental ($0.4 < a < 1.1$) and theoretical ($0.4 < a < 0.8$) transitional critical parameter bounds.

ETR	$0.4 < a < 1.1$	$0.4 < a < 0.8$
75%	29.4%	6.1%
100%	27.5%	8.3%
130%	13.5%	3.9%

The relationship between the percentage of shock counts classified as vNR and Sk{∂p/∂t} values may lend insight into a potentially appropriate critical parameter value representing the transition from RR to vNR. Throughout this study, two critical parameter values ($a = 0.8$ and $a = 1.1$) have been used to predict the transition from RR to vNR. Without a setup to visualize the shocks and confirm the appropriate the shock reflection classification, the a value for the transition from RR to vNR must be determined indirectly. The results of this study suggest that a critical parameter value approaching $a = 1.1$, perhaps at a lower value such as $a = 1.0$, may be appropriate for characterizing the transition from RR to vNR for shocks embedded in jet noise. One piece of supporting evidence for this is that the percent increase in Table 3.3 for $0.4 < a < 1.1$ more closely following the observed Sk{∂p/∂t} trend of increasing with lower engine conditions. Also, with a less restrictive a value there are more shocks undergoing vNR, which

would further help explain the increase of Sk{∂p/∂t} along the ground array. Thus, $a = 1.1$ is recommended until further evidence arises.

3.6 Conclusion

This study has investigated the possibility of nonlinear, irregular shock reflections of the von Neumann type occurring for acoustic shocks in jet noise at ground-based measurements near a tied-down military aircraft. A comparison between a ground and nearby off-ground microphone revealed that while there are similar number of shocks as defined by the $15\sigma_{\partial p/\partial t}$ shock criterion, the resulting Sk{∂p/∂t} values were 1.8 times greater at the ground for 150% ETR. The average maximum derivative of the shocks are $26\sigma_{\partial p/\partial t}$ at the ground compared to only $21\sigma_{\partial p/\partial t}$ off the ground, suggesting that on average, the shocks measured at the ground are steeper. In addition to this, the ratio of peak-to-peak pressures at the ground relative to off the ground is a factor of 2.3, which is greater than a linear doubling and is a characteristic of irregular reflections.

The critical parameter, a, is calculated from the acoustic Mach number and angle of incidence of each shock and used to predict shock reflection classifications. Examining the critical parameter values of top 100 largest-derivative events along the array reveals that vNR are expected primarily at locations where shocks are present as defined by the $15\sigma_{\partial p/\partial t}$ criterion. The position along the array at which shocks transition from RR to vNR based on the experimental ($0.4 < a < 1.1$) and theoretical ($0.4 < a < 0.8$) critical parameter occurs at $z = 3.5$–9.8 m with the transition location occurring farther upstream for greater engine powers. Examination of the critical parameter values of all the shocks along the array defined by the $15\sigma_{\partial p/\partial t}$ criterion indicates that a substantial percentage of shocks are expected to exhibit vNR over the same extent of the array at which Sk{∂p/∂t} values are significant. In addition to increasing the Sk{∂p/∂t} compared to off-

ground measurements along the majority of the ground array, irregular reflections are a plausible explanation for increased Sk{∂p/∂t} at the aft portion of the array where Sk{∂p/∂t} increases with lower engine power. Not only are there more shock counts at these aft locations, a larger percentage of the shocks is expected to experience vNR. A critical parameter value approaching $a = 1.1$ may be appropriate boundary between the RR and vNR regimes for shocks in jet noise. Additional investigation, including visualization of shock reflections in jet noise, is needed to develop quantitative relationships between the occurrence of irregular reflections and the subsequent increase in Sk{∂p/∂t} for ground measurements.

.

Chapter 4
Near to Far-field Correlation of Crackle-related Events

4.1 Introduction

Jet crackle, as a potential factor in community annoyance, depends on the existence of shocks in the far field. Shocks may exist at far-field locations due to nonlinear propagation of large-amplitude waveforms that steepen with distance or the persistence of near-field shocks into the far field. While event-based beamforming of Chapter 2 found apparent near-field origins of crackle-related events and Chapter 3 revealed that there are a significant number of shocks along the near-field ground array using the $15\sigma_{\partial p/\partial t}$ criterion, the objective of the present chapter is to determine the connection between the near-field events and far-field measures correlated with crackle perception. To help determine their relationship, this study employs a nonlinear model to propagate waveforms collected at the near-field ground array into the far field to compare with far-field measurements.

There is some debate as to whether crackle is a propagation or source phenomenon. In the initial crackle study, Ffowcs Williams *et al.*[2] suggested that crackle was a source phenomenon. This claim is supported by the use of the pressure skewness as an indicator for crackle perception, as pressure skewness decays with distance from the source. However, Gee *et al.*[8] has shown that the derivative skewness is strongly correlated to crackle perception while the pressure skewness is not related. Furthermore, Gee *et al.*[80] have shown that large-amplitude waveforms produced near an F-35 nonlinearly propagate, causing waveforms to steepen and form shocks, which

subsequently increases the derivative skewness with distance, until the waveforms and shocks substantially decay.[57] Derivative skewness is a better metric for crackle perception prediction than the pressure skewness, as the pressure skewness decays with distance and does not vary with shock formation, as does the derivative skewness.[13,48]

In order to make comparisons between the near-field crackle-related events and far-field measurements, waveforms need to be propagated using a nonlinear method. Early observations by Morfey and Howell[81] of flyover measurements of the Concorde (the same aircraft studied by Ffowcs Williams *et al*.[2]) and other high-power aircraft suggested a nonlinear model over a linear one to predict jet noise propagation. A linear model generally supposes significant high-frequency attenuation due to atmospheric absorption; however, Morfey and Howell[81] observed greater high-frequency energy than explained by linear models. This irregularity is rectified by a nonlinear energy transfer to high frequencies as explained in a nonlinear model. The nonlinear model used in this study is the generalized Burgers equation (GBE). The GBE is a partial differential equation that accounts for an amplitude-dependent sound speed, which causes waveform steepening: large positive peaks in the waveform to travel faster while large negative pressure peaks (relative to ambient pressure) travel slower. Intermediate engine powers and greater are expected to have sufficient conditions for waveforms to experience significant nonlinear steepening, as has been validated for several aircraft.[10–12] Other uses of this same nonlinear model include a plane-wave tube study[82] and rocket noise. [83]

The primary analysis for comparing near-field crackle-related events to far-field measures is performed using cross-correlation coefficients. A variety of correlation analyses have been used to characterize near-field jet noise sources.[84– 87] However, this study seeks to use correlation as a means to relate the results of the event-based beamforming to far-field measurements. Propagated

waveforms are propagated numerically via the GBE, then cross-correlation coefficients are calculated for individual events, which are the same events identified in the event-based beamforming method from Chapter 2.

Because nonlinear propagation effects are expected to be the greatest, the study contained in this Chapter consists of nonlinearly propagating near-field waveforms to compare with far-field measurements for the F-35 operating at 150% ETR. A brief description of the nonlinear model along with the process for selecting waveforms and events to compare with far-field measurements are provided. Validation of the nonlinear model is made using comparisons between the OASPL, derivative skewness, and spectra for the nonlinear propagated and measured waveforms. An analysis using cross-correlation coefficients of comparable waveform segments is made to quantify the relationship between propagated and measured waveforms, after which a concluding discussion is given.

4.2 Near to Far-field Correlation Methods

First, a description of the nonlinear model using the GBE is provided. Then the process is given for determining what waveform segment to nonlinearly propagate to compare with overall far-field trends. A subset of eight microphones are selected for more direct comparisons between propagated and measured waveforms. Lastly, the method for calculating cross-correlation coefficients is provided.

4.2.1 Nonlinear Model

Selected waveform segments are propagated using a nonlinear propagation model based on the generalized-Burger's equation (GBE) that incorporates cumulative quadratic nonlinearity,

atmospheric absorption and dispersion, and spherical spreading as found in Ref. 11. This formulation of the GBE in a retarded time frame is as follows:

$$\frac{\partial p}{\partial r} = \frac{\beta}{2\rho_0 c_0^3}\frac{\partial p^2}{\partial \tau} + \psi_\tau\{p\} - \frac{1}{r}p \qquad \textbf{Equation (4.1)}$$

where $p(r,\tau)$ is the acoustic pressure, r is the output distance, τ is the retarded time of propagation between the input distance and r, β is the coefficient of nonlinearity, ρ_0 is the ambient air density, c_0 is the ambient speed of sound, and ψ_τ is an operator representing atmospheric absorption and dispersion that acts on $p(r,\tau)$. Equation (4.1) is solved incrementally using a time-frequency domain algorithm that is based on methods in Refs. 88 and 89 described in more detail in Refs. 11, 12, and 90.

4.2.2 Waveform Selection Process

Results from the event-based beamforming in Chapter 2 are used to identify angles at which to propagate near-field measurements into the far field. Initial comparisons between nonlinearly propagated waveforms and far-field measurements are made using all 70 microphone pairs along the ground array. Figure 4.1 shows the outward ray tracings of the propagation angle modes for 150% ETR. These rays are extrapolations of the inward ray tracings shown in Figure 2.9d and discussed in Section 2.4.2. Upstream radiation of group 1 (blue) is of less interest in the near field because of low derivative skewness values but can have appreciable growth in the forward direction.[57] Most outward ray tracings range from 110º–150º. This region is of interest because derivative skewness values are sufficient for crackle perception along the 305 m arc, as established in a previous crackle listening study.[8,9,19] Angles relative to the microphone array reference point (MARP) at which the outward ray tracings intersect with the microphone arcs are used as their position for comparisons of the OASPL and derivative skewness values with the

measured data in Section 4.3.1. Waveforms are numerically propagated at 204.8 kHz, which was the sampling frequency at the near-field array, then downsampled to 96 kHz for comparison with far-field measurements.

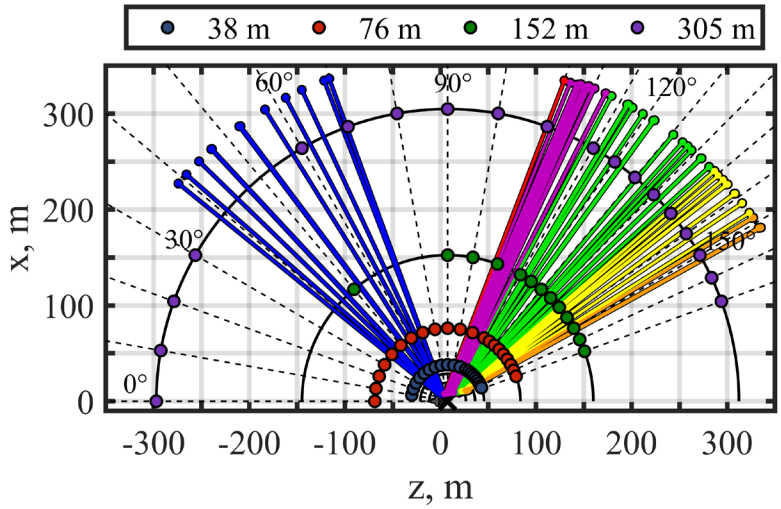

Figure 4.1 Outward ray tracings of the propagation angle mode from the event-based beamforming for 150% ETR (see Figure 2.9d for inward ray tracing).

4.2.2.1 Event Selection

The same 1000 largest derivative events used in the event-based beamforming (see Section 2.2.1) are defined in the 36-s waveforms. For simplicity, a 20.48-s segment is chosen to be nonlinearly propagated and compared with the far-field measurements. On average, the 20.48-s segment contains ~750 large derivative events. An iterative process is used to find a 20.48-s segment with similar OASPL and derivative skewness values to that of the overall waveform. Across the entire array, derivative skewness values for a 5.12-s segment may vary by as much as 10% while the OASPL varies less than 1 dB compared to the 36-s waveform.

4.2.2.2 Microphone Subset Selection

Ideal ground array measurements to compare directly with far-field measurements are those that have events projected to propagate near microphones along far-field arcs. A subset of eight microphones along the ground array are used to compare waveform segments centered about previously beamformed events using cross-correlation coefficients. Information for the locations, associated event-based beamforming group, propagation angles, and intersection angles with radial arcs are given in Table 4.1. Due to the sparseness of far-field arc microphones every 5º or 10º, ground array microphones were chosen with events that have propagation angle modes such that the outward traced rays intersect near locations of far-field microphones. This generally means that the ground array microphones selected fall along a jet inlet angle radial as defined by the MARP and have similar propagation angle to the radial angle. The normalized histogram distributions in Figure 2.5b show that microphone pairs with events that propagate 110º to 150º have a spread of about 10°, which helps justify the use of the mode and splitting the difference of intersection angles across the arcs.

Table 4.1 Radial angles of interest, event-based beamforming group number and color, propagation angle modes, array position jet inlet angle, and the intersection angle with far-field arcs for the subset of eight ground array microphones used in the near to far-field event comparison.

Radial Angle	Group Number (& Color)	Propagation Angle Mode	Array Position Angle	19 m	29 m	38 m	76 m	152 m	305 m
110°	3 (Purple)	113°	104.0°	108.9°	110.2°	110.9°	112.0°	112.5°	112.7°
120°	4 (Green)	118°	127.3°	123.7°	121.8°	120.9°	119.4°	118.7°	118.4°
125°	4 (Green)	124°	131.6°	-	-	126.5°	125.3°	124.6°	124.3°
130°	4 (Green)	130°	138.4°	-	-	133.3°	131.6°	130.8°	130.4°
135°	4 (Green)	134°	140.2°	139.1°	137.6°	136.6°	135.3°	134.6°	134.3°
140°	5 (Yellow)	139°	144.0°	-	-	141.3°	140.2°	139.6°	139.3°
145°	5 (Yellow)	144°	147.1°	-	-	145.6°	144.8°	144.4°	144.2°
150°	6 (Orange)	149°	150.4°	-	-	150.4°	150.7°	150.9°	150.9°

A smaller subset of three of the eight microphones in Table 4.1 are used to examine waveform features in Section 4.3.3. While the outer four arcs (38–305 m) are of primary interest because of their position in the far field, two additional inner arcs at $r = 19$ m and 28 m have microphones at a more limited number of positions. For 110°, 120°, and 135°, microphones exist at both the inner 19 and 29 m arcs, whereas microphones only exist at one or neither location for other angles. This allows for a more incremental comparison between the nonlinearly propagated and measured waveforms in Section 4.3.3 and their corresponding cross-correlation coefficients in Section 4.3.4.

4.2.3 Cross-correlation Coefficients

Near-field, crackle-related events are directly compared to far-field measurements using cross-correlation coefficients. First, to time-align waveforms, a cross-correlation is performed to find a time lag between the 20.48-s propagated waveform segment given in retarded time and the measured waveform at the propagated distance. Similar time-alignment can be found using the measured distances and speed of sound with differences of less than 0.1 ms up to the 76 m arc and within a few milliseconds at the 152 and 305 m arcs. Discrepancies are expected to increase with distance, as the assumed pathlength may differ due to microphone position uncertainty, varying ambient conditions impacting the speed of sound, wind, and the directivity of the beamformed events being different from that of the overall energy in the waveform. After waveforms are temporally aligned, cross-correlation coefficients, ρ_{xy}, are calculated for the entire 20.48-s waveform and each individual event. For each of the 180–200 large-derivative events of interest, the 10-ms waveform segment centered about the event in the propagated and measured waveforms is used to calculate ρ_{xy}. While no windowing or variable segment length based on the characteristic

frequency of the waveform is applied, these could be done to improve results.[84] The ρ_{xy} values are found only using nonlinear propagation on the ground-array waveform, which does not account for meteorological, terrain, or other measurement effects.

4.3 Results and Analyses

Validation and limitations of the nonlinear model are examined by comparing measured and propagated OASPL, derivative skewness, and spectra in Sections 4.3.1 and 4.3.2. Example waveforms are examined in Section 4.3.3 for three radial cases to provide a qualitative comparison of near to far-field crackle-related events. Lastly, cross-correlation coefficients for the propagated and measured shock waveforms segments are compared, providing a quantitative relationship between near and far-field events in Section 4.3.4.

4.3.1 OASPL and Derivative Skewness Comparison

Comparisons between propagated and measured of OASPL and derivative skewness along four arcs are shown in Figure 4.2. Each plot denotes for a given arc array the measured values in black and the values of the propagated waveforms in colors, which represent the color groupings from Section 2.4.1. Groups 3, 4, and 5 (purple, green, and yellow) are related to crackle perception at the near-field ground array, while the others are not, though their derivative skewness values may increase sufficiently for crackle perception in the far field.

The OASPL and derivative skewness have similar trends for both the propagated and measured data. The OASPL and derivative skewness for the propagated waveforms peak at larger angles. This suggests that the directivity of the noise source responsible for the large derivative events for those groups may be fundamentally different than the directivity of the noise

components producing the majority of the time-averaged energy. This region where the levels and derivative skewness are greater correspond primarily to group 5 (yellow), for which there is a slight increase in OASPL in the near field that perhaps does not radiate efficiently into the far field. Despite the disparity between directivities and peak values, the nonlinear propagation produces waveforms similar to the measured values in the far field.

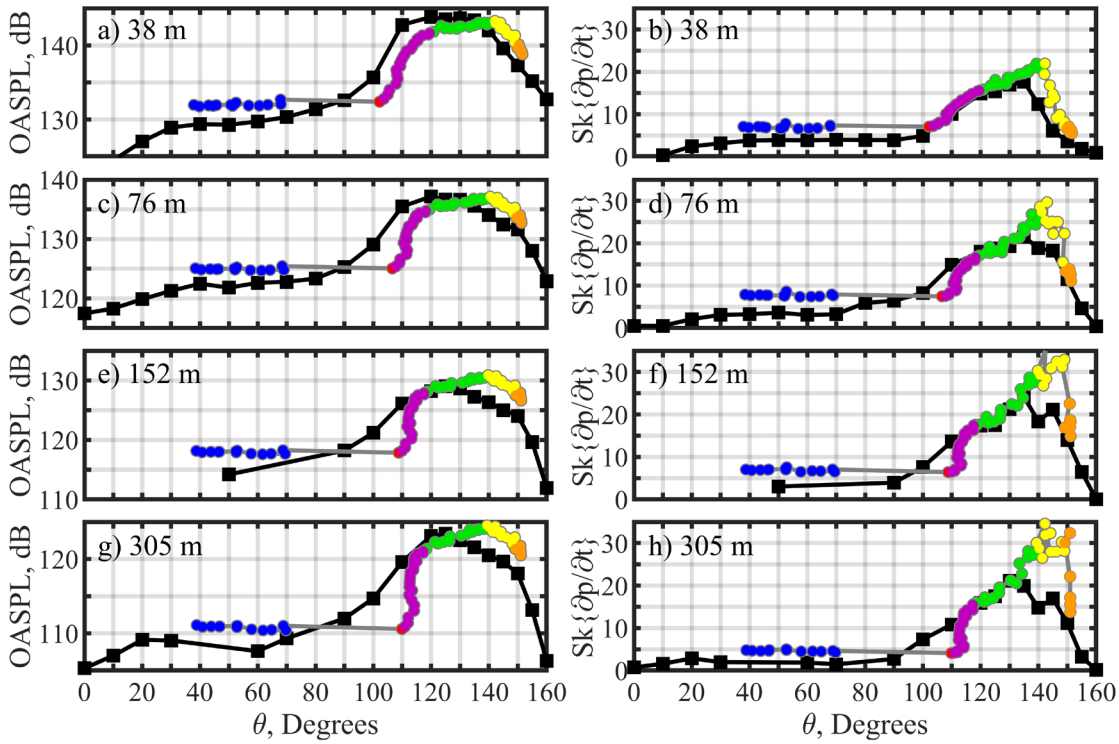

Figure 4.2 Measured and nonlinearly propagated projected OASPL and derivative skewness along the a) b) 38 m, c) d) 76 m, e) f) 152 m, and g) h) 305 m arcs. Colors identify event-based beamforming group, as defined in Section 2.4.1.

The choice of spherical spreading in the nonlinear model appears appropriate as validated by OASPL trends as a function of distance. For select angles from Table 4.1, OASPL and derivative skewness values as a function of distance are shown in Figure 4.3. The spherical decay rate, η, as a function of distance, r, is given as:

$$\eta = 20\log_{10}\left(\frac{1}{r}\right) \qquad \textbf{Equation (4.2)}$$

and is denoted by the blue dashed line in Figure 4.3. There is a 150-dB offset applied to η allow for comparison with measured and propagated levels. Generally, the measured and propagated levels follow the spherical decay rate. The propagated waveforms' OASPL are slightly underpredicted at some locations for 110° and 120° and overpredicted at 140° and 150°. Some reasons for discrepancies in levels could include near-field measurements capturing noise that does not radiate spherically at those distances, different directivity for the beamformed events from the overall average waveform energy, terrain, meteorological, and other measurement effects. Despite the discrepancies due to proposed and other reasons, the resulting OASPL reasonably follow spherical decay.

The derivative skewness in Figure 4.3 reveals limitations in making direct comparisons using the derivative skewness values between the measured and propagated waveforms in the far field. The first derivative skewness point, representing the value measured at the ground array, is consistently greater than the value at the nearest arc measurement, which are located 5′ off the ground. This is likely attributed to the presence of nonlinear reflections occurring at the ground measurements, as discussed in Chapter 3. Despite this discrepancy, the derivative skewness values approach nearly identical values by the 305 m arc for 130° and lower angles. Contrarily, at 140° and 150° the derivative skewness for the propagated waveforms are consistently greater. At 140°, both the propagated and measured waveforms follow a similar spatial derivative skewness trend of increasing then decreasing with distance, despite the discrepancy in values. A similar trend is observed up to the 152 m arc for 150°, but the derivative skewness continues to increase to the 305 m arc for the propagated waveform while the measured value decreases. The greater levels at 140° and 150° suggest that there is a larger potential for large-pressure events at the ground array to

form into shocks with propagation. However, despite physical limitations of the nonlinear model, reasonable results are produced.

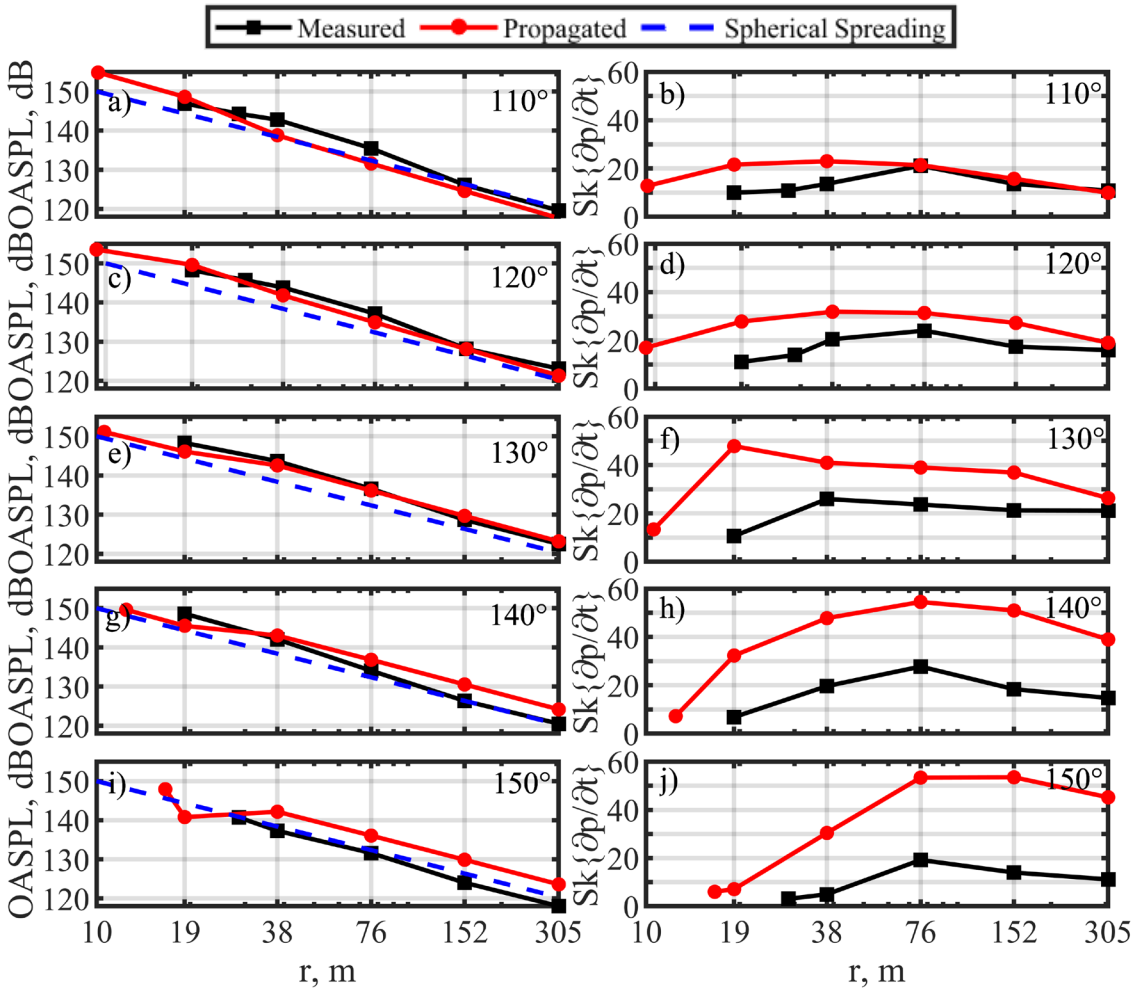

Figure 4.3 Measured and nonlinearly propagated a) OASPL and b) derivative skewness values along the 110° radial, c) OASPL and d) derivative skewness along the 120° radial, e) OASPL and f) derivative skewness along the 130° radial, g) OASPL and h) derivative skewness along the 140° radial, andic) OASPL and j) derivative skewness along the 150° radial. The blue dashed line in the OASPL plots represents spherical decay.

4.3.2 Spectral Comparisons

Spectral comparisons further validate the nonlinear model. Figure 4.4 shows spectral comparisons between the propagated (red) and measured (black) for the same waveforms examined in Figure 4.3 with the propagated angles reported in Table 4.1. Each row represents a

different arc, while columns denotes a radial angle. For nearly all cases, high frequencies (>1 kHz) match well, which validates the use of the nonlinear model. Without the nonlinear model, the high frequencies would decay more rapidly and be underpredicted. Along the 38 m arc, the peak frequency is similar for both the measured and propagated waveform spectra, with 110° underpredicting the level, 150° overpredicting the level, and 120°–140° nearly identical levels. As a function of distance, the peak frequencies are higher for the propagated waveform spectra than the measured spectra in all cases at greater distances, while the levels are underpredicted for 110° and 120° and overpredicted for 140° and 150°. Along the 120° radial, the double peak in the propagated spectra matches well at the nearer two arcs, but the higher frequency peak decreases in level, becoming almost indistinguishable in the measured spectra at 152 m. Overall, despite the discrepancies about the peak, which further informs the differences observed for OASPL, the propagated and measured spectra match well, especially the high-frequency content.

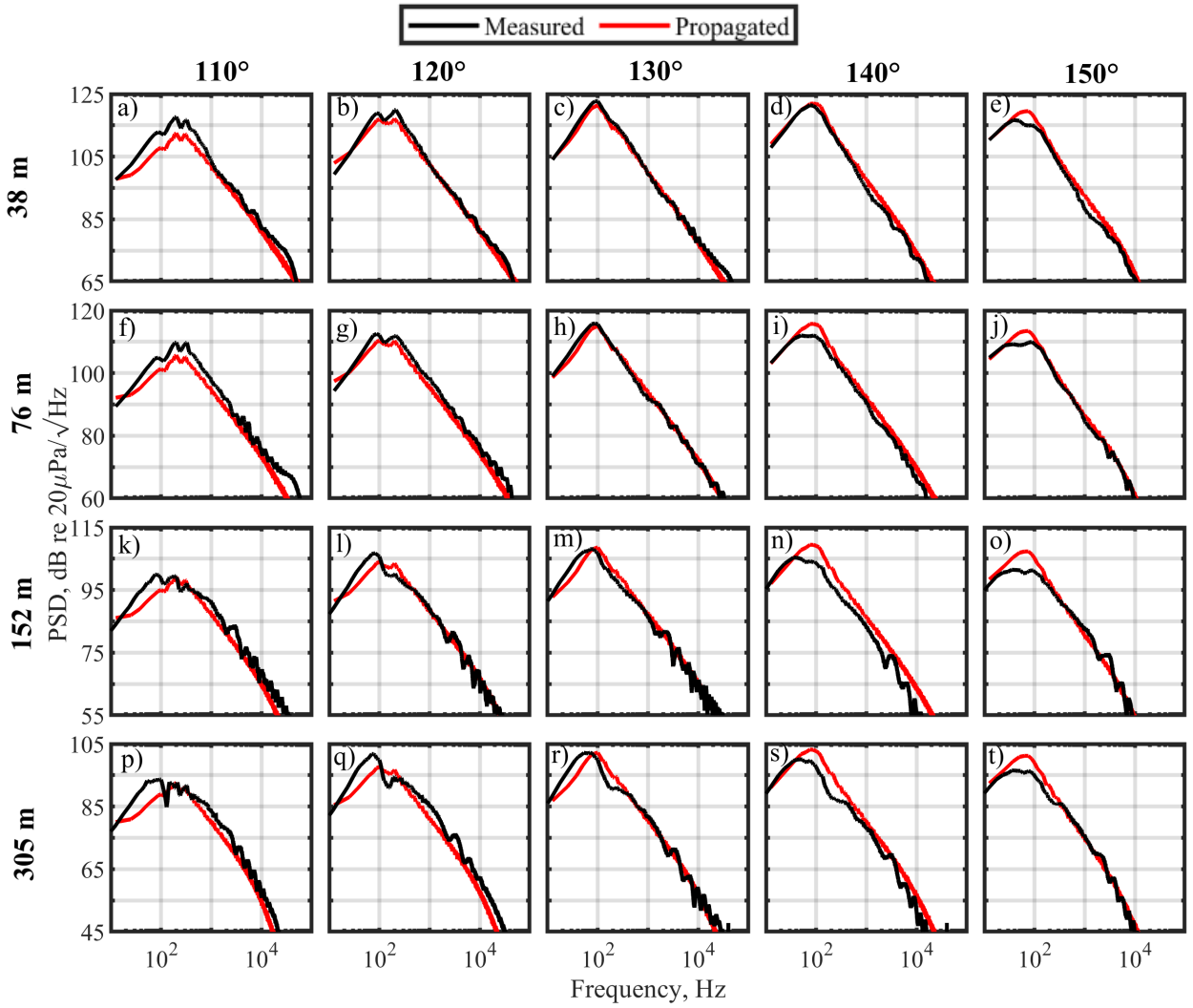

Figure 4.4 Spectra comparison between the measured (black) and nonlinearly propagated (red) waveforms. Columns refer to angles and rows represent radial arcs, as noted.

4.3.3 Waveform Comparison

Example waveforms comparing propagated and measured shocks at six distances along three radials are examined in this section. The radial angles are 110°, 120°, and 135°. Information regarding the propagation waveform angles and their intersection angles with each far-field arc radial are in Table 4.1. Waveform segments of 20-ms length are shown for 19, 29, 38, 76, 152, and 305 m arc radials and compared with the corresponding measurements along the arcs. Each waveform is centered about a large derivative event denoted by a red x in the ground-array

waveform in Figure 4.5a, 4.6a, and 4.7a. Other large-derivative events, that are considered shocks according to the $15\sigma_{\partial p/\partial t}$ shock criterion, may also exist within the 20-ms waveform and are similarly noted by a red x. Cross-correlation coefficients, ρ_{xy}, are calculated and reported for 10-ms segments centered about the main large derivative event at 0 ms (from -5 ms to 5 ms).

As shown in Figure 4.5, some shocks in the 20-ms waveform along the 110° radial (see row 1 in Table 4.1) do not persist to the far-field. The first large-derivative event at -8 ms is more impulsive, with a more abrupt rise and sharp drop after peaking, compared to the second event at 0 ms. As a function of distance, the first event decays rapidly and is nearly unidentifiable beyond the ground array in the measured waveforms, though it persists slightly in the propagated waveforms. Similarly, the narrow-peaked, shock-like event at about -5.5 ms also decays and is not readily identifiable beyond the ground array. There are also a number of small shocks throughout the measured 19 m arc waveform that do not persist into the far field.

There are near-field shock events that do propagate into the far field, as demonstrated by the central event at 0 ms. At the 19 m arc, the measured waveform still has not quite steepened into a single shock. Two factors that likely attribute to the lack of a formed shock at 19 m is that the shock identified in the ground array data (Figure 4.5a) is present in the off-ground data (Figure 4.5b) with a ground reflection and the shock measured at the ground could potentially be overly steepened due to the occurrence of an irregular shock reflection, as discussed in Chapter 3. As a result of the shock being fully formed at the ground, the derivative skewness at the ground is likely elevated and the subsequently propagated waveform decays more rapidly than the measured waveform, as there is increased absorption of energy at the shock peak. The behavior of the propagated versus measured waveforms can also be described by ρ_{xy}. The ρ_{xy} is lower at 19 m than 29 m, likely due to more significant ground interference at 19 m. Beyond 29 m, ρ_{xy} decreases

with distance, partly due to shock being well formed at the ground, which decays more rapidly with distance relative to other waveform segments. At the 305 m arc, even though the propagated waveform does not ideally match the measurement, there is a shock present at 0 ms for the measured waveform, demonstrating that this event identified at the ground array persists into the far field.

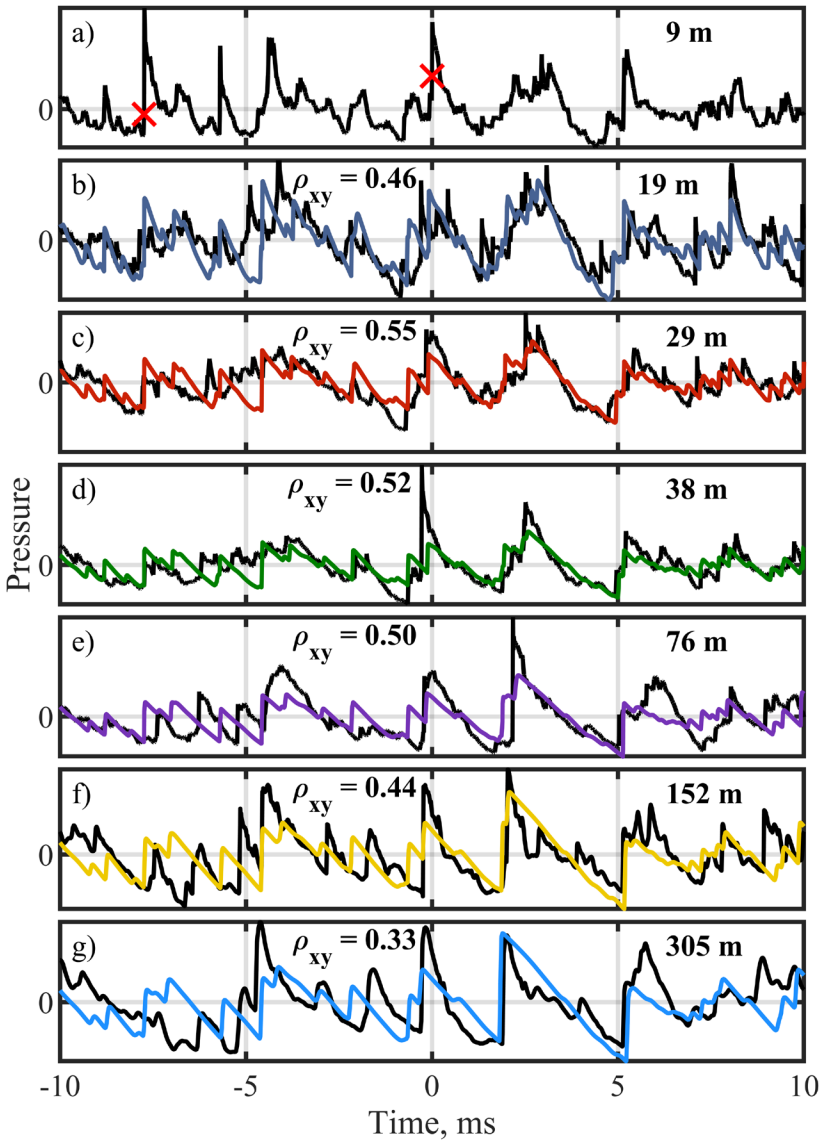

Figure 4.5 Example waveforms along the 110° radial at a) ground array and b) 19 m, c) 29 m, d) 38 m, e) 76 m, f) 152, and g) 305 m arcs. Black lines denote measured waveforms while colors represent the nonlinearly propagated waveforms. Cross-correlation coefficients for the 5-ms to 15-ms segment are also noted.

There are other near-field events that give rise to far-field shocks. Another significant shock exists at about 2 ms in Figure 4.5g for both waveforms at the 305 m arc, though it does not originate as a shock at the ground array. From about 2–4 ms in the ground-array waveform in Figure 4.5a, there is a broad, large pressure waveform segment. This progressively steepens to form a distinct shock by 76 m. From these examples, it is observed that not all large-derivative shock events necessarily propagate into the far field, and large pressure events may also have the potential to form far-field shocks.

The persistence of first and second shocks and decline of the third shock into the far field are observed in the waveform example along the 120° radial in Figure 4.6. The first shock at -5 ms is the narrowest in peak and decays more rapidly than the measured waveforms at each radial distance. The second event occurs at the waveform center (0 ms) and is most similar to the measured waveform along all the arcs. The ground reflection is pronounced at 19 m, which again causes ρ_{xy} to be lower than at 29 m. Similar to Figure 4.5, ρ_{xy} generally decreases with distance, though it increases slightly at the 152 m arc. The third defined event at about 3.5 ms is more similar to the event at -5 ms in Figure 4.5a than the second event, and subsequently the nonlinear propagation scheme causes it to decay and underpredict the peak up to 38 m, then it actually overpredicts at farther arcs. Time misalignment for the first and third events are probably due to the shocks having slightly different propagation angles relative to the assumed mode value, as described in Section 2.3.

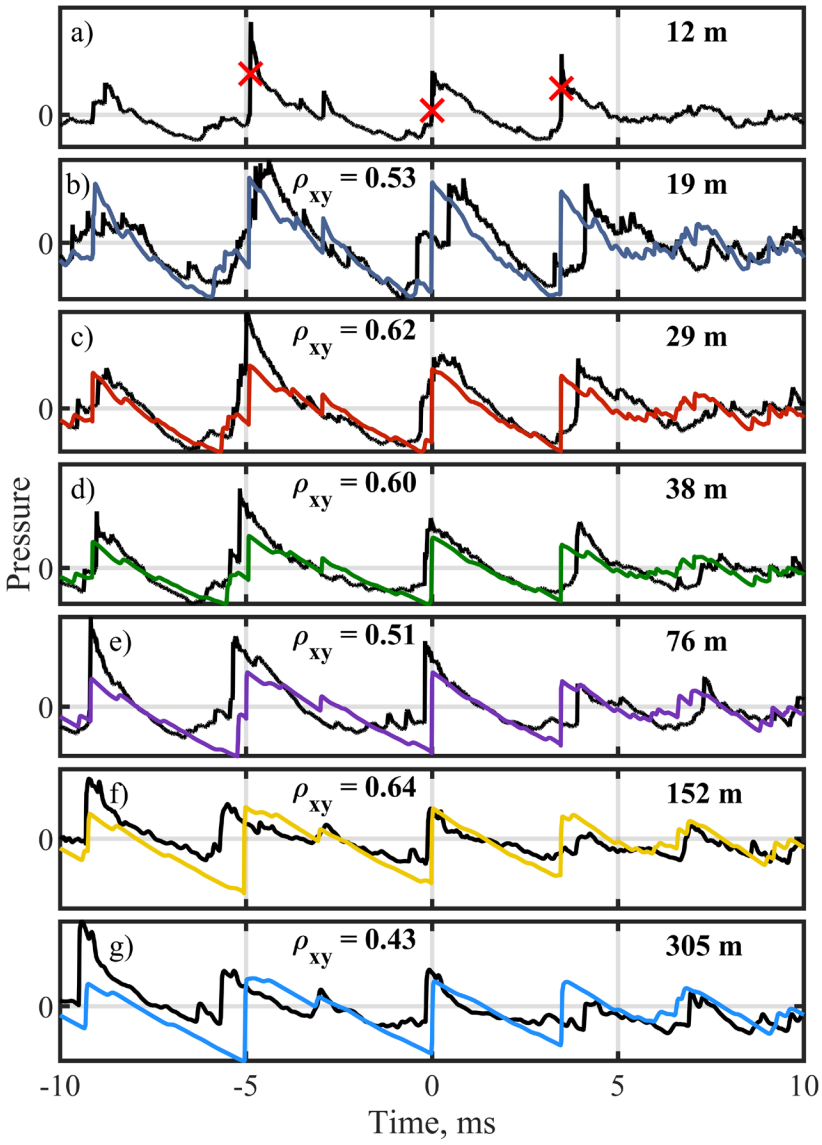

Figure 4.6 Example waveforms along the 120° radial at a) ground array and b) 19 m, c) 29 m, d) 38 m, e) 76 m, f) 152, and g) 305 m arcs. Black lines denote measured waveforms while colors represent the nonlinearly propagated waveforms. Cross-correlation coefficients for the 5-ms to 15-ms segment are also noted.

More distinct and stronger correlated events are observed at farther aft locations. Compared to 110° and 120°, the large derivative event in the waveform propagated along the 135° radial is more isolated, with a single shock forming in the 20-ms waveform shown in Figure 4.7. The ρ_{xy} values are greatest for this of the three radials, with the 10-ms segment focused only on the event of interest. A window or more limited waveform segment based on the characteristic frequency of

the waveform for the 110° and 120° cases may allow for more direct comparison between propagated and measured events using ρ_{xy} values. Despite the slight mismatch about the peak and the underpredicted pressures before the shock, the propagated and measured waveforms appear quite similar up to 38 m and somewhat similar at greater distances.

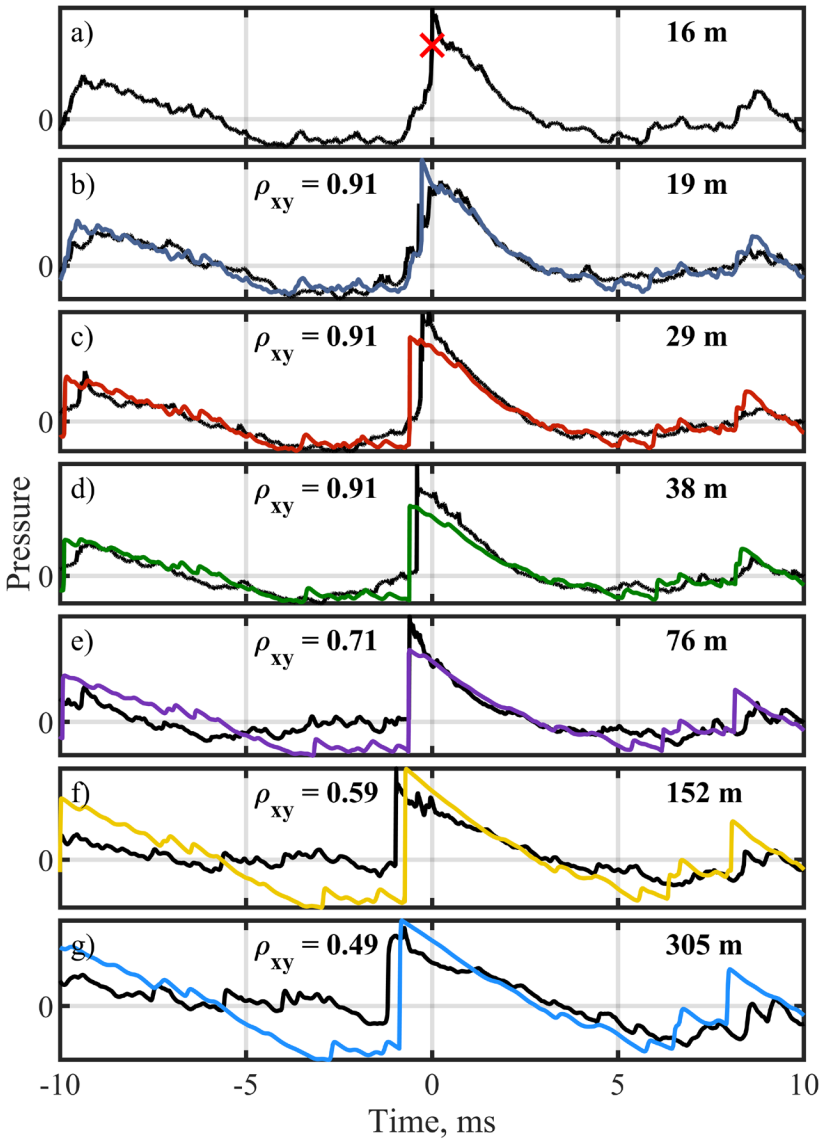

Figure 4.7 Example waveforms along the 135° radial at a) ground array and b) 19 m, c) 29 m, d) 38 m, e) 76 m, f) 152, and g) 305 m arcs. Black lines denote measured waveforms while colors represent the nonlinearly propagated waveforms. Cross-correlation coefficients for the 5-ms to 15-ms segment are also noted.

4.3.4 Cross-correlation Coefficient Histograms

Cross-correlation coefficients, ρ_{xy}, are calculated for segments of propagated and measured waveforms centered about shock events to provide a quantitative relationship of near-field crackle-related events and far-field measurements. The distribution of calculated ρ_{xy} values for the 10-ms waveform segments centered about each of the ~ 750 event are presented as box and whisker plots. Corresponding to the waveforms examined in Section 4.3.3, ρ_{xy} distributions for six distances are first compared for three angles in Figure 4.8. Only the outer four arcs (38, 76, 152, and 305 m) are considered for the ρ_{xy} distributions of eight angles in Figure 4.9. For each distribution, the bottom and top edges of the box indicate the 25^{th} and 75^{th} percentiles, respectively, while the central mark notes the median. The whiskers extend to approximately $\pm$ 2.7 σ and 99.3% coverage assuming the data are normally distributed, with outliers are noted by red pluses. Lastly, comparisons between the ρ_{xy} value of the 20.48-s waveforms and the medians of the ρ_{xy} distributions for the event comparisons are given in Table 4.2, revealing the significance of the ρ_{xy} values of the propagated events in the far field.

Spatially, the ρ_{xy} values are greater at farther aft angles and decreases with increased propagation distance. Distributions of ρ_{xy} values are presented in Figure 4.8 for the six distances at the three angles that waveform examples were previously provided for in Section 4.3.3. Parts a) through c) are respectively for 110°, 120°, and 135° with each box-whisker corresponding to the distribution of ρ_{xy} values for the 750 propagated events compared at a particular arc. Comparing across angles, distribution of ρ_{xy} values increases from 110° to 120° to 135°. With shocks occurring in quicker succession at 110°, they have more of a potential impact on affecting the cross-correlation about the events of interest. A window or a shorter waveform segment at lower

angles may help to focus on just comparing the event itself, as Harker *et al.*[84] suggests temporal normalization to more meaningfully compare correlations at different angles. Similar to previously examined waveforms of individual events, the ρ_{xy} distributions decrease as a function of distance. The ρ_{xy} values are generally greater at the 29 m than 19 m arc, likely due to ground reflections decreasing the correlation between the propagated ground waveform and the off-ground measurement along the 19 m arc. Despite the increase from 19 to 29 m, ρ_{xy} generally decreases with greater propagation distance, as the physical effects not incorporated into the nonlinear propagation model potentially have a greater impact.

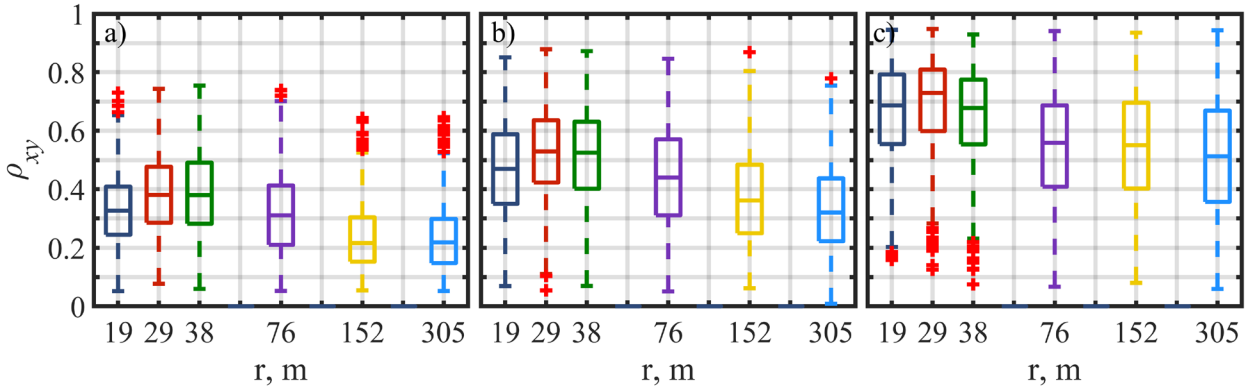

Figure 4.8 Box and whisker plots of cross-correlation coefficients distribution for the 750 propagated events compared with measured waveforms for the 6 arcs (19, 29, 38, 76, 152, and 305 m) along the a) 110°, b) 120°, and c) 135° radials. On each box, lower and upper edges respectively represent the 25th and 75th percentiles with central line indicating the median. The whiskers extend to the most extreme values not considered outliers, while outliers noted as red pluses.

Similar spatial trends are observed for ρ_{xy} values in Figure 4.9. Instead of each subplot corresponding to an angle, they now represent an arc, ranging from 38 to 305 m, and box-whiskers are distributions for a given angle along the arc. A quick visual inspection of Figure 4.8 shows the angular trend of ρ_{xy} values increasing with angle, while Figure 4.9 demonstrates the decrease of ρ_{xy} values increasing with distance. With more angles present in Figure 4.9, an increase in

increasing ρ_{xy} values with angle is observed from 110° to 130°, 130°–150° perform almost equally well.

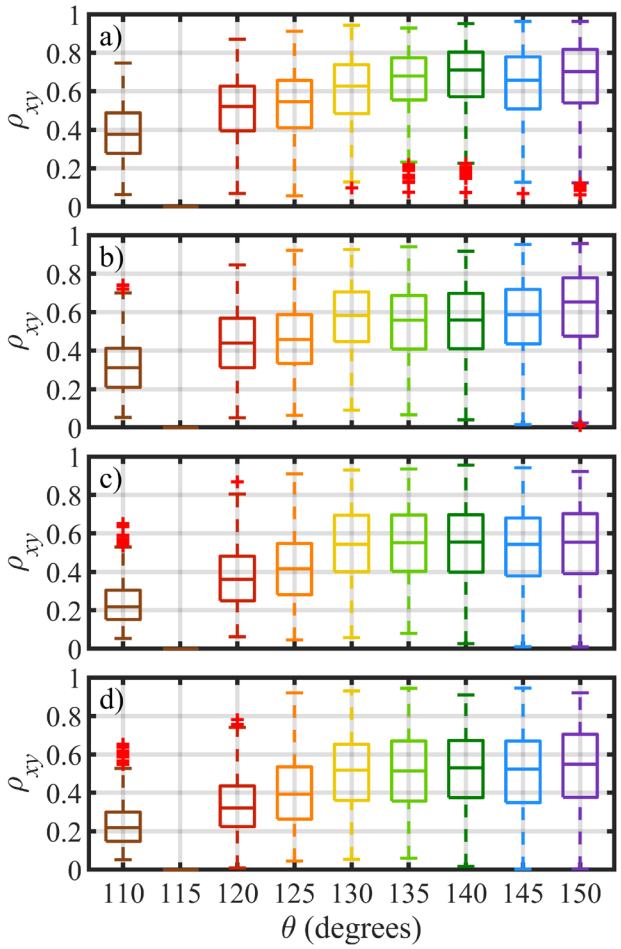

Figure 4.9 Box and whisker plots of cross-correlation coefficients distribution for the 750 propagated events compared with measured waveforms for angles ranging from 110–150° along the a) 38, b) 76, c) 152, and d) 305 m arcs. On each box, lower and upper edges respectively represent the 25th and 75th percentiles with central line indicating the median. The whiskers extend to the most extreme values not considered outliers, while outliers noted as red pluses.

To provide a reference to the significance of the ρ_{xy} distributions of the compared propagated events with far-field measurements, ρ_{xy} values of the entire 20.48-s waveforms and for the median of event comparison distribution are listed in Table 4.2. The ρ_{xy} value for the comparison of the 20.48-s propagated waveform and far-field measured waveform is noted in

Table 4.2 as "waveform" and the median of the ρ_{xy} distribution of the 750 propagated events compared with far-field measurements in 10-ms segments as "events." The ρ_{xy} value is consistently lower for the waveform than the events. Over half of the events for 130°–150° have $0.5 > \rho_{xy}$. These distributions serve to show that there are a significant number of events from the near field that are related to waveform segments in the far field. However, these results do not directly answer how many of these events are directly responsible for crackle perception in the far field. From the waveform examples in Section 4.3.3, shocks measured in the near field may persist into the far field and result in large ρ_{xy} values, while others do not. Regardless, there is a significant correlation between the near-field crackle-related events and measurements in the far field.

Table 4.2 Cross-correlation values for the 20.48 s waveforms and the median for the event distribution shown in Figure 4.9 for the four arcs and eight angles represented in Table 4.1.

Angle	38 m Arc		76 m Arc		152 m Arc		305 m Arc	
	Waveform	Events	Waveform	Events	Waveform	Events	Waveform	Events
110°	0.29	0.36	0.18	0.28	0.05	0.19	0.04	0.19
120°	0.41	0.52	0.31	0.44	0.12	0.39	0.09	0.32
125°	0.48	0.55	0.39	0.48	0.16	0.42	0.15	0.42
130°	0.56	0.64	0.52	0.58	0.23	0.57	0.20	0.53
135°	0.64	0.67	0.47	0.56	0.22	0.55	0.20	0.51
140°	0.68	0.72	0.49	0.58	0.23	0.56	0.21	0.53
145°	0.55	0.68	0.47	0.58	0.20	0.55	0.18	0.52
150°	0.60	0.69	0.55	0.61	0.20	0.55	0.18	0.52

4.4 Conclusion

Near-field, event-based beamforming results have been extrapolated using a nonlinear model based on the GBE and compared to far-field measurements. Some limitations to the nonlinear model are that it does not include reflections, terrain effects, ray tracing due to wind or temperature gradients, and the input not necessarily being in the geometric far field where the spreading is most appropriately represented as spherical. The GBE assumes spherical spreading,

quasi-one-dimensional propagation, quiescent neutral atmosphere, atmospheric absorption and dispersion, and quadratic nonlinearity. Despite these limitations of the nonlinear model, it performs sufficiently well to produce meaningful comparisons of near-field events and far-field measurements. Validation of the nonlinear model include propagated and measured OASPL following a similar trend to spherical decay with distance and propagated and measured spectra matching at high-frequencies with a 20-dB decay per decade as expected for nonlinear propagation. Similar OASPL and derivative skewness values were found for both the propagated and measured data, though the directivity of the propagated OASPL and derivative skewness were slightly aft of the measured, which possibly suggests a difference in source and directivity of the events to the overall waveform energy.

Correlation analysis using cross-correlation coefficients reveals that near-field, crackle-related events are related to far-field measurements. Cross-correlation coefficients, ρ_{xy}, were calculated for the time-aligned propagated and measured waveform segments of 10-ms length centered about each of the 750 events. Spatially, ρ_{xy} values generally decrease with increased distance and are greater for 130°–150° than lower angles. Over half of the events for 130°–150° have $0.5 > \rho_{xy}$. Relative to the ρ_{xy} for the entire propagated 20.48-s waveform, the median of the distribution for the events is greater, suggesting that the events are among the most correlated portions of the waveform. Example waveforms demonstrated that both near-field shock and large-amplitude pressure events give rise to far-field shocks that are likely related to the perception of crackle. These near-field events are not necessarily source phenomena, as nonlinear propagation may play a role in their propagation from the source to near-field measurement location. In addition, these near-field events may include nonlinear reflections. This all suggests that the near-field events examined are likely related to far-field measures through nonlinear propagation.

Further probing towards the source to understand the physical origin of the near-field events is necessary to more thoroughly establish crackle as primarily a propagation rather than a source phenomenon. Future investigation into individual events is warranted in order to more fully determine their relationship to far-field crackle perception.

Chapter 5
Conclusions

5.1 Thesis Summary

This thesis investigates physical jet noise phenomena associated with the perception of crackle. Each chapter explores one of these three main goals: 1) Determine the potential spatial origin of crackle-related events in the near field via an event-based beamforming method. 2) Investigate the potential for nonlinear shock reflections occurring along the near-field ground array and their implications on elevated derivative skewness. 3) Correlate near-field, crackle-related events to potential far-field crackle perception by numerically propagating waveforms to compare with measured far-field data.

The event-based beamforming study in Chapter 2 identifies acoustic source regions along the nozzle lipline of a military aircraft that correspond to higher crackle percept[8,9] in the near field. Short windowed segments of the waveform around 1000 of the highest derivative values are chosen as events in the beamforming process. Six distinct microphone pair groupings have been defined, with particular interest given to those that exceed the criterion for continuous crackle (groups 3–5 (purple, green, and yellow), $\mathrm{Sk}\{\partial p/\partial t\} > 3$). These three crackle-related groups propagate downstream but have differing source locations and directivities. The crackle-related events appear to originate anywhere along the jet nozzle lipline from $z = 2.0$–14.5 m for these groups. Events beamformed from group 3 (purple) display unidirectional radiation and likely originates from the potential core region, consistent with the description of Mach wave radiation.[15,29] Groups 4 and 5 (green and yellow) likely originate downstream of the potential core and appear similar to large-scale turbulent structure noise.

A comparison between a ground and nearby off-ground microphone in Chapter 3 reveals that while there are similar number of shocks as defined by the $15\sigma_{\partial p/\partial t}$ shock criterion, the resulting Sk{∂p/∂t} values were 1.8 times greater at the ground for 150% ETR. The average maximum derivative of the shocks and the ratio of peak-to-peak pressure is greater at the ground, suggesting that on average the shocks at the ground are steeper and increase by a factor of 2.3, which is greater than a linear doubling and is a characteristic of irregular reflections.

Evidence for the occurrence of nonlinear, irregular reflections of the von Neumann type for acoustic shocks in jet noise at ground-based measurements near a tied-down military aircraft is the primary focus of Chapter 3. The critical parameter, a, is calculated from the acoustic Mach number and angle of incidence of each shock and used to predict shock reflection classifications. Examining the critical parameter values of top 100 largest-derivative events along the array reveals that vNR are expected at locations where shocks are present as defined by the $15\sigma_{\partial p/\partial t}$ criterion. The position along the array at which shocks transition from RR to vNR based on the experimental ($0.4 < a < 1.1$) and theoretical ($0.4 < a < 0.8$) critical parameter occurs at $z = 3.5$–9.8 m with the transition location occurring farther upstream for greater engine powers. Examination of the critical parameter values of all the shocks along the array defined by the $15\sigma_{\partial p/\partial t}$ criterion indicates that a substantial percentage of shocks are expected to exhibit vNR over the same extent of the array at which Sk{∂p/∂t} values are significant. In addition to increasing the Sk{∂p/∂t} compared to off-ground measurements along the majority of the ground array, irregular reflections are a plausible explanation for increased Sk{∂p/∂t} at the aft portion of the array where Sk{∂p/∂t} increases with lower engine power. Not only are there more shock counts at these aft locations, a larger percentage of the shocks are expected to experience vNR. A critical parameter value approaching $a = 1.1$ may be an appropriate boundary between the RR and vNR regimes for

shocks in jet noise as occurrence of vNR shocks that likely drive elevated derivative skewness values have more similar spatial trends to the derivative skewness when using an upper bound of $a = 1.1$ instead of $a = 0.8$ to count vNR occurrences.

Chapter 4 takes the near-field, event-based beamforming results from Chapter 2 and extrapolates them via a nonlinear model to determine their relevance in the far field using cross-correlation coefficients. While there are some limitations to the nonlinear model based on the GBE equation, the model performs sufficient to produce meaningful comparisons of near-field events and far-field measurements. The correlation analysis calculates cross-correlation coefficients, ρ_{xy}, for the time-aligned propagated and measured waveform segments of 10-ms length centered about each of the 180–200 events in 5.12 s waveforms. Spatially, ρ_{xy} values generally decrease with increased distance and are greater for 130°–150° than at 110°–125°. Over half of the events for 130°–150° have $\rho_{xy} > 0.5$. Relative to ρ_{xy} for the entire propagated 20.48-s waveform, the median of the distribution for the events is greater, suggesting that the events are among the most correlated portions of the waveform. Example waveforms demonstrated that both near-field shock and large-amplitude pressure events give rise to far-field shocks likely related to the perception of crackle, suggesting that source phenomena explored in Chapter 2 may play a role in tandem with propagation for far-field crackle perception.

5.2 Recommendations for Future Work

A variety of recommendations may be applied to further analyze the F-35B dataset or dataset of other aircraft. The main prerequisite to apply these analyses to other jet aircraft noise measurements is a ground-based array and off-ground measurements, preferably with some co-located. For the event-based beamforming, the methods may be further explored by investigating

the impact of different window types and lengths and using a different time-delay for the adjacent channel instead of just assuming delay due to pathlength difference relative to the MARP. The two-point cross-correlation beamforming method may be expanded upon by extending the beamforming aperture by using more than two microphones. Instead of manually applying criteria to create microphone pair groupings, a data clustering analysis involving more than just propagation angles, OASPL, and derivative skewness may be able to provide more concise groupings with more insightful characteristics. Additional inputs into a cluster analysis may include kurtosis, pressure skewness, average peak-to-peak pressure, average maximum derivative, and shock counts. Application of the event-based beamforming to multiple runups at each engine condition can further validate the results found for the single runups examined in this study.

For the shock reflection study, visualization of shocks would confirm shock reflection classification. Though imaging individual shock events embedded in jet noise may prove difficult in an outdoor environment, the use of closely spaced microphones at ground and off-ground locations may provide sufficient information to better characterize shock reflections.[78] The coalescence of an incident and reflected shock could be examined in the acoustic waveform at each of the heights to determine the occurrence and potential height of Mach stems. Comparing the pressure rise of individual shocks with the nearby off-ground measurements could help further determine the peak-to-peak pressure increase and the impact of irregular shock reflections on derivative skewness values. Comparing derivative skewness to shock counts and relative shock strengths for a group of off-ground microphones to compare with values for ground microphones may provide a more quantitative relationship between ground and off-ground derivative skewness measurements.

The near to far-field correlation study of the crackle-related event in Chapter 4 could be expanded to examine all the engine conditions used in the event-based beamforming study. If multiple runs are used for the event-based beamforming study, they too can be used in the near to far-field correlation study. Also, the entire waveform, including all 1000 events, could be used to provide a larger number of events to compare. Individual inspection of events could further determine whether the near-field shock-like event persists into the far field and whether the cross-correlation coefficient is relatively high or low. Variable segment lengths for performing cross-correlation coefficients at different angles may increase the values at 110° and 120° and allow for more meaningful comparisons across angles. Investigation into the forward direction may lend insight as to whether the upstream radiating group 1 (blue) has any significant crackle content due to propagation. Lastly, an auralization study using the propagated waveforms can further validate the nonlinearly propagation method and provide a comparison of crackle perception due to the propagation relative to the measurements.

Appendix

Cross-correlation coefficients are used to justify the use of a two-point cross-correlation beamforming method in Chapter 1. Averaged cross-correlation coefficient values for 200 events at 150% ETR are shown in Figure A.1, The color at the intersection of the grid lines denote the correlation between the downstream mic number along the array shown on the abscissa and the number of mics upstream ($-z$-direction) or downstream ($+z$-direction) on the ordinate. The first 20 microphones along the array drop off below 0.5 at the adjacent microphone, suggesting that many of these events are not strongly correlated. Farther downstream at greater mic numbers, the correlation is closer to 1 over several microphones. This suggests that the two-point beamforming method is perhaps better for upstream locations, as the correlation of events between adjacent microphones drops off quickly; however, downstream, where there appear to be more events persisting over a greater number of microphones, more than two microphones could be used to improve determining the apparent origin of the crackle-related events.

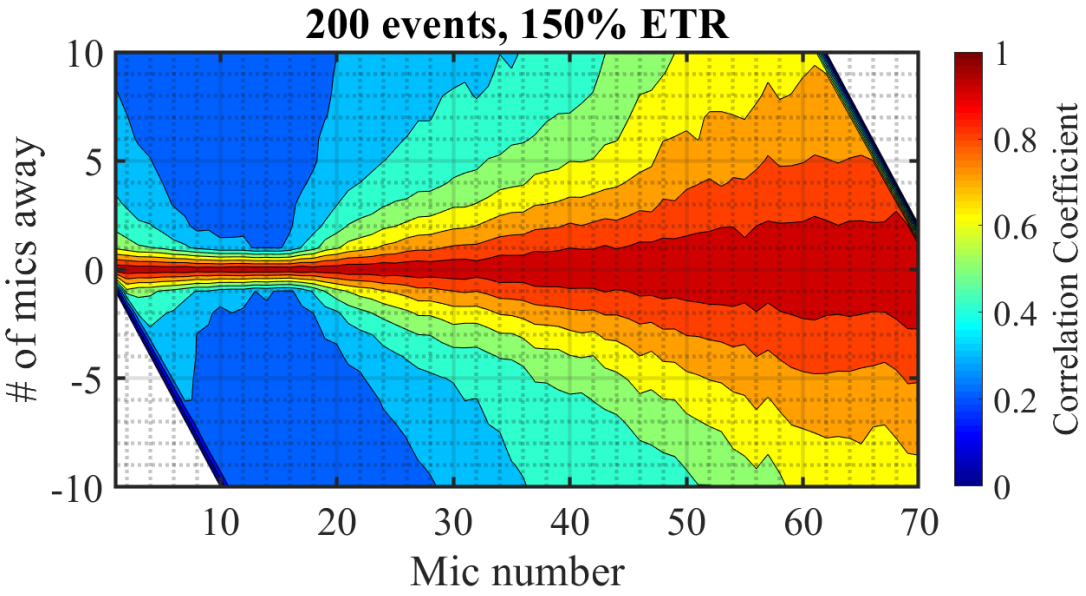

Figure A.1 Correlation coefficients as a function of microphone number for the linear, ground array for 200 events at 150% ETR.

Specific numerical results from the event-based beamforming grouping analysis are noted in Table A.1 and Table A.2. The mean and 5th and 95th percentiles listed in Table A.1 are shown graphically in Figure 2.9 and correspond to the distributions given in Figure 2.10. These values provide a more quantitative comparison between microphone pair groups as well as allow for relative source distribution comparisons to be made with other studies.

Table A.1 Apparent jet lipline origin 5th and 95th percentiles and mean, μ, of compiled grouping histograms across ETR. A dash (–) notes groups that are not applicable for a given engine condition.

Group #	Color	75% ETR			100% ETR			130% ETR			150% ETR		
		5%	μ	95%	5%	μ	95%	5%	μ	95%	5%	μ	95%
1	Blue	2.3	4.0	5.2	2.9	5.1	6.9	3.2	5.7	8.4	3.8	6.3	8.5
2	Red	0.9	3.3	9.1	1.4	4.5	7.6	1.3	4.9	9.1	1.1	5.6	8.8
3	Purple	–	–	–	2.0	4.3	6.0	2.3	5.3	7.3	2.5	7.0	9.7
4	Green	1.9	3.6	5.0	3.3	5.9	7.7	6.5	8.9	11.0	8.3	10.8	12.8
5	Yellow	2.8	5.5	7.9	3.3	6.2	8.6	5.1	8.6	12.2	7.5	11.0	14.6
6	Orange	–	–	–	–	–	–	–	–	–	6.5	9.6	12.8
Total	–	1.7	3.6	6.9	2.6	4.9	7.9	3.5	6.9	11.1	4.1	8.0	13.0

While the values in Table A.2 are not graphically depicted, they provide information regarding the distributions of propagation angles of the microphone pair groups examined in the event-based beamforming study in Chapter 2.

Table A.2 Propagation angle 5th and 95th percentiles and mean, μ, of compiled grouping histograms across ETR. A dash (–) notes groups that are not applicable for a given engine condition.

Group #	Color	75% ETR			100% ETR			130% ETR			150% ETR		
		5%	μ	95%	5%	μ	95%	5%	μ	95%	5%	μ	95%
1	Blue	49.2	71.6	123.0	47.5	70.9	133.1	43.1	68.7	139.2	40.7	68.1	143.7
2	Red	86.5	112.0	126.3	78.9	106.8	122.4	70.6	103.6	125.5	66.4	103.5	146.0
3	Purple	–	–	–	118.9	124.4	131.3	110.4	115.6	122.0	108.8	114.4	122.2
4	Green	127.0	141.0	152.4	128.2	141.0	152.0	116.7	130.7	145.4	118.0	129.4	141.5
5	Yellow	150.6	153.3	156.9	149.0	152.5	156.3	140.5	149.1	155.3	132.7	142.9	150.8
6	Orange	–	–	–	–	–	–	–	–	–	145.9	150.1	154.2
Total	–	70.5	127.4	155.5	63.7	122.5	155.1	61.1	117.1	153.8	57.9	113.7	151.8

The microphone cutoff frequency is more limiting than the sampling rate used for the outer two arcs at 152 and 305 m. Data were collected by two organizations at the outer two arc locations: Wyle and the Air Force Research Laboratory (AFRL). Microphones used by Wyle sampled at 96 kHz while AFRL sampled at 192 kHz. Figure A.2 gives the average derivative skewness values across 5–6 measurements at each location with error bars denoting the standard deviation. Generally, higher sampling frequency is preferred for measuring derivative skewness values, however, the microphone bandwidth proves to be the more limiting factor. As described in Section 1.3, Wyle used 1/4" microphones when possible in the maximum radiation region, while AFRL only used 1/2". The cutoff frequency for the 1/4" microphone is about 70 kHz, while the 1/2" microphone is only about 20 kHz. Despite the higher sampling rate, the 1/2" microphones used by AFRL generally have lower derivative skewness values than the 1/4" microphones used by Wyle. Further investigation into the impact of sampling rate on derivative skewness values is of importance for using it to quantify crackle perception.

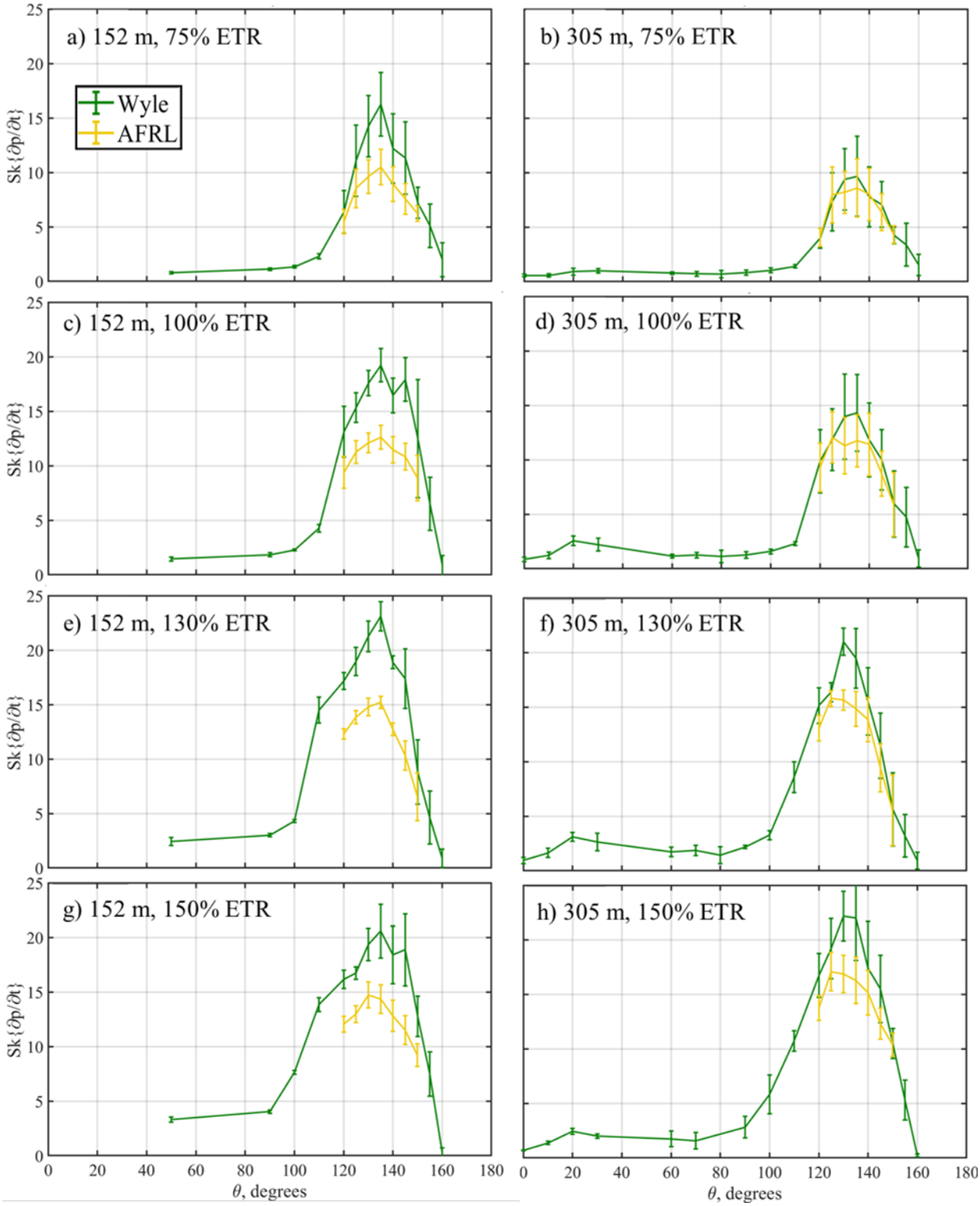

Figure A.2 Comparison of derivative skewness values for ½" microphones sampling at 96 kHz and ¼" microphones sampling at 192 kHz along at the 152 m arc for a) 75%, c) 100%, e) 130%, and 150% ETR and at the 305 m arc for b) 75%, d) 100%, f) 130%, and h) 150% ETR.

References

[1] K. L. Gee, T. B. Neilsen, A. T. Wall, J. M. Downing, and M. M. James, "The 'sound of freedom': characterizing jet noise from high-performance military aircraft," *Acoustics Today*, Vol. 9, No. 3, pp. 8–21 (2013).

[2] J. E. Ffowcs Williams, J. Simson, and V. J. Virchis, " 'Crackle': An annoying component of jet noise," *Journal of Fluid Mechanics*, Vol. 71, No. 2, pp. 251–271 (1975). https://doi.org/10.1017/S0022112075002558

[3] A. Krothapalli, L. Venkatakrishnan, and L. Lourenco, "Crackle: A dominant component of supersonic jet mixing noise," AIAA Paper 2000-2024, June 2000. https://doi.org/10.2514/6.2000-2024

[4] K. L. Gee, R. J. Kenny, T. B. Neilsen, T. W. Jerome, C. M. Hobbs and M. M. James, "Spectral and statistical analysis of noise from reusable solid rocket motors", *Proceedings of Meetings on Acoustics*., Vol. 18, No. 1, p. 040002 (2013). https://doi.org/10.1121/1.4789401

[5] S. A. McInerny, "Launch vehicle acoustics part 2: Statistics of the time domain data", *Journal of Aircraft*, Vol. 33, No. 3, pp. 518–523 (1996). https://doi.org/10.2514/3.46975

[6] D. Fee, R. S. Matoza, K. L. Gee, T. B. Neilsen and D. E. Ogden, "Infrasonic crackle and supersonic jet noise from the eruption of Nabro Volcano", *Geophysical Research Letters*, Vol. 40, No. 16, pp. 2780–2785 (2013). https://doi.org/10.1002/grl.50827

[7] K. L. Gee, T. B. Neilsen, A. A. Atchley, "Skewness and shock formation in laboratory-scale supersonic jet data," *Journal of the Acoustical Society of America*, Vol. 133, No. 6, EL491-EL497 (2013). https://doi.org/10.1121/1.4807307

[8] K. L. Gee, P. B. Russavage, T. B. Neilsen, S. H. Swift, and A. B. Vaughn, "Subjective rating of the jet noise crackle percept," *Journal of the Acoustical Society of America*, Vol. 144, No. 1, EL40–EL44 (2018). https://doi.org/10.1121/1.5046094

[9] P. B. Russavage, T. B. Neilsen, K. L. Gee, K.L. and S. H. Swift, "Rating the perception of jet noise crackle." *Proceedings of Meetings on Acoustics*, Vol. 33, No. 1, p. 040001 (2018). https://doi.org/10.1121/2.0000821

[10] K. L. Gee, T. B. Gabrielson, A. A. Atchley, and V. W. Sparrow, "Preliminary analysis of nonlinearity in military jet aircraft noise propagation," *AIAA Journal*, Vol. 43, No. 6, pp. 1398–1401 (2005). https://doi.org/10.2514/1.10155

[11] K. L. Gee, V. W. Sparrow, M. M. James, J. M. Downing, C. M. Hobs, T. B. Gabrielson, and A. A. Atchley, "The role of nonlinear effects in the propagation of noise from high power aircraft," *Journal of the Acoustical Society of America*, Vol. 123, No. 6, pp. 4082–4093 (2008). https://doi.org/10.1121/1.2903871

[12] K. L. Gee, J. M. Downing, M. M. James, R. C. McKinley, R. L. McKinley, T. B. Neilsen, and A. T. Wall, "Nonlinear evolution of noise from a military aircraft during ground run-up," AIAA Paper 2012-2258, June 2012. https://doi.org/10:2514/6.2012-2258

[13] K. L. Gee, T. B. Neilsen, M. B. Muhlestein, A. T. Wall, J. M. Downing, M. M. James, and R. L. McKinley, "On the evolution of crackle in jet noise from high-performance engines," AIAA Paper 2013-2190, June 2013. https://doi.org/10:2514/6.2013-2190

[14] C. K. W. Tam, J. T. Spyropoulos, A. C. Aubert, and R. W. Powers, "Crackle in the noise of high-performance aircraft," AIAA Paper 2018-3306, June 2018. https://doi.org/10.2514/6.2018-3306

[15] W. J. Baars, C. E. Tinney, M. S. Wochner, and M. F. Hamilton, "On cumulative nonlinear acoustic waveform distortions from high-speed jets," *Journal of Fluid Mechanics*, Vol. 749, pp. 331–366 (2014). https://doi.org/10.1017/jfm.2014.228

[16] P. Mora, N. Heeb, J. Kastner, E. J. Gutmark, and K. Kailasanath, "Effect of heat on the pressure skewness and kurtosis in supersonic jets," *AIAA Journal*, Vol. 52, No. 4, pp 777–787 (2014). https://doi.org/10.2514/1.J052612

[17] S. Chen, R. Gojon, and M. Mihaescu, "High-temperature effects on aerodynamic and acoustics characteristics of a rectangular supersonic jet" AIAA Paper 2018-3033, June 2018. https://doi.org/10.2514/6.2018-3303

[18] M. B. Muhlestein, "Analyses of nonlinearity measures in high-amplitude sound propagation," Ph.D. dissertation, Brigham Young University, Provo, UT (2013). https://scholarsarchive.byu.edu/etd/3994 (see Figure 6.9 for $\mathrm{Sk}\{\partial p/\partial t\} = 4$ at 48 kHz and p. 137 that peak $\mathrm{Sk}\{\partial p/\partial t\} = 2.7$ in the NAH plane.)

[19] M. M. James, A. R. Salton, J. M. Donwing, K. L. Gee, T. B. Neilsen, B. O. Reichman, R. L. McKinley, A. T. Wall, and H. L. Gallagher, "Acoustic emissions from F-35 aircraft during ground run-up," AIAA Paper 2015-2375, June 2015. https://doi.org/10.2514/6.2015-2375

[20] A. T. Wall, K. M. Leete, K. L. Gee, T. B. Neilsen, M. M. James, and R. L. McKinley, "Preliminary investigation of multilobe fighter jet noise sources using acoustical holography," AIAA Paper 2017-3520, June 2017. https://doi.org/10.2514/6.2017-3520

[21] S. H. Swift, K. L. Gee, T. B. Neilsen, A. T. Wall, J. M. Downing, and M. M. James, "Spatiotemporal correlation analysis of jet noise from a round-nozzle supersonic aircraft," AIAA Paper 2018-3938, June 2018. https://doi.org/10.2514/6.2018-3938

[22] T. B. Neilsen, A. B. Vaughn, K. L. Gee, S. H. Swift, A. T. Wall, J. M. Downing, and M. M. James, "Three-way spectral decompositions of high-performance military aircraft noise," *AIAA Journal* Vol. 57, No. 8, pp. 3467–3479 (2019). https://doi.org/10.2514/1J057992

[23] K. M. Leete, A. T. Wall, K. L. Gee, T. B. Neilsen, M. M. James, and J. M. Downing, "Dependence of high-performance military aircraft noise on frequency and engine power," AIAA Paper 2018-2826, June 2018. https://doi.org/10.2514/6.2018-2826

[24] A. B. Vaughn, K. L. Gee, S. H. Swift. A. T. Wall, J. M. Downing, and M. M. James, "Beamforming of supersonic jet noise for crackle-related events," *Proceedings of Meetings on Acoustics*, Vol. 35, No. 1, p. 040003 (2018). https://doi.org/10.1121/2.0000998

[25] S. A. McInerny, J. M. Downing, C. Hobbs, M. M. James, and M. Hannon, "Metrics that characterize nonlinearity in jet noise," *AIP Conference Proceedings*, Vol. 838, No. 1, pp. 560–563 (2006). https://doi.org/10.1063/1.2210418

[26] R. Fievet, C. E. Tinney, W. J. Baars, and M. F. Hamilton, "Coalescence in the sound field of a laboratory-scale supersonic jet," *AIAA Journal*, Vol. 54, No. 1, pp. 254–265 (2016). https://doi.org/10.2514/1.J05452

[27] P. Pineau and C. Bogey, "Steepened Mach waves near supersonic jets: study of azimuthal structure and generation process using conditional averages," *Journal of Fluid Mechanics*, Vol. 880, pp.594–619 (2019). https://doi.org/10.1017/jfm.2019.729

[28] J. Veltin, B. J. Day, and D. K. McLaughlin, "Correlation of flowfield and acoustic field measurements in high-speed jets," *AIAA Journal*, Vol. 49, No. 1, pp. 150–163 (2011). https://doi.org/10.2514/1.J050583

[29] N. E. Murray and G. W. Lyons, "On the convection velocity of source events related to supersonic jet crackle," *Journal of Fluid Mechanics*, Vol. 793, pp. 477–503 (2016). https://doi.org/10.1017/jfm.2016.127

[30] N. E. Murray and W. J. Baars, "Passive nozzle-based technology for reduction of heated supersonic jet noise," AIAA Paper 2019-2729, May 2019. https://doi.org/10.2514/6.2019-2729

[31] K. Daniel, D. Mayo Jr., K. T. Lowe, and W. F. Ng, "Experimental investigation of the pressure field of a heated supersonic jet with a centered total temperature non-uniformity," AIAA Paper, 2018-3145, June 2018. https://doi.org/10.25/6.2018-3145

[32] S. Martens, J. T. Spyropoulos, and Z. Nagel, "The effect of chevrons on crackle—Engine and scale model results," in ASME Turbo Expo 2011, Vol. 54617, pp. 315–326 (2011). https://doi.org/10.1115/GT2011-46417

[33] D. Papamoschou and M. Debiasi, "Directional suppression of noise from a high-speed jet," *AIAA Journal*, Vol. 39, No. 3, pp. 380–387 (2001). https://doi.org/10.2514/2.1345

[34] S. Chen, and M. Mihaescu, "Nozzle pressure ratio effects on aerodynamics and acoustics of a highly-heated rectangular supersonic jet," AIAA Paper 2019-2753, May 2019. https://doi.org/10.2514/6.2019-2753

[35] D. A. Buchta, A. T. Anderson, and J. B. Freund, "Near-field shocks radiated by high-speed free-shear flow turbulence," AIAA Paper 2014-3201, June 2014. https://doi.org/10.2514/6.2014-3201

[36] A. T. Anderson and J. B. Freund, "Source mechanisms of jet crackle," AIAA Paper 2012-2251, June 2012. https://doi.org/10.2514/6.2012-2251

[37] P. Pineau and C. Bogey, C., "Temperature effects on convection speed and steepened waves of temporally developing supersonic jets," *AIAA Journal*, Vol. 58, No. 3, 2019, pp. 1227–1239 (2019). https://doi.org/10.2514/1.J058589

[38] J. W. Nichols, S. K. Lele, F. E. Ham, S. Martens, and J. T. Spyropoulos, "Crackle noise in heated supersonic jets," *Journal of Engineering for Gas Turbines and Power*, Vol. 135, No. 5, p. 051202 (2013). https://doi.org/10.1115/1.4007867

[39] J. W. Nichols S. K. Lele, and J. T. Spyropoulos, "The source of crackle noise in heated supersonic jets," AIAA Paper 2013-2197, June 2013. https://doi.org/10.2514/6.2013-2197

[40] A. Langenais, F. Vuillot, J. Troyes, and C. Bailly, "Accurate simulation of the noise generated by a hot supersonic jet including the turbulence tripping and nonlinear acoustic propagation," *Physics of Fluids*, Vol. 31, No. 1, p. 01605 (2019). https://doi.org/10.1063/1.5050905

[41] J. Laufer, R. H. Schlinker, and R. E. Kaplan, "Experiments on supersonic jet noise," *AIAA Journal* Vol. 14, No. 4, pp. 489–497 (1976). https://doi.org/10.2514/3.61388

[42] R. H. Schlinker, J. C. Simonich, R. A. Reba, T. Colonius, F. Ladeinde, "Decomposition of high speed jet noise: source characteristics and propagation effects," AIAA Paper 2008-2890, May 2008. https://doi.org/10.2514/6.2008-2890

[43] J. I. Hileman and M. Samimy, "Mach number effects on jet noise sources and radiation to shallow angles," *AIAA Journal* Vol. 44, No. 8, pp. 1915–1918 (2006). https://doi.org/10.2514/1.19959

[44] J. I. Hileman, B. Thurow, and M. Samimy, "Development and evaluation of a 3-D microphone array locate individual acoustic sources in a high-speed jet," *Journal of Sound and Vibration*, Vol. 276, No. 3-5, pp. 649–669 (2004). https://doi.org/10.1016/j.jsv.2003.08.022

[45] K. L. Gee, V. W. Sparrow, A. A. Atchley, and T. B. Gabrielson, "On the perception of crackle in high-amplitude jet noise," *AIAA Journal*, Vol. 45, No. 3, pp. 593–58 (2007). https://doi.org/10.2514/1.26484

[46] S. H. Swift, K. L. Gee, and T. B. Neilsen, "Testing two crackle criteria using modified jet noise waveforms," *Journal of the Acoustical Society of America*, Vol. 141, No. 6, pp. EL549–EL554 (2017). https://doi.org/10.1121/1.4984819

[47] R. H. Schlinker, S. A. Liljenberg, D. R. Polak, K. A. Post, C. T. Chipman, and A. M. Stern, "Supersonic jet noise source characteristics & propagation: Engine and model scale," AIAA Paper 2007-3623, June 2007. https://doi.org/10.2514/6.2007-3623

[48] K. L. Gee, T. B. Neilsen, A. T. Wall, J. M. Downing, M. M. James, and R. L. McKinley, "Propagation of crackle-containing jet noise from high-performance engines," *Noise Control Engineering Journal*, Vol. 64, No. 1, pp. 1–12 (2016). https://doi.org/10.3397/1/376354

[49] M. M. Karzova, T. Lechat, S. Ollivier, D. Dragna, P. V. Yuldashev, V. A. Khokhlova, and P. Blanc-Benon, "Effect of surface roughness on nonlinear reflection of weak shock waves," *Journal of the Acoustical Society of America*, Vol. 146, No. 5, pp. EL438–EL443 (2019). https://doi.org/10.1121/1.5133737

[50] R. Marchiano, F. Coulouvrat, S. Baskar, and J. L. Thomas, "Experimental evidence of deviation from mirror reflection for acoustical shock waves," *Physical Review E*, Vol. 76, No. 5, p. 056602 (2007). https://doi.org/10.1103/PhysRevE.760566602

[51] T. A. Stout, K. L. Gee, T. B. Neilsen, A. T. Wall, and M. M. James, "Source characterization of full-scale jet noise using acoustic intensity," *Noise Control Engineering Journal*, Vol. 63, No. 6, pp. 522–536 (2015). https://doi.org/10.3397/1/376346

[52] H. T. Nagamatsu and G. Horvay, "Supersonic jet noise," AIAA Paper 1970-237, January 1970. https://doi.org/10.2514/6.1970-237

[53] C. K. W. Tam, K. Viswanathan, K. K. Ahuja, and J. Panda, "The sources of jet noise: experimental evidence," *Journal of Fluid Mechanics*, Vol. 615, pp. 254–292 (2008). https://doi.org/10.1017/S0022112008003704

[54] C. K. W. Tam and L. Auriault, "Jet mixing noise from fine-scale turbulence," *AIAA Journal* Vol. 37, No. 2, pp. 145–153 (1999). https://doi.org/10.2514/2.691

[55] K. M. Leete, K. L. Gee, J. Liu, and A. T. Wall, "Coherences analysis of the noise from a simulated highly-heated laboratory-scale jet," *AIAA Journal*, pp. 1 – 10 (2020). https://doi.org/10.2514/1.J059112

[56] O. T. Schmidt and P. J. Schmid, "A conditional space-time POD formalism for intermittent and rare events: example of acoustic bursts in turbulent jets," *Journal of Fluid Mechanics*, Vol. 867, (2019). https://doi.org/10.1017/jfm.2019.200

[57] B. O. Reichman, K. L. Gee, T. B. Neilsen, and S. H. Swift, "Acoustic shock formation in noise propagation during ground run-up operations of military aircraft," AIAA Paper 2017-4043, June 2017. https://doi.org/10.2514/6.2017-4043

[58] S. A. McInerny, K. L. Gee, J. M. Downing, and M. M. James, "Acoustical nonlinearities in aircraft flyover data," AIAA Paper 2007-3654, May 2007. https://doi.org/10.2514/6.2007-3654

[59] D. K. McLaughlin, C. W. Kuo, and D. Papamoschou, "Experiments on the effect of ground reflections on supersonic jet noise," AIAA Paper 2008-22, January 2008. https://doi.org/10.2514/6.2008-22

[60] K. L. Gee, T. B. Neilsen, and M. M. James, "Including source correlation and atmospheric turbulence in a ground reflection model for rocket noise," *Proceedings of Meetings on Acoustics*, Vol. 22, No. 1, p. 040001 (2014). https://10.1121/2.0000002

[61] S. A. E. Miller, "The prediction of jet noise ground effects using an acoustic analogy and a tailored Green's function," *Journal of Sound and Vibration*, Vol. 333, No. 4, pp. 1193–1207 (2014). https://doi.org/10.1016/j.jsv.2013.10.028

[62] K. M. Leete, A. T. Wall, K. L. Gee, T. B. Neilsen, M. M. James, and J. M. Downing, "Dependence of high-performance military aircraft jet noise on frequency and engine power," AIAA Paper 2018-2826, June 2018. https://doi.org/10.2514/6.2018-2826

[63] B. M. Harker, K. L. Gee, T. B. Neilsen, A. T. Wall, and M. M. James, "Source characterization of full-scale tactical jet noise from phased-array measurements," *Journal of the Acoustical Society of America*, Vol. 146, No. 1, pp. 665–680 (2019). https://doi.org/10.1121/1.5118239

[64] E. Mach, " Uber den Verlauf von Funkenwellen in der Ebene und im Raume" ("Over the course of radio waves in the plane and in space"), *Sitzungsbr. Akad. Wiss. Wien*, Vol. 78, pp. 819–838 (1878).

[65] G. Ben-dor, *Shock Wave Reflection Phenomena* (Springer Verlag, New York, 2007), pp. 3–4 and 297–303 (2007).

[66] A. N. Semenov, M. K. Berezkina, and I. V. Krassovskaya, "Classification of pseudo-steady shock wave reflection types," *Shock Waves*, Vol. 22, No 4., pp. 307–316 (2012). https://doi.org/10.1007/s00193-012-0373-z

[67] G. Birkhoff, "Hydrodynamics: A study in logic, fact, and similitude," (Princeton University pp. 129–130) (1950).

[68] P. Colella and L. F. Henderson, "The von Neumann paradox for the diffraction of weak shock waves" *Journal of Fluid Mechanics*, Vol. 213, pp. 71–94 (1990). https://doi.org/10.1017/S0022112090002221

[69] B. W. Skews and J. T. Ashworth, "The physical nature of weak shock wave reflection," *Journal of Fluid Mechanics*, Vol. 542, pp. 105–114 (2005). https://doi.org/10.1017/S0022112005006543

[70] J. von Neumann, "Oblique reflection of shocks," in *John von Neumann Collected Works*, edited by A. H. Taub (MacMillan, New York, 1963), Vol. 6, pp. 238–299 (1963).

[71] M. M. Karzova, V. A. Khokhlova, E. Salze, S. Ollivier, and P. Blanc-Benon, "Mach stem formation in reflection and focusing of weak shock acoustic pulses," *Journal of the Acoustical Society of America*, Vol. 137, No. 6, EL436–EL442 (2015). https://doi.org/10.1121/1.4921681

[72] M. M. Karzova, T. Lechat, S. Ollivier, D. Dragna, P. V. Yuldashev, V. A. Khokhlova, and P. Blanc-Benon, "Irregular reflection of spark-generated shock pulses from a rigid surface: Mach-Zehnder interferometry measurements in air," *Journal of the Acoustical Society of America*, Vol. 145, No. 1, pp. 26–35 (2019). https://doi.org/10.1121/1.5084266

[73] C. Desjouy, S. Ollivier, O. Marsden, M. M. Karzova, and P. Blanc-Benon, "Irregular reflection of weak acoustic shock pulses on rigid boundaries: Schlieren experiments and direct numerical simulation on a Navier-Stokes solver," *Physics of Fluids*, Vol. 28, No. 2, p. 027102 (2016). https://doi.org/10.1063/1.4940987

[74] M. Geva, O. Ram, and O. Sadot, "The non-stationary hysteresis phenomenon in shock wave reflections," *Journal of Fluid Mechanics*, Vol. 732, R1 (2013). https://doi.org/10.17/jfm.2013.423

[75] T. Suzuki, T. Adachi, and S. Kobayashi, "Experimental analysis of reflected shock behavior over a wedge with surface roughness," *JSME International Journal Series B Fluids and Thermal Engineering*, Vol. 36, No. 1, pp. 130–134 (1993). https://doi.org/10.1299/jsmeb.36.130

[76] S. Baskar, F. Coulouvrat, and R. Marchiano, "Nonlinear reflection of grazing acoustic shock waves: Unsteady transition from von Neumann to Mach to Snell-Descartes reflectoins," *Journal of Fluid Mechanics*, Vol. 575, pp. 27–55 (2007). https://doi.org/10.1017/S0022112006003752

[77] E. A. Zabolotskaya and V. R. Khokhlov, "Quasi-plane waves in the nonlinear acoustics of confined beams," *Soviet Physics Acoustics*, Vol. 15, pp. 35–40 (1969).

[78] K. M. Leete, K. L. Gee, T. B. Neilsen, and T. T. Truscott, "Mach stem formation in outdoor measurements of shocks," *Journal of the Acoustical Society of America*, Vol. 138, No. 6, EL522–EL 527 (2015). https://doi/org/10.1121/1.4937745

[79] B. O. Reichman, K. L. Gee, T. B. Neilsen, J. M. Downing, M. M. James, A. T. Wall, S. A. McInerny, "Characterizing acoustic shocks in high-performance jet aircraft flyover noise," *Journal of the Acoustical Society of America*, Vol. 143, No. 3, pp. 1355–1365 (2018). https://doi.org/10.1121/1.5026026

[80] K. L. Gee, T. B. Neilsen, J. M. Downing, M. M. James, R. L. McKinley, R. C. McKinley, and A. T. Wall, "Near-field shock formation in noise propagation from a high-power jet aircraft," *Journal of the Acoustical Society of America*, Vol. 133, No. 2, EL88–EL93 (2013). https://doi.org/10.1121/1.4773225

[81] C. L. Morfey and G. P Howell, "Nonlinear propagation of aircraft noise in the atmosphere," *AIAA Journal*, Vol 19, No. 8, pp. 986–992 (1981). https://doi.org/10.2514/3.51026

[82] B. O. Reichman, M. B. Muhlestein, K. L. Gee, T. B. Neilsen, and D. C. Thomas, "Evolution of the derivative skewness for nonlinearly propagating waves," *Journal of the Acoustical Society of America*, Vol. 139, No. 3, pp. 1390–1403 (2016). https://doi.org/10.1121/1.4944036

[83] M. B. Muhlestein, K. L. Gee, T. B. Neilsen, and D. C. Thomas, "Prediction of nonlinear propagation of noise from a solid rocket motor," *Proceedings of Meetings on Acoustics*, Vol. 18, No. 1 040006 (2013). https://doi.org/10.1121/1.4828827

[84] B. M. Harker, T. B. Neilsen, K. L. Gee, A. T. Wall, and M. M. James, "Spatiotemporal-correlation analysis of jet noise from a high-performance military aircraft," *AIAA Journal*, Vol. 54, No. 5, pp. 1554–1566 (2016). https://doi.org/10.2514/1.J054442

[85] K. Viswanathan, J. R. Underbrink, and L. Brusniak, "Space-time correlation measurements in near fields of jets," *AIAA Journal*, Vol. 49, No. 8, 1577–1599 (2011). https://doi.org/10.2514/1.J050750

[86] C. K. W. Tam, N. N. Pastouchenko, K. Viswanathan, "Continuation of the near acoustic field of a jet to the far field part I: theory," AIAA Paper 2010-3728, June 2010. https://doi.org/10.2514/6.2010-3728

[87] C. K. W. Tam, K. Viswanathan, N. N. Pastouchenko, and B. Tam, "Continuation of near-acoustic fields of jets to the far field part II: experimental validation and noise source characteristics," AIAA Paper 2010-3729, June 2010. https://doi.org/10.2514/6.2010-3729

[88] F. M. Pestorius and D. T. Blacksotck, "Propagation of finite-amplitude noise," in *Finite-Amplitude Wave Effects in Fluids*, edited by L. Bjorno (IPC Science and Technology, Guildford, 1973), pp. 24–29 (1973).

[89] M. O. Anderson, "The propagation of a spherical N wave in an absorbing medium and its diffraction by a circular aperture," Technical Report No. ARL-TR-74-25, Applied Research Laboratories, The University of Texas at Austin, Austin, TX (1974).

[90] K. L. Gee, "Prediction of nonlinear jet noise propagation," Ph.D. thesis, The Pennsylvania State University, University Park, PA (2005).